

BALLISTOCARDIOGRAPHY:
PHYSICALLY-BASED MODELING TO BRIDGE PHYSIOLOGY AND
TECHNOLOGY

A thesis
presented to
the Faculty of the Graduate School
at the University of Missouri-Columbia

In Partial Fulfillment
of the Requirements for the Degree
Master of Science

by
NICHOLAS MATTIA MARAZZI
Dr. Giovanna Guidoboni, Thesis Supervisor
DECEMBER 2020

The undersigned, appointed by the dean of the Graduate School, have examined the thesis entitled

Ballistocardiography: physically-based modeling to bridge physiology and technology

presented by Nicholas Mattia Marazzi, a candidate for the degree of master of Electrical Engineering, and hereby certify that, in their opinion, it is worthy of acceptance

Dr. Giovanna Guidoboni

Dr. Marjorie Skubic

Dr. James M. Keller

Dr. Virginia H. Huxley

*To my sister and my parents,
my grandparents
and my friends.*

You have always been there when the rain starts to pour.

Acknowledgements

First, I want to thank my advisor, Dr. Guidoboni. Without your scientific guidance, your support and constant encouragements none of the present work would have been possible. Thank you for always remembering me that there are not problems, but opportunities, and to show me how to keep smiling to life in every moments.

I would like to thank Dr. Skubic for her valuable suggestions and for the opportunity to actively participate in her Lab.

I would like to thank Dr. Keller, your suggestions, insight and lectures helped me developing a strong curiosity towards the world of the artificial intelligence and the machine learning. Thank you also for letting me be part of the football tradition at Mizzou.

I would like to thank Dr. Huxley. I became passionate about physiology with our discussion about the lymphatic system and I will keep memories of the meetings in your lab, fighting against the entropy and discussing about the fascinating world of physiology.

I would like to thank Dr. Sacco. Your passion during the lesson in the N11 classroom at the Politecnico of Milano were the reason why I started this journey four years ago.

I would like to thank Dr. Popescu, Dr. Heise and Dr. Despins for the discussions in the weekly BCG meeting that helped improve this work.

Finally, thanks to all the friends who made this experience at Mizzou unique. A special thanks to Moein, Ahmad and Ruhan for helping me in the Lab session and in my research work.

Contents

1	Introduction	1
1.1	Ballistocardiography and Ballistocardiogram: a physically-based viewpoint to bridge physics and technology	2
1.2	Organization of the thesis	3
2	Ballistocardiography: physiological foundations, physics, technology and modeling	5
2.1	BCG Physiology	5
2.1.1	Physiological BCG signal (pBCG)	6
2.1.2	Physiological contributions to the pBCG	7
2.2	BCG modeling	9
2.2.1	Body as a heterogeneous mixture of blood and everything else	9
2.2.2	Model reduction: lumped volumes	10
2.2.3	Closed-loop Model of the cardiovascular circulation	11
2.2.4	Using the closed-loop model to simulate displacement, velocity and acceleration BCG signals	14
2.3	BCG Tecnology	16
2.3.1	Suspended bed	16
2.3.2	Stationary Bed	17
2.4	BCG Physics	17
2.4.1	Measured BCG signal (mBCG)	17
2.4.2	Physics of the accelerometer on the suspended bed ($j = sb$)	18
2.4.3	Physics of the load cells system ($j = lc$)	19
2.4.4	Load cells under the bed posts ($j = lc$), numerical solution	20
3	CoM motion reconstruction for the suspended bed and load cell system	24

3.1	Introduction	24
3.2	Methods	25
3.2.1	Data acquisition and signal processing for ECG, SCG and BCG signals on a healthy subject	25
3.2.2	Signal processing and template generation for the suspended bed	26
3.2.3	Signal processing and template generation for the load cell system	28
3.3	Results	30
3.3.1	Reconstructed pBCG signal from the suspended bed	30
3.3.2	Reconstruction of the 3D pBCG signal from the load cell system	31
3.3.3	Towards an individual-specific pBCG	32
3.4	Conclusion	33
4	Non invasive estimate of the pulse pressure with the suspended bed and load cell signals	42
4.1	Background	42
4.2	Methods	44
4.2.1	BCG Sensing Device, Data Acquisition and Signal Processing procedure	44
4.2.2	Non invasive estimate of the absolute pulse pressure	46
4.3	Results	47
4.3.1	Intraclass variability of the relevant BCG features recorded on the suspended bed	49
4.3.2	Absolute Pulse Pressure estimate procedure	50
4.3.3	Absolute Pulse Pressure results for the entire population	51
4.4	Conclusions: advantages and limitation for the proposed method for the Pulse Pressure estimate	52
5	Development of an evolutionary algorithm to individualize the model parameters of the cardiovascular model	55
5.1	Evolutionary algorithms	56
5.2	Problem statement	57
5.2.1	Data Collection	59
5.2.2	Evolutionary algorithm formulation	59
5.3	Results	63
5.3.1	EA algorithm results	63
5.4	Conclusion	68

List of Figures

2.1	Reference systems to describe the CoM motion: $\mathcal{C} = \{\mathbf{O}, \underline{\mathbf{E}}_X, \underline{\mathbf{E}}_Y, \underline{\mathbf{E}}_Z\}$ is a cartesian reference system that is fixed with the environment, whereas $c = \{\mathbf{o}, \underline{\mathbf{e}}_x, \underline{\mathbf{e}}_y, \underline{\mathbf{e}}_z\}$ is a second reference system that moves with the body and that is centered on the CoM of the subject.	7
2.2	Schematic of the a_y waveform (reproduced from [40])	8
2.3	Schematic representation of the closed-loop model proposed in [28] to simulate blood flow through the cardiovascular system.	12
2.4	Basic components of the closed-loop model. <i>Left</i> : ventricles and valves; the subscript i is used to distinguish between left ($i = L$) and right ($i = R$) ventricles; P_i is the ventricular pressure; $R_{1,i}$, $R_{2,i}$ and $R_{3,i}$ are hydraulic resistances assumed to be constant; U_i and E_i characterize ventricular pumping, E_i representing the variable ventricular elastance. <i>Right</i> : large arteries; the subscript k is used to distinguish among different arterial segments, specifically aortic arch ($k = 3$), thoracic aorta ($k = 4$), abdominal aorta ($k = 5$), iliac arteries ($k = 6$) and cerebral arteries ($j = 14$); P_k is the pressure of the specific arterial segment; $R_{a,k}$ and $R_{b,k}$ are the hydraulic resistances representing viscous effects; L_k is the inductance representing inertial effects; C_k and γ_k represent elastic and viscoelastic properties of the arterial wall, respectively.	15
2.5	Replica of the suspended ballistocardiography bed originally designed by Burger, et al. [8], utilized in the present work.	17
2.6	Reference systems to describe the CoM motion ON the suspended bed: $\mathcal{C} = \{\mathbf{O}, \underline{\mathbf{E}}_X, \underline{\mathbf{E}}_Y, \underline{\mathbf{E}}_Z\}$ is a cartesian reference system that is fixed with the environment, whereas $c = \{\mathbf{o}, \underline{\mathbf{e}}_x, \underline{\mathbf{e}}_y, \underline{\mathbf{e}}_z\}$ is a second reference system that moves with the body and that is centered on the CoM of the subject. $\underline{\mathbf{r}}(t)$ $\underline{\mathbf{r}}(t)$ denote the position of the origin of the frame of reference c that is centered on the individual center of mass.	18
2.7	Reference systems to describe the CoM motion for the load cell: $\underline{\mathbf{X}} = \{X, Y, Z\}$ is a cartesian reference system that is fixed with the environment, whereas R_i with $i = 1, \dots, 4$ are the signal recorded via the load cell signal.	19

3.1	Reference system for the recordings on the suspended bed. Red: reference system utilized in the present work, in agreement with the conventions for presentation or reproduction of vector ballistocardiographic records (red arrows) [40]. Green: Accelerometer reference system.	26
3.2	Reference system for the recordings on the load cell system. Red: reference system utilized in the present work, in agreement with the conventions for presentation or reproduction of vector ballistocardiographic records (red arrows) [40]. Green: Reference system adopted to recover the pBCG signal from the signal recorded on the load cell system.	29
3.3	Average value of the recorded R_j^V plotted against the known masses.	29
3.4	Recording on one subject of the y component of the pBCG tensor (Left) and the x component of the pBCG tensor (Right): (a): experimentally recorded a_y (grey curve) and computed template a_y^T (red curve),(c)- (e) numerically computed v_y and d_y (grey curve) via an integration process and computed template v_y^T and d_y^T . (b), experimentally recorded a_x (grey curve) and computed template a_x^T (blue curve), (d)-(f): numerically computed v_x and d_x (grey curve) via an integration process and computed template v_x^T and d_x^T (blue curve) .	34
3.5	(a): d_y in one heart beat (black curve) and template curve d_y^T (blue curve). The colored circles indicates some reference points for d_y , whereas the colored squares indicates some reference points for d_y^T . (b): d_x in one heart beat (black curve) and template curve d_x^T (blue curve). (c) CoM motion in the lateral-longitudinal plane.	35
3.6	Vector valued function $\mathcal{T}_{R,j}$ with $j = 1, \dots, 4$	35
3.7	Recording on one subject of the y component of the pBCG tensor (Left) and the x component of the pBCG tensor (Right): (a): experimentally recorded a_y (grey curve) and computed template a_y^T (red curve),(c)- (e) numerically computed v_y and d_y (grey curve) via an integration process and computed template v_y^T and d_y^T . (b), experimentally recorded a_x (grey curve) and computed template a_x^T (blue curve), (d)-(f): numerically computed v_x and d_x (grey curve) via an integration process and computed template v_x^T and d_x^T (blue curve) .	36
3.8	(a): d_y in one heart beat (black curve) and template curve d_y^T (blue curve). The colored circles indicates some reference points for d_y , whereas the colored squares indicates some reference points for d_y^T . (b): d_x in one heart beat (black curve) and template curve d_x^T (blue curve). (c) CoM motion in the lateral-longitudinal plane.	37
3.9	3D motion as reconstructed from the signal recorded on the load cell system.	37

4.1	Simulated f_d , f_v and f_a via the closed-loop model: (a) black curve: f_d curves resulting considering all cardiovascular compartment, f_d curves resulting considering only the thoracic and abdominal compartment. (b) f_v curves resulting considering all cardiovascular compartment, f_v curves resulting considering only the thoracic and abdominal compartment. (c) f_a curves resulting considering all cardiovascular compartment, f_a curves resulting considering only the thoracic and abdominal compartment. representation.	45
4.2	Comparison of the pressure waveform in the thoracic (top) and abdominal artery (bottom). Blue curve: $P_i = \frac{V_i}{C_i} + \gamma \frac{dV_i}{dt}$. Orange curve: $\tilde{P}_i = \frac{V_i}{C_i}$	45
4.3	Bar chart summarizing the mean value and standard deviation of the recorded BCG features for the male subjects (blue bars) and the female subjects (red bars). (a) T_1^g , (b) T_K^g , (c) T_1^v , (d) T_1^d	50
4.4	(a): recorded d_y (grey curves) and template curve (red curve) for subject 4.(b) d_y waveforms with a correlation below 0.4 and lag-time above 0.4 (blue shaded curve).(c): comparison between the predicted brachial pulse pressure amplitude via the proposed methodology (blue shaded curve) and the measured GT pressure (red line) for subject 4.	51
4.5	(a): recorded d_y (grey curves) and template curve (red curve) for subject 7.(b) d_y waveforms with a correlation below 0.4 and lag-time above 0.4 (blue shaded curve).(c): comparison between the predicted brachial pulse pressure amplitude via the proposed methodology (blue shaded curve) and the measured GT pressure (red line) for subject 7.	51
4.6	(a) blue bar: mean value and standard deviation of predicted brachial pulse pressure for the male subject involved in the study, black bar: mean value and standard deviation of GT pressure measured via the cuff device in the lab. (b) red bar: mean value and standard deviation of predicted brachial pulse pressure for the female subject involved in the study, black bar: mean value and standard deviation of GT pressure measured via the cuff device in the lab.	53
5.1	$\mathcal{T}_{f_a}^M$: collection of the individually segmented $f_{a,j}^M(t)$ curves for subject 4 (black curves). $f_{a,j}^M$: selected objective curves for subject 4.	66
5.2	Resulting value of the parameter \mathcal{P}^r predicted by the EA.	66
5.3	Comparison among the experimentally measured a_y curve and the three best-ranked a_y curve computed by the EA (colored-curve).	67
5.4	Left: Predicted central aortic pressure via the personalized input parameter obtained after the first run of the EA. Right: Comparison between the experimentally measured brachial pulse pressure (blue lines) and the the pressure predicted by the EA.	67

List of Tables

2.1	Anatomical meaning of the circuit nodes	12
2.2	Geometrical parameters for the main arterial segments	14
2.3	Anatomical meaning of the circuit nodes	15
3.1	Details of subjects involved in the CoM reconstruction project.	25
3.2	Comparison between the reconstructed longitudinal acceleration a_Y , velocity v_Y and displacement d_Y for three subjects.	38
3.3	Comparison between the reconstructed lateral acceleration a_X , velocity v_X and displacement d_X for three subjects.	39
4.1	Details of subjects involved in the blood pressure study.	43
4.2	Parameter of the proposed physiological-based formula.	46
4.3	Summary of the analyzed BCG features for the subject involved in the study. The table distinguishes among features pertaining to the acceleration, velocity and displacement BCG.	48
4.4	mBCG relevant features among the subjects involved in the study	48
4.5	mBCG relevant features among the subjects involved in the study	49
4.6	Comparison between the brachial pressure computed via the proposed cuff-less methodology and the GT brachial pressure measured in the lab.	52
5.1	Cardiovascular Physiology: Condition establishing if a combination $\mathcal{P}_{r,i}$ is physiological.	64
5.2	Summary of the baseline and the standard deviation values utilized in the EA simulation for each of the bio-mechanical parameter for the left and right ventricle and the arterial segments.	64
5.3	Summary of the reported range of the length and radii of the arterial compartment.	65

5.4 Quantitative comparison between the mean J-K feature predicted by the EA and the J-K features measured experimentally. $\bar{A}_J^{\mathcal{P}}$ and $\bar{A}_K^{\mathcal{P}}$ represent the mean amplitude of the J-peak and K-valley of the three best ranked curve predicted for each run by the EA, whereas $\bar{T}_J^{\mathcal{P}}$ and $\bar{T}_K^{\mathcal{P}}$ are the mean timing of the J-peak and K-valley of the three best ranked curve, respectively, predicted for each run by the EA. Conversely, $\bar{A}_J^{\mathcal{M}}$ and $\bar{A}_K^{\mathcal{M}}$ represent the amplitude of the J-peak and K-valley, whereas $\bar{T}_J^{\mathcal{M}}$ and $\bar{T}_K^{\mathcal{M}}$ 68

List of Algorithms

1	Evolutionary Algorithm	57
2	Initialize Population	60
3	Evaluate Fitness	60
4	Mutation	62
5	Check for Convergence	62
6	Mutation	65

Ballistocardiography: physically based modeling to bridge physiology and technology

Nicholas Mattia Marazzi

Abstract

The ballistocardiogram (BCG) captures the motion of the center of mass (CoM) of the human body resulting from the blood motion within the circulatory system. The BCG signal reflects the status of the cardiovascular system as a whole and, for this reason, it offers a more holistic evaluation of cardiovascular performance than traditional markers, such as electrocardiography or echocardiography. In addition, the acquisition of BCG signals is not invasive, can be performed with several devices -such as accelerometers, chairs, hydraulic system- and does not require body contact. However, the utilization of the BCG as a clinical diagnosis tool and monitoring method is currently hindered by the absence of standardized methods to link the motion of the CoM of the human body, which constitutes the physiological BCG (pBCG), with the BCG signal acquired with sensing devices, which constitute the measured BCG (mBCG). To address this issue, in the first part of the present work we provide a formal definition of pBCG and mBCG, which will be then utilized to (i) define the physical connection between the mBCG obtained with two sensing devices, i.e. the suspended bed and the load cell system, and the pBCG signal and (ii) reconstruct the individual CoM motion.

In the second part of the thesis, we focus on the synergistic combination between the physiology behind the BCG signal and the physics of the sensing devices, which may lead to novel clinical applications. In particular, we propose a cuff-less method for absolute pulse pressure assessment via the synergistic integration of two components, namely (i) theoretical simulations of cardiovascular physiology by means of a mathematical closed-loop model of the cardiovascular system, and (ii) synchronous ECG, SCG and BCG data acquired in our laboratory. Then, we present an evolutionary algorithm aimed at individualizing the closed-loop model of the cardiovascular system, with which we will also provide an estimate of the arterial pressure. Finally, in the last part of the thesis, we draw the conclusion of this study, showing how the integration of the mathematical modeling alongside with clinical studies can improve the understanding of the BCG signal and actively contributing to the development of new clinical monitoring solution.

Chapter 1

Introduction

Ballistocardiography is a method for sensing the repetitive motions of the human body arising from the sudden ejection of blood into the great vessels with each heart beat. In particular, ballistocardiography captures a 3D motion, called ballistocardiogram (BCG), which is originated by the motion of the center of mass (CoM) of the human body. Compared to traditional monitoring techniques, such as electrocardiography, echocardiography and intravascular catheterization, the BCG signal offers a promising venue for monitoring cardiovascular function as a whole. Indeed, both the ECG, which is generated by electrical changes due to the periodic depolarization/repolarization of the cardiac muscle at each heartbeat, and the echocardiography, which utilizes a Doppler ultrasound instrument to create two and three dimensional images of the heart, are mainly focused on the heart, providing limited information on the vasculature. Conversely, the BCG signal reflects the status of the cardiovascular system as a whole, thereby making it an ideal solution to monitor cardiovascular function. In addition, the acquisition of BCG signals is not invasive and does not require body contact, thereby eliminating the risk of infections and making it a viable option for both hospital and in-home monitoring.

Although the BCG signal offers a potentially valuable monitoring tool for the early diagnosis of cardiovascular disease (CVDs), the BCG utilization in the clinical settings has been limited by the absence of a standardized measurement technique, which could make BCG measurements and interpretation device-independent. Consequently, the lack of knowledge of what a healthy BCG waveform should look like, makes it extremely challenging to identify instances when changes in the BCG waveform are truly indicative of pathological conditions rather than changes in the device setting. With the aim of fully exploiting the potential of the BCG signal as a comprehensive cardiovascular tool, in the present thesis we utilize a physically-based modeling approach to *(i)* increase the mechanistic understanding of the BCG signal which is acquired via different sensing devices, *(ii)* propose novel non-invasive solutions, driven by the physiology and physics of the signal, for the cardiovascular moni-

toring and *(iii)* lay the foundations towards a standardization of the BCG waveform, which ultimately may lead to a BCG-based cardiovascular monitoring.

The remaining of this chapter is organized as follow. In Sec 1.1 we briefly recall the BCG history and further explain the rationale behind the modeling approach to the BCG signal utilized in this thesis. Then, in Sec. 1.2 we outline the organization of the thesis, with a summary of the content of each chapter.

1.1 Ballistocardiography and Ballistocardiogram: a physically-based viewpoint to bridge physics and technology

Ballistocardiography was originally discovered in the late 19th century. One of the first observation of the BCG phenomenon is traced back to the work of Gordon in 1877, with the finding that as a subject would stand on a weighing scale, the needle would vibrate synchronously to the subject's heartbeat [14]. Nearly 60 years later, Starr and colleagues created an instrument in the form of a table with a mobile top surface to measure the BCG in a repeatable scientific manner and laid the foundations for the ballistocardiogram field study. After this pioneering work, the BCG has been the focus of intense research in 1940's through the early 80's, with a main emphasis on the modeling/mechanism behind the BCG waveform [44] [16]. Then, the method slowly faded away due to a combination of factors, such as the absence of a standardized measurement technique and the lack of understanding of the physiology behind the BCG signal, as well as the development of new technological solution such as ultrasound and echocardiography [12]. .

The 20th century witnessed a resurgence in the field of the BCG, with a variety of novel sensors to measure the BCG signal noninvasively, for example in the form of bed sensors, chair sensors and weighing scales [38, 17, 19]. Alongside with the technological development, several algorithm for interpreting the BCG signal have been developed, which may be mainly grouped into time-domain algorithms, frequency-domain algorithms, and wavelet-domain algorithms. Time domain algorithms aim at automatically detecting the local maxima or local minima of the recorded signal. The main limitation of these method is the reduction of prominent peaks with elderly adults, as well as the influence of motion artifacts. Time-frequency algorithm project the signal into the frequency domain to then analyze its spectral content. Lastly, wavelet-domain algorithms aim to decompose the signal into different components and to then select the part which shows an agreement with the vital signs. Although these algorithms have the huge advantage of being utilized with automated pipeline capable of handling a large amount of patients, they share a common limitation: they are primarily data-driven approaches that do not investigate the physics behind the sensor and the physiological meaning of the signal that is recorded. Indeed, although the BCG signal originates from the CoM motion, different sensing devices can capture complementary,

yet very different, kinematic aspects of the CoM motion. This concept will be further discussed in Chapter 2.

To overcome this limitation, in this thesis we adopted a complementary view, by investigating the physics of the instruments utilized to detect BCG signal and provide a mechanistic interpretation of the recorded signal via mathematical modeling. Indeed, a mathematical model can serve as a *virtual laboratory*, where multiple simulation scenarios are explored and all variables are kept under control and tested. As a result, this mathematical modeling framework can provide quantitative tools to bridge the developed non-invasive technology with the physiology of the BCG signal. Finally, it is worth noting that our long-term goal is to fuse together the advantage of deterministic modeling with the automated data-driven approaches to fully exploit the potential of BCG as a clinical tool.

1.2 Organization of the thesis

The present thesis is structured as follows:

- Chapter 2: the theoretical foundations of the BCG are outlined, with a particular emphasis on the concepts of pBCG and mBCG. Then, we provide an overview of the technological solution that are utilized to record the BCG signal in this work and we present the closed-loop mathematical model of the cardiovascular system that will be utilized in this thesis;
- Chapter 3: Reconstruction of the CoM motion for the suspended bed and the load cell system;
- Chapter 4 Development of a methodology that leverages physiology via a closed-loop model of the cardiovascular system to non-invasively estimate the absolute pulse wave pressure;
- Chapter 5: Development of an evolutionary algorithm to individualize the closed-loop model of the cardiovascular system;
- Chapter 6: Conclusion and future works.

Chapter 2

Ballistocardiography: physiological foundations, physics, technology and modeling

In this chapter we provide a rigorous definition of the physiological BCG (**pBCG**) as a function of the **CoM** motion of the human body (Section 2.1). Then, in Sec.2.2 we describe how the **CoM** motion can be modeled mathematically utilizing the mixture theory and we outline the physically-based model of the cardiovascular system which will be utilized in the present thesis to interpret the **pBCG**. In Sec. 2.3 we provide an overview of the sensing devices that are utilized in this thesis to record the BCG signal, i.e. the suspended bed and the load cell system, and we introduce the concept of the measured BCG (**mBCG**). Finally, in Sec. 2.4 we explore the physics of each instruments to derive the mathematical relationship between the **pBCG** and **mBCG** with both the suspended bed and load cell system.

2.1 BCG Physiology

The aim of this section is to provide a rigorous definition to the concept of the physiological BCG signal (**pBCG**). For this purpose, we firstly define mathematically the kinematics of the **CoM** motion via displacement, velocity and acceleration. By so doing, we naturally lay the foundations for the formal definition of the **pBCG** in Sec. 2.1.1. Then, in Sec. 2.1.2, we review the physiological events occurring in the human body giving rise to the **CoM** motion, i.e. the **pBCG**.

2.1.1 Physiological BCG signal (pBCG)

Following the convention by Starr and Noordegraaf, we introduce two reference system to describe the CoM motion. Referring to Fig. 2.1, we denote as $\underline{\mathbf{X}} = \{X, Y, Z\}$ the coordinate in a cartesian reference system $\mathcal{C} = \{\underline{\mathbf{O}}, \underline{\mathbf{E}}_X, \underline{\mathbf{E}}_Y, \underline{\mathbf{E}}_Z\}$ that is fixed with the environment, and we denote with $\underline{\mathbf{x}} = (x, y, z)$ the coordinate in a second reference system $c = \{\underline{\mathbf{o}}, \underline{\mathbf{e}}_x, \underline{\mathbf{e}}_y, \underline{\mathbf{e}}_z\}$ that moves with the body and that is centered on the CoM of the subject. Importantly, we note that the two reference systems have opposite direction of the axes, namely

$$\underline{\alpha} = \alpha_x \underline{\mathbf{E}}_X + \alpha_y \underline{\mathbf{E}}_Y + \alpha_z \underline{\mathbf{E}}_Z = -\alpha_x \underline{\mathbf{e}}_x - \alpha_y \underline{\mathbf{e}}_y - \alpha_z \underline{\mathbf{e}}_z \quad (2.1)$$

Let us denote by Ω the volume occupied by the human body. In c , the mass distribution within Ω is described by the mass density $\rho = \rho(\underline{\mathbf{x}}, t)$, with $\underline{\mathbf{x}} = (x, y, z) \in \Omega$ and $t \geq 0$. Since blood moves throughout the body, the mass density is not a constant but it varies both in space and time. The position $\underline{\mathbf{u}} = \underline{\mathbf{u}}(t)$ of the center of mass (CoM) of the human body at any time t in the reference system is given by

$$\underline{\mathbf{u}}(t) = \frac{\int_{\Omega} \rho(\underline{\mathbf{x}}, t) \underline{\mathbf{x}} d\underline{\mathbf{x}}}{\int_{\Omega} \rho(\underline{\mathbf{x}}, t) d\underline{\mathbf{x}}} = \frac{1}{M} \int_{\Omega} \rho(\underline{\mathbf{x}}, t) \underline{\mathbf{x}} d\underline{\mathbf{x}} \quad (2.2)$$

where M is the total body mass. The CoM displacement $\underline{\mathbf{d}}(t)$ can be computed as the difference between the position vector $\underline{\mathbf{u}}(t)$ in the reference system c and a fixed vector $\underline{\bar{\mathbf{u}}}$ in the reference system \mathcal{C} , so that we have

$$\underline{\mathbf{d}}(t) = \underline{\mathbf{u}}(t) - \underline{\bar{\mathbf{u}}}. \quad (2.3)$$

The velocity $\underline{\mathbf{v}}(t)$ and acceleration $\underline{\mathbf{a}}(t)$ in the reference system c of the CoM can be obtained via time differentiation as

$$\underline{\mathbf{v}}(t) = \frac{d}{dt} \underline{\mathbf{u}}(t) = \frac{d}{dt} \underline{\mathbf{d}}(t) = \frac{1}{M} \int_{\Omega} \frac{\partial \rho}{\partial t}(\underline{\mathbf{x}}, t) \underline{\mathbf{x}} d\underline{\mathbf{x}} \quad (2.4)$$

$$\underline{\mathbf{a}}(t) = \frac{d}{dt} \underline{\mathbf{v}}(t) = \frac{1}{M} \int_{\Omega} \frac{\partial^2 \rho}{\partial t^2}(\underline{\mathbf{x}}, t) \underline{\mathbf{x}} d\underline{\mathbf{x}}. \quad (2.5)$$

Eqs. 2.3-2.5 represent the kinematic description of the CoM motion of the human body, which constitutes the physiological BCG (pBCG). Thus, pBCG is not a simple waveform; rather, it comprises 9 different waveforms corresponding to the CoM displacement, velocity and acceleration in the three directions of the physical space. This concept can be formalized mathematically as follows:

Definition 1 (Physiological BCG) The physiological BCG (pBCG) is represented by the 3×3 tensor $\underline{\underline{\varphi}} = \underline{\underline{\varphi}}(t)$ whose columns are displacement, velocity and acceleration of the

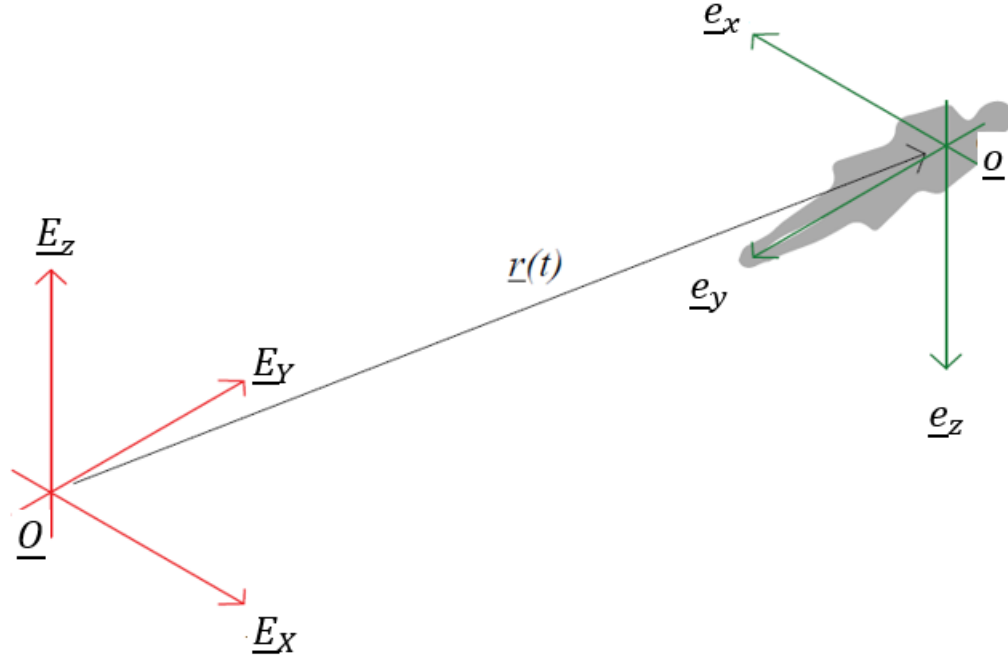


Figure 2.1: Reference systems to describe the CoM motion: $\mathcal{C} = \{\underline{\mathbf{O}}, \underline{\mathbf{E}}_X, \underline{\mathbf{E}}_Y, \underline{\mathbf{E}}_Z\}$ is a cartesian reference system that is fixed with the environment, whereas $\mathcal{c} = \{\underline{\mathbf{o}}, \underline{\mathbf{e}}_x, \underline{\mathbf{e}}_y, \underline{\mathbf{e}}_z\}$ is a second reference system that moves with the body and that is centered on the CoM of the subject.

center of mass of the human body, namely

$$\underline{\underline{\varphi}}(t) = [\underline{\mathbf{d}}(t); \underline{\mathbf{v}}(t); \underline{\mathbf{a}}(t)] = \begin{bmatrix} d_x(t) & v_x(t) & a_x(t) \\ d_y(t) & v_y(t) & a_y(t) \\ d_z(t) & v_z(t) & a_z(t) \end{bmatrix} \quad (2.6)$$

where the x direction represents the right to left direction, the y direction represents the head to toe direction, whereas the the z direction represents the back to front direction as shown in Fig. 2.1

2.1.2 Physiological contributions to the pBCG

Having defined the pBCG as the tensor comprising the displacement, velocity and acceleration of the CoM in the three directions of the space, it remains to be established which are the cardiovascular events contributing to the CoM movement. For this purpose, we recall the mechanical analogy reported in the work by Starr and Rawson to describe the ballistic component of the circulation [45]:

...what happens when a long freight train, stopped on the track, is started by the locomotive. The train is not set in motion as a unit, but car by car, the impulse traveling down the train so that the last car moves some time after the first has started. Bend such a train around a curve like the aortic arch, have the locomotive push rather than pull, have it start, move a short distance and stop again, assume a second train for the pulmonary system and one has a reasonably close analogy to what happens in the circulation. The impacts of such a system will be the sum of the impacts of its units (cars) and these will be delivered in various directions due to the curve of the track and at different times as each starts and stops a little later in time than the one before it.

Thus, the periodic motion of the CoM of an individual is originated by the interplay among (i) the heart, which is the physiological unit that accelerates the mass of blood, and (ii) the systemic circulation, which provides the route where the blood moves. Specifically, as the blood moves in the circulatory system, the distribution of the mass in the human body changes. Furthermore, during the cardiac and respiratory cycles, the heart, the large vessels and the soft tissue also move, thereby contributing to change the mass distribution inside the body. The total change in mass distribution gives rise to the CoM movement described by the 9 kinematic component of the pBCG.

Several works attempted to further disentangle the internal events contributing to the observed pBCG waveform shape. The majority of the literature focuses on the acceleration of the CoM in the longitudinal direction, i.e a_y . Indeed, the longitudinal direction is characterized by a larger amplitude compared to the other space directions and the acceleration can be directly obtained utilizing an ultra-low frequency device. Fig. 2.2 reports an example of an a_y waveform, with the nomenclature recommended by the committee on ballistocardiography terminology in 1956 [40]. The longitudinal acceleration consists of the systolic waves, comprising the H, I, J, and K peaks and valleys (highlighted with a green box in Fig. 2.2), which are then followed by the diastolic waves, where the observed morphological peaks and valleys are denoted as L, M, and N (blue box in Fig. 2.2). The presystolic G wave also sometimes appears in the BCG recordings (red box in Fig. 2.2). A brief description of each peak is provided here:

- the H wave is the first headward deflection of the BCG that begins near the ECG R peak.
- the I wave appears early in the systole, whereas the J wave is the largest headward wave of the BCG, which occurs later in the systole.
- the K wave is the next footward ballistic wave to appear near the end of systole and may extend into the early diastole.
- the L and N waves are the smaller headward waves in the diastole with a footward wave in between them named the M wave.

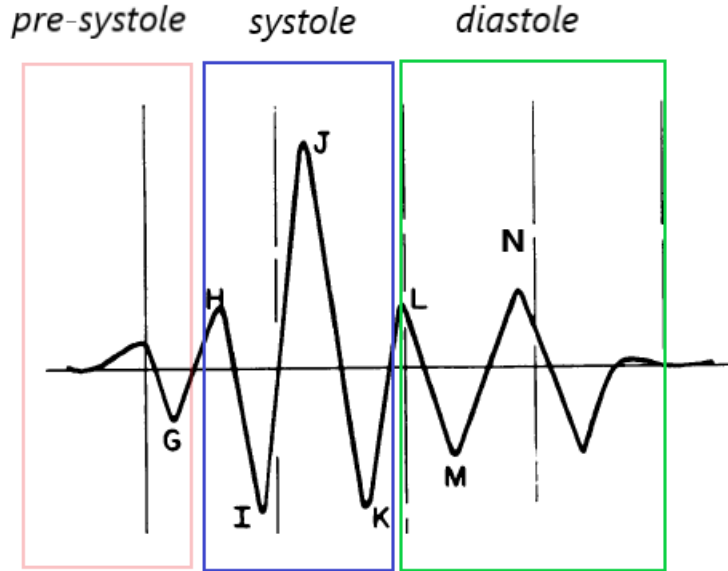


Figure 2.2: Schematic of the a_y waveform (reproduced from [40])

Several studies have been performed to understand the genesis of these peaks and valley. For instance, Starr and Rawson reconstructed the a_y component of the pBCG from the cardiac ejection curves of dogs and then utilized a mathematical model comprising the aorta and the pulmonary artery to relate the reconstructed ballistocardiogram with circulatory events [45]. The authors concluded that the major part of the systolic complex is due to the movements of the blood in the aorta, while the pulmonary contribution was considered to be minor. This finding was confirmed also by Hamilton [16], who studied the forces resulting from the movement of blood through the ascending aorta. In this case, the author reconstructed a_y from an ejection curve computed from pressure measurements made on man and furtherly observed that (i) the J-wave is due to the deceleration of blood into the heart, ascending aorta and pulmonary artery, (ii) the timing of the K wave well correlated with the peak of the femoral pulse pressure curve. The author also hypothesized that the observed peaks in the diastolic wave resulted from the reflection of pressure wave in the arterioles. In 1959, Starr and Noordegraf developed an open-loop model of the cardiovascular system comprising 111 arterial segments and 4 pulmonary segments and they increased the mechanistic understanding of the a_y component by observing that (i) the I-wave is due to the recoil accompanying blood ejection and (ii) the diastolic complex, including the LMN wave complex, seems to be due to changes in blood movements as the wave travels through the peripheral vessels and, to a smaller extent, to the refilling of the heart [44].

Few studies analyzed the lateral direction of the pBCG. Knoop [23] reported the measured acceleration in the frontal plane ($x - y$) and observed how the shape of the frontal BCG

changed significantly in the elderly adults and in other patients involved in the study [44] in the lateral direction. Similarly, March observed a striking increase in the amplitude of the lateral waves in some older normal subjects [31]. In addition, the author concluded that the longitudinal ballistic forces are predominant in the young adults, whereas "... with age, the force vector changes and in middle aged or elderly individuals, it may have an almost purely lateral representation".

After these pioneering studies, which all occurred between the 1940's through the early 80's, a major shift of paradigm occurred. Indeed, the major focus was posed on the development of new non-invasive technological solutions to capture the CoM motion as well as the development of automated pipelines for the processing and analysis of the signal, rather than investigating the relationship between the physiology and the novel sensing device. However, we believe that including the physiology and the physics of the instrument in the analysis of the collected data may help fully exploit the potential associated with the new devices. In the next section, we describe a mathematical modeling approach that can help disentangle the physiological contribution in the pBCG.

2.2 BCG modeling

In this section we describe our modeling approach for the BCG analysis. Firstly, in sec. 2.2.1 we utilize the mixture theory to obtain an explicit relationship between the CoM motion and the blood volume in the cardiovascular system. Then, in Sec. 2.2.2, following the approach described in [44], the human body is subdivided into homogeneous subregions and an explicit relationship between the CoM motion and the volume waveform pertaining to each of this subregions is defined. Finally, in Sec.2.2.3 we present a closed-loop mathematical model of the cardiovascular system that will be utilized to model the pBCG.

2.2.1 Body as a heterogeneous mixture of blood and everything else

Let us consider the body to be a heterogeneous mixture of blood and everything else (including tissue, bones, nerves, ...), which we will refer to as body frame. Let us denote by ρ_b and ρ_f the real densities of blood and body frame, which are assumed to be constant. Let us introduce the volume fractions $\phi_b(\underline{\mathbf{x}}, t)$ and $\phi_f(\underline{\mathbf{x}}, t)$ of blood and body frame as

$$\phi_b(\underline{\mathbf{x}}, t) = \frac{V_b(\underline{\mathbf{x}}, t)}{V} \quad \text{and} \quad \phi_f(\underline{\mathbf{x}}, t) = \frac{V_f(\underline{\mathbf{x}}, t)}{V} \quad (2.7)$$

where $V_b(\underline{\mathbf{x}}, t)$ and $V_f(\underline{\mathbf{x}}, t)$ are the volumes of blood and body frame occupying the reference element volume V . Now, the body mass density ρ can be written as

$$\rho(\underline{\mathbf{x}}, t) = \phi_b(\underline{\mathbf{x}}, t)\rho_b + \phi_f(\underline{\mathbf{x}}, t)\rho_f \quad (2.8)$$

and the CoM position vector can be written as

$$\underline{\mathbf{u}}(t) = \frac{1}{M} \int_{\Omega} \rho(\underline{\mathbf{x}}, t) \underline{\mathbf{x}} d\underline{\mathbf{x}} = \frac{1}{M} \int_{\Omega} \left(\phi_b(\underline{\mathbf{x}}, t) \rho_b + \phi_f(\underline{\mathbf{x}}, t) \rho_f \right) \underline{\mathbf{x}} d\underline{\mathbf{x}} \quad (2.9)$$

In the assumption of full saturation, we can write

$$\phi_b(\underline{\mathbf{x}}, t) + \phi_f(\underline{\mathbf{x}}, t) = 1 \quad \rightarrow \quad \phi_f(\underline{\mathbf{x}}, t) = 1 - \phi_b(\underline{\mathbf{x}}, t). \quad (2.10)$$

Since $\phi_b(\underline{\mathbf{x}}, t) \ll 1$, we can simplify the model by assuming that $\phi_f(\underline{\mathbf{x}}, t) \approx 1$, from which it follows that Eq. (2.9) can be rewritten as

$$\underline{\mathbf{u}}(t) = \frac{1}{M} \int_{\Omega} \phi_b(\underline{\mathbf{x}}, t) \rho_b \underline{\mathbf{x}} d\underline{\mathbf{x}} + \frac{1}{M} \int_{\Omega} \rho_f \underline{\mathbf{x}} d\underline{\mathbf{x}} \quad (2.11)$$

$$= \frac{\rho_b}{M} \int_{\Omega} \phi_b(\underline{\mathbf{x}}, t) \underline{\mathbf{x}} d\underline{\mathbf{x}} + \underline{\mathbf{c}} \quad (2.12)$$

where

$$\underline{\mathbf{c}} := \frac{1}{M} \int_{\Omega} \rho_f \underline{\mathbf{x}} d\underline{\mathbf{x}}. \quad (2.13)$$

Notice that $\underline{\mathbf{c}}$ is a vector that does not depend neither on time nor on space and represents the location of the center of mass of those parts of the body that do not move when a person is laying still. Thus, we can choose $\underline{\mathbf{c}}$ as the fixed vector $\underline{\mathbf{u}}$ in Eq. (2.3). Finally, assuming $\underline{\mathbf{u}} = \underline{\mathbf{c}}$ the displacement $\underline{\mathbf{d}}(t)$ of the body CoM is given by

$$\underline{\mathbf{d}}(t) = \underline{\mathbf{u}}(t) - \underline{\mathbf{u}} = \frac{\rho_b}{M} \int_{\Omega} \phi_b(\underline{\mathbf{x}}, t) \underline{\mathbf{x}} d\underline{\mathbf{x}}. \quad (2.14)$$

2.2.2 Model reduction: lumped volumes

The computation of the integral on the right hand side of Eq. (2.14) requires the knowledge of how the blood volume fraction is distributed throughout the whole body. To simplify the computation of $\underline{\mathbf{d}}(t)$, let us partition the domain Ω occupied by the human body into subregions Ω_k , with $k = 1, \dots, K$, such that

$$\bigcup_{k=1}^K \Omega_k = \Omega \quad \text{and} \quad \overset{\circ}{\Omega}_k \cap \overset{\circ}{\Omega}_l = \emptyset \quad \text{for} \quad k \neq l. \quad (2.15)$$

Thanks to this partition and the additivity of integrals, we can write

$$\underline{\mathbf{d}}(t) = \frac{\rho_b}{M} \int_{\Omega} \phi_b(\underline{\mathbf{x}}, t) \underline{\mathbf{x}} d\underline{\mathbf{x}} = \frac{1}{M} \sum_{k=1}^K \int_{\Omega_k} \rho_b \phi_b(\underline{\mathbf{x}}, t) \underline{\mathbf{x}} d\underline{\mathbf{x}} \quad (2.16)$$

Let us utilize the formula of the midpoint to approximate the integral on the right hand side of Eq. (2.17) so that we can write

$$\underline{\mathbf{d}}(t) = \frac{1}{M} \sum_{k=1}^K \int_{\Omega_k} \rho_b \phi_b(\underline{\mathbf{x}}, t) \underline{\mathbf{x}} d\underline{\mathbf{x}} \approx \frac{1}{M} \sum_{k=1}^K \rho_b \phi_b(\underline{\mathbf{x}}_k, t) \underline{\mathbf{x}}_k |\Omega_k| \quad (2.17)$$

where $\underline{\mathbf{x}}_k$ is the centroid of Ω_k and $|\Omega_k|$ is the measure of the volume Ω_k . Denoting by $V_k(t)$ the volume of blood that occupies the region Ω_k at time t , defined as

$$V_k(t) := \phi_b(\underline{\mathbf{x}}_k, t)|\Omega_k| \quad (2.18)$$

we can approximate the CoM displacement as

$$\underline{\mathbf{d}}(t) \approx \frac{\rho_b}{M} \sum_{k=1}^K V_k(t) \underline{\mathbf{x}}_k. \quad (2.19)$$

We notice that $\underline{\mathbf{d}}(t)$ is a vector, whose components give the displacement in the three spacial directions:

$$d_x(t) = \frac{\rho_b}{M} \sum_{k=1}^K V_k(t) x_k, \quad d_y(t) = \frac{\rho_b}{M} \sum_{k=1}^K V_k(t) y_k, \quad d_z(t) = \frac{\rho_b}{M} \sum_{k=1}^K V_k(t) z_k. \quad (2.20)$$

By differentiation, we can now obtain the expressions for velocity and acceleration

$$\underline{\mathbf{v}}(t) = \frac{\rho_b}{M} \sum_{k=1}^K \frac{d}{dt} V_k(t) \underline{\mathbf{x}}_k, \quad \underline{\mathbf{a}}(t) = \frac{\rho_b}{M} \sum_{k=1}^K \frac{d^2}{dt^2} V_k(t) \underline{\mathbf{x}}_k \quad (2.21)$$

whose componentwise version is

$$v_x(t) = \frac{\rho_b}{M} \sum_{k=1}^K \frac{d}{dt} V_k(t) x_k, \quad v_y(t) = \frac{\rho_b}{M} \sum_{k=1}^K \frac{d}{dt} V_k(t) y_k, \quad v_z(t) = \frac{\rho_b}{M} \sum_{k=1}^K \frac{d}{dt} V_k(t) z_k. \quad (2.22)$$

$$a_x(t) = \frac{\rho_b}{M} \sum_{k=1}^K \frac{d^2}{dt^2} V_k(t) x_k, \quad a_y(t) = \frac{\rho_b}{M} \sum_{k=1}^K \frac{d^2}{dt^2} V_k(t) y_k, \quad a_z(t) = \frac{\rho_b}{M} \sum_{k=1}^K \frac{d^2}{dt^2} V_k(t) z_k. \quad (2.23)$$

2.2.3 Closed-loop Model of the cardiovascular circulation

The closed-loop mathematical model for the cardiovascular system, schematized in Fig. 2.3, leverages the analogy between electric circuits and hydraulic networks, where electric potentials, electric charges, and electric currents correspond to fluid pressures, fluid volumes and volumetric flow rates, respectively [39]. The model comprises a total of 15 subregions, each one representing an anatomical compartment, grouped in 4 main interconnected compartments that are reported in Table. 2.1. We briefly describe each compartment below:

- **the heart:** the heart compartment comprises the left ventricle ($k = 1$) and the right ventricle ($k = 10$). The ventricles are modeled as voltage sources and variable capacitors connected in series, as shown in Fig. 2.4 (Left). The voltage sources describe the electrochemical activation of the ventricles by means of the time-varying input

NODE	COMPARTMENT	SEGMENT
1	Heart	Left Ventricle
2	Systemic	Ascending Aorta
3	Systemic	Aortic Arch
4	Systemic	Thoracic Aorta
5	Systemic	Abdominal Aorta
6	Systemic	Iliac arteries
7	Systemic	Small arteries
8	Systemic	Capillaries
9	Systemic	Veins
10	Heart	Right Ventricle
11	Pulmonary	Pulmonary Arteries
12	Pulmonary	Capillaries
13	Pulmonary	Veins
14	Cerebral	Cerebral Arteries
15	Cerebral	Veins

Table 2.1: Anatomical meaning of the circuit nodes

signals $U_i = U_i(t)$, where the subscript i distinguishes between the left ($i = L$) and right ($i = R$) ventricles. The variable capacitors describe the ventricular biomechanical properties by means of the time-varying elastances $E_i = E_i(t)$, as introduced by Suga et al [29], where the subscript i again distinguishes between the left ($i = L$) and right ($i = R$) ventricles. Denoting by P_i and V_i , with $i = L, R$, pressure and volume of the left and right ventricles, respectively, we have $P_i = E_i V_i$ with

$$E_L(t) = ELD + ELS a_L(t) \quad (2.24)$$

$$E_R(t) = ERD + ERS a_R(t) \quad (2.25)$$

where ELD, ELS, ERD and ERS are given constants characterizing the systolic and diastolic elastances of the left and right ventricles, whereas $a_L(t)$ and $a_R(t)$ are nondimensional activation functions characterizing the timing of the ventricular contractions [15, 4, 33]. In [28], [15], the activation function was described mathematically as

$$a_i(t_m) = \begin{cases} \frac{\tanh(2\pi(t_m - T_a)) - \tanh(2\pi(t_m - T_b))}{2} & t_m < T_s \\ 0 & \text{otherwise} \end{cases} \quad (2.26)$$

for $i = L, R$, where T_a and T_b are given constants, T_s is the length of the systolic part of the cardiac cycle, t_m is defined as $t_m = \text{mod}(t, T_c)$, T_c being the length of the entire cardiac cycle.

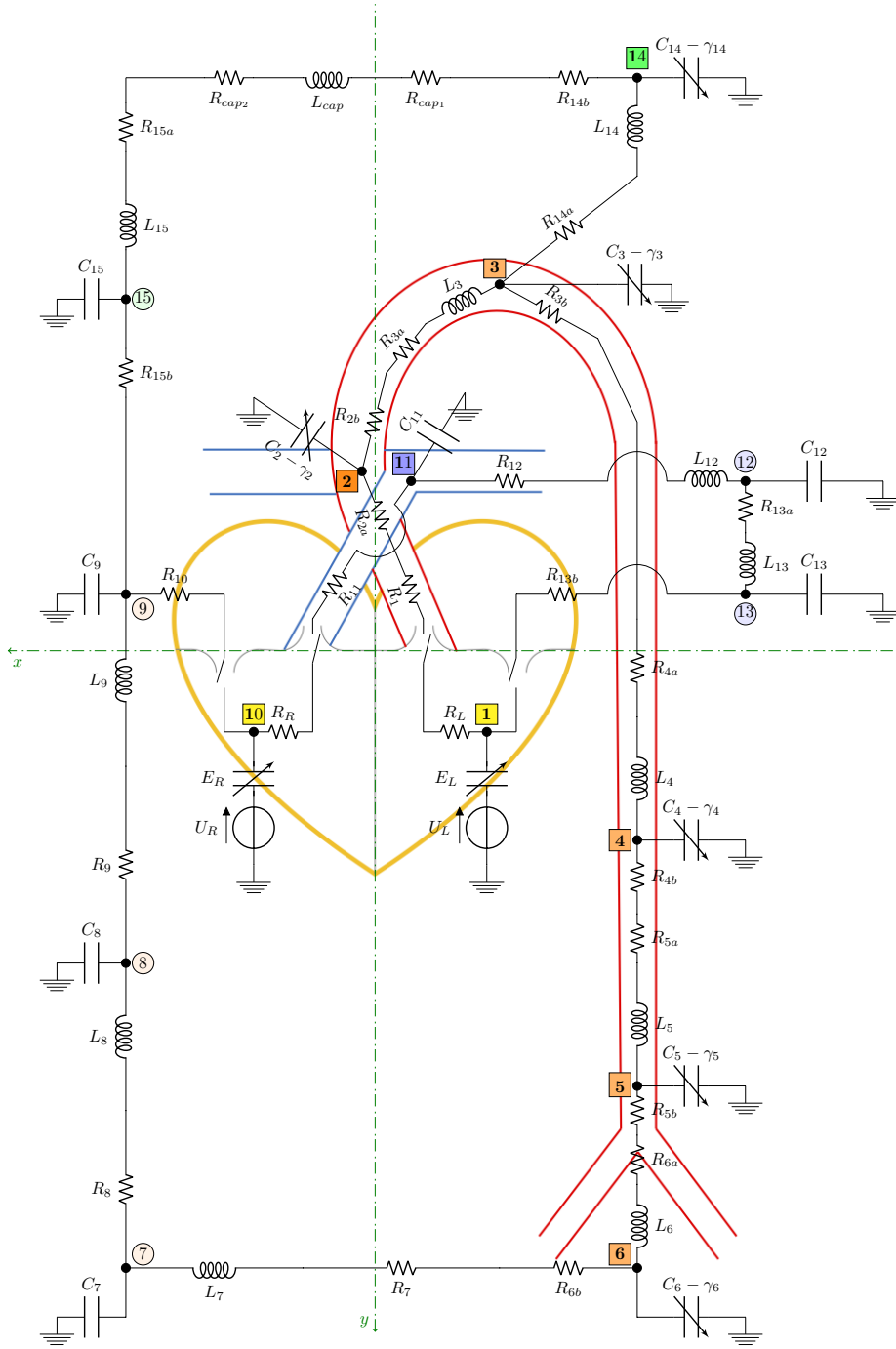


Figure 2.3: Schematic representation of the closed-loop model proposed in [28] to simulate blood flow through the cardiovascular system.

The heart valves are modeled as ideal switches, see Fig. 2.4 (Left), which close as soon as a positive pressure difference between the upstream and downstream nodes of the switch is established.

- **the systemic circulation:** the systemic circulation comprises the arterial segments from the ascending aorta to the iliac arteries ($k = 2, \dots, 6$), the small arteries and capillary segments ($k = 7, 8$) and the central veins ($k = 9$). The large arteries, namely aortic arch, thoracic aorta, abdominal aorta, iliac arteries and cerebral arteries, share the same mathematical description, see Fig. 2.4 (Right), which includes two resistors, one inductor and one variable capacitor representing hydraulic resistance, inertial effects and wall compliance, respectively. The constitutive laws defining these elements are:

$$\begin{aligned}
 (\text{resistor}) \quad & \Delta P = RQ \\
 (\text{inductor}) \quad & \Delta P = L \frac{dQ}{dt} \\
 (\text{variable capacitor}) \quad & \Delta P = \frac{V}{C} + \gamma \frac{dV}{dt}
 \end{aligned}$$

where ΔP is the pressure difference across the element, Q is the volumetric flow rate, V is the fluid volume, R is the hydraulic resistance, L is the inductance, and C and γ are positive constants representing the elastic and viscoelastic properties of the arterial wall, respectively. The parameter values characterizing the main arteries have been computed using the following relationships:

$$R = \frac{8\pi l \eta}{S^2}, \quad L = \frac{\rho_b l}{S}, \quad C = \frac{3lS(a+1)^2}{E(2a+1)}, \quad \gamma = \frac{\delta}{C}, \quad (2.27)$$

where l is the vessel length, $a = r/h$ is the ratio between the vessel radius r and the wall thickness h , η is the blood viscosity, $S = \pi r^2$ is the vessel cross sectional area, ρ_b is the blood density, E is the arterial Young modulus and δ is a viscoelastic parameter. In this work, we have assumed $\rho_b = 1.05 \text{ g cm}^{-3}$, $\eta = 0.035 \text{ g cm}^{-1} \text{ s}^{-1}$, $E = 4 \cdot 10^6 \text{ dyne cm}^{-2}$ and $\delta = 1.56 \cdot 10^{-3} \text{ s}$. The values of the remaining geometrical parameters utilized to determine R , L , C and γ for each of the main arterial segments have been adapted from [44] and [9] and are reported in Table 2.2.

- **the pulmonary circulation:** the pulmonary circulation starts with the pulmonary artery at the right ventricle and converges into the left atrium. It comprises three segments ($k = 11, 12, 13$) sharing the same mathematical description, which includes two resistors, one inductor and one constant capacitor representing hydraulic resistance, inertial effects and wall compliance, respectively. The parameters for these compartments have been obtained from the work of Avanzolini et al [4].
- **the cerebral circulation:** the cerebral circulation branches from the aortic arch and converges into the systemic venous system. It comprises both the cerebral arteries ($k = 14$), which is modeled as the large arteries, i.e. with two resistors, one inductor and one variable capacitor (see Fig. 2.4 (Right)). The cerebral veins ($k = 14$) are also modeled via a RLC combination, even though the capacitor is characterized by

a constant capacitance. The parameters for these compartments have been obtained from the work by Avanzolini et al [4] and [25].

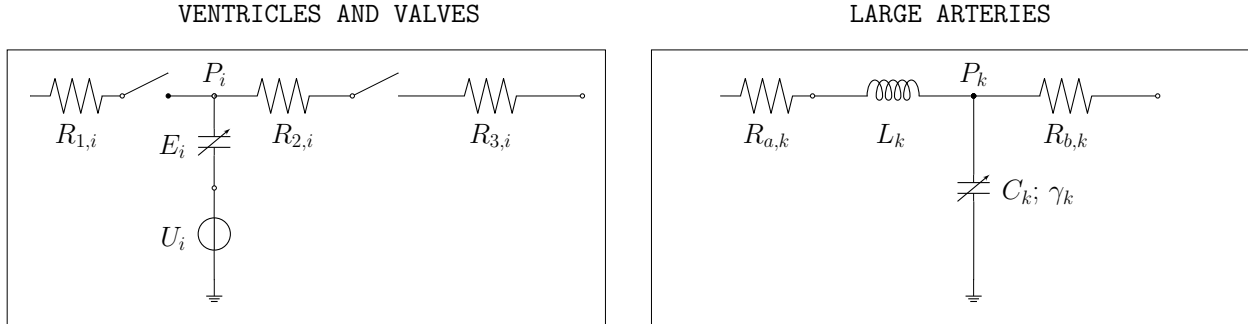


Figure 2.4: Basic components of the closed-loop model. *Left*: ventricles and valves; the subscript i is used to distinguish between left ($i = L$) and right ($i = R$) ventricles; P_i is the ventricular pressure; $R_{1,i}$, $R_{2,i}$ and $R_{3,i}$ are hydraulic resistances assumed to be constant; U_i and E_i characterize ventricular pumping, E_i representing the variable ventricular elastance. *Right*: large arteries; the subscript k is used to distinguish among different arterial segments, specifically aortic arch ($k = 3$), thoracic aorta ($k = 4$), abdominal aorta ($k = 5$), iliac arteries ($k = 6$) and cerebral arteries ($j = 14$); P_k is the pressure of the specific arterial segment; $R_{a,k}$ and $R_{b,k}$ are the hydraulic resistances representing viscous effects; L_k is the inductance representing inertial effects; C_k and γ_k represent elastic and viscoelastic properties of the arterial wall, respectively.

ARTERIAL SEGMENT	SEGMENT NODE	l [cm]	r [cm]	h [cm]
Ascending Aorta	2	4	1.44	0.158
Aortic Arch	3	5.9	1.25	0.139
Thoracic Aorta	4	15.6	0.96	0.117
Abdominal Aorta	5	15.9	0.85	0.105
Iliac artery	6	5.8	0.52	0.076
Carotid artery	14	20.8	0.39	0.064

Table 2.2: Geometrical parameters for the main arterial segments

2.2.4 Using the closed-loop model to simulate displacement, velocity and acceleration BCG signals

Following [28], the waveforms $V_k(t)$ representing the blood volumes occupying the cardiovascular compartment k at time t calculated via the closed-loop model can be utilized to estimate the displacement $d_y(t)$ of the center of mass of the human body at every heartbeat

NODE	y [cm]
1	0.5
2	-2
3	-7
4	20
5	35
6	45
7	-
8	-
9	-
10	0.5
11	-5
12	-
13	-
14	-10
15	-

Table 2.3: Anatomical meaning of the circuit nodes

in the head-to-toe direction as

$$d_y(t) = \frac{\rho_b}{M} \sum_{k=1}^K V_k(t) y_k \quad (2.28)$$

where ρ_b is the blood density, M is the total body mass, y_k is the distance between the compartment k and the plane of the heart valves and K is the total number of cardiovascular compartments considered in the model. In this work, we considered $K = 9$ compartments, whose y_k values are reported in Table 2.3. Multiplying Eq. (2.28) by M and differentiating with respect to time, we obtain the waveforms f_D , f_V and f_A , which are traditionally used in the BCG literature [17] and are defined as

$$f_D(t) = \rho_b \sum_{k=1}^K V_k(t) y_k \quad [\text{cm g}] \quad (2.29)$$

$$f_V(t) = \rho_b \sum_{k=1}^K \frac{dV_k}{dt}(t) y_k \quad \left[\frac{\text{cm}}{\text{s}} \text{g}\right] \quad (2.30)$$

$$f_A(t) = \rho_b \sum_{k=1}^K \frac{d^2V_k}{dt^2}(t) y_k \quad \left[\frac{\text{cm}}{\text{s}^2} \text{g}\right] \quad (2.31)$$

we notice that $f_d(t) = d_y(t) M$, $f_v(t) = v_y(t) M$ and $f_a(t) = a_y(t) M$.

2.3 BCG Technology

After defining the theoretical foundations of the pBCG concept and the modeling approach, in this section we provide an overview of the technological solutions that are utilized to record the BCG signal. Firstly, in Sec. 2.3.1 we describe the suspended bed, and then in Sec. 2.3.2 we provide an overview of the load cell system.

2.3.1 Suspended bed

The suspended bed utilized in this work is a replica of the suspended ballistocardiography bed originally designed by Burger et al [8], and is shown in Fig.2.5. This ultra-low frequency ballistocardiograph device is made of a lightweight foldable aluminum frame approximately 207 cm by 78 cm fixed on top of two lateral wood frames. The frame is suspended at four points from the ceiling with 3 m long steel cable of approximately 2.5 mm in diameter. The cables are kept parallel to each other, as done in [8]. To record the motion of the CoM, a three-axis accelerometer (Kionix EVAL-KXR94-2283 [21]) with 1 V/g sensitivity, was placed on the wood frame closer to the subject's head. A thin air mattress was placed on top of the aluminum frame, assuring that the total weight of the bed and all extra materials were kept at less than 8 Kg. In addition to the BCG signal, the ECG, SCG were recorded simultaneously. ECG signals were acquired via a 3-lead configuration, SCG signals were measured using a Kionix KXR94-2283 accelerometer, with 1000 mV/g sensitivity [21] placed on the subject's sternum. All signals were collected simultaneously using an AD Instrument PowerLab 16/35 data acquisition system [22].

2.3.2 Stationary Bed

The stationary bed utilized in this work is a twin-sized captain bed initially used for ballistocardiography with hydraulic bed sensors. To record the effects of the CoM motion in the form of forces exerted on the bed, we placed load cells beneath the posts of the bed. The load cells are from TE Connectivity (FX1901) with a maximum load capacity rating of 200 lbf. The signals from the load cells are preprocessed by a signal conditioning circuit. The load cells and the accompanying signal conditioning circuits are previously validated in [47, 2]. The signal conditioning circuit is comprised of an instrumentation amplifier and a second order low pass filter in Sallen and Key configuration. The cut-off frequency of the filter was 35 Hz [47].



Figure 2.5: Replica of the suspended ballistocardiography bed originally designed by Burger, et al. [8], utilized in the present work.

2.4 BCG Physics

Different devices for BCG measurement capture different kinematic aspects of the CoM motion depending on their physical characteristics. For this reason, in this section we introduce the concept of **measured BCG** (mBCG), which refers to the quantity that can be recorded with the sensing devices but do not necessarily directly correspond to the pBCG. A formal definition of the mBCG concept is provided in Sec. 2.4.1. Then, in Sec. 2.4.2 and 2.3.2 we describe a device-characteristic relationship between the mBCG and pBCG for both the load cell and the suspended bed.

2.4.1 Measured BCG signal (mBCG)

Different devices for BCG measurement capture different kinematic aspects of the CoM motion depending on their physical characteristics. In other words, the mBCG does not have a unique representation since different waveforms are produced by different devices, even though the signal source is the same pBCG. This concept can be formalized mathematically as follows:

Definition 2 (Measured BCG) Let us consider J different devices for BCG measurement. Each device j , with $j = 1, \dots, J$, provides a measured BCG (mBCG) represented by a

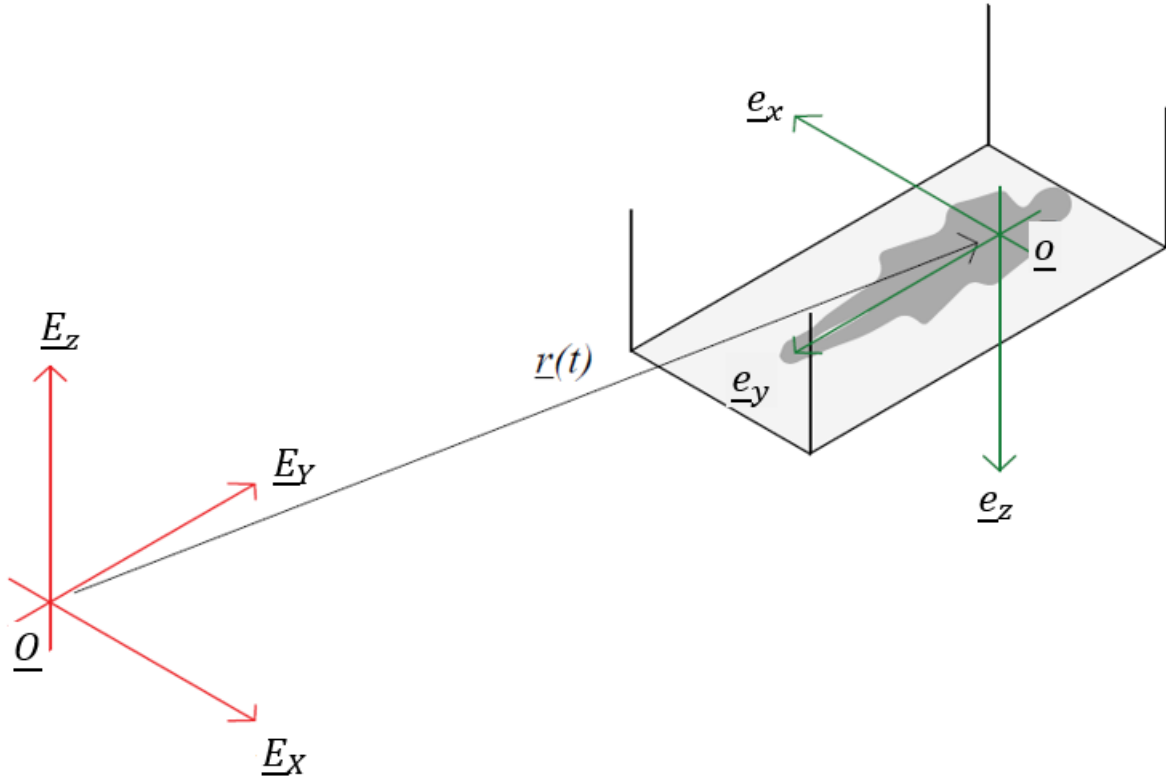


Figure 2.6: Reference systems to describe the CoM motion ON the suspended bed: $\mathcal{C} = \{\underline{O}, \underline{E}_X, \underline{E}_Y, \underline{E}_Z\}$ is a cartesian reference system that is fixed with the environment, whereas $c = \{\underline{o}, \underline{e}_x, \underline{e}_y, \underline{e}_z\}$ is a second reference system that moves with the body and that is centered on the CoM of the subject. $\underline{\mathbf{r}}(t)$ $\underline{\mathbf{r}}(t)$ denote the position of the origin of the frame of reference c that is centered on the individual center of mass.

vector-valued function $\underline{\omega}_j(t)$, which depends on the tensor $\underline{\underline{\varphi}}(t)$ representing the pBCG and on the physical parameters $\underline{\mathbf{s}}_j$ of the sensing device via a device-specific functional relationship $\underline{\mathcal{F}}_j$, namely

$$\underline{\omega}_j(t) = \underline{\mathcal{F}}_j(\underline{\underline{\varphi}}(t), \underline{\mathbf{s}}_j) \quad \text{for } j = 1, \dots, J. \quad (2.32)$$

2.4.2 Physics of the accelerometer on the suspended bed ($j = sb$)

To couple the concept of mBCG and pBCG two points needs to be addressed:

1. *how is the vector valued function $\underline{\omega}_j(t)$ obtained experimentally?*
2. *which are the forces produced by the CoM motion that give rise to $\underline{\omega}_j(t)$?*

Referring to point (1), when $j = sb$, $\underline{\omega}_{sb}(t)$ is obtained from the signal of a three-axis accelerometer. The kinematic variables in the x and y directions are directly measuring body

motion, whereas the reading in the z direction is constrained by the cables supporting the bed.

Then, to address point(2), i.e. to couple $\underline{\omega}_{sb}(t)$ with the kinematics of the CoM, we refer to Fig. 2.6. Here, $\underline{\mathbf{r}}(t)$ denote the position of the origin of the frame of reference c that is centered on the individual center of mass. Denoting the acceleration of the CoM of the human body as $\underline{\ddot{\mathbf{r}}}(t)$, we can write the 2-nd Newton law

$$M \underline{\ddot{\mathbf{r}}}(t) = \underline{\mathbf{F}}_{int} \quad (2.33)$$

where M is the total body mass, $\underline{\ddot{\mathbf{r}}}(t)$ is the acceleration of the CoM of the human body and $\underline{\mathbf{F}}_{int}$ are the internal forces that make the body move. It should be noted that $\underline{\ddot{\mathbf{r}}}(t)$ is measured with respect to the fixed cartesian reference frame $\underline{\mathbf{X}}$. Thus with respect to $\underline{\mathbf{x}}$, $\underline{\mathbf{F}}_{int}$ can be written as

$$\underline{\mathbf{F}}_{int} = \sum_{k=1}^K m_k \underline{\ddot{\mathbf{r}}}_k(t) \quad (2.34)$$

where k denotes the subregions in which we partition the domain Ω occupied by the human body (see Eq.2.23). Thus in the case of the suspended bed, provided that the accelerometer reference system is aligned with c , the acceleration recorded by the suspended bed, i.e. $\underline{\omega}_{sb}$, provide a signal close to the acceleration of the CoM, namely

$$\underline{\omega}_{sb}(t) = \underline{\ddot{\mathbf{r}}}(t) \approx [\hat{a}_x, \hat{a}_y] \quad (2.35)$$

where the hat symbol means that these are measured variables. Then, the signal of the three-axis accelerometer can be numerically integrated to calculate velocity and displacement. Overall, in this case $\underline{\mathcal{F}}_{sb}$ is an approximation of the identity with respect to the kinematic variables in the $x - y$ plane. This functional is invertible and allows direct reconstruction of the pBCG features in the $x - y$ plane.

2.4.3 Physics of the load cells system ($j = lc$)

In this case, $\underline{\omega}_{lc}(t)$ is obtained from the four load cell signals, which will be denoted as $R_i(t)$ with $i = 1, \dots, 4$ (see Fig. 2.7). To couple $\underline{\omega}_{lc}(t)$ with the kinematic of the CoM, we can firstly reconstruct $a_z(t)$ from $R_i(t)$ via the balance of forces in the z -direction

$$a_z(t) = \frac{g}{M_s} \left(\sum_{i=1}^4 R_i(t) - M_f - M \right) \quad (2.36)$$

where M is the total body mass, M_f is the mass of the bed frame and g is the acceleration of gravity. It is interesting to notice how the BCG features naturally available from the

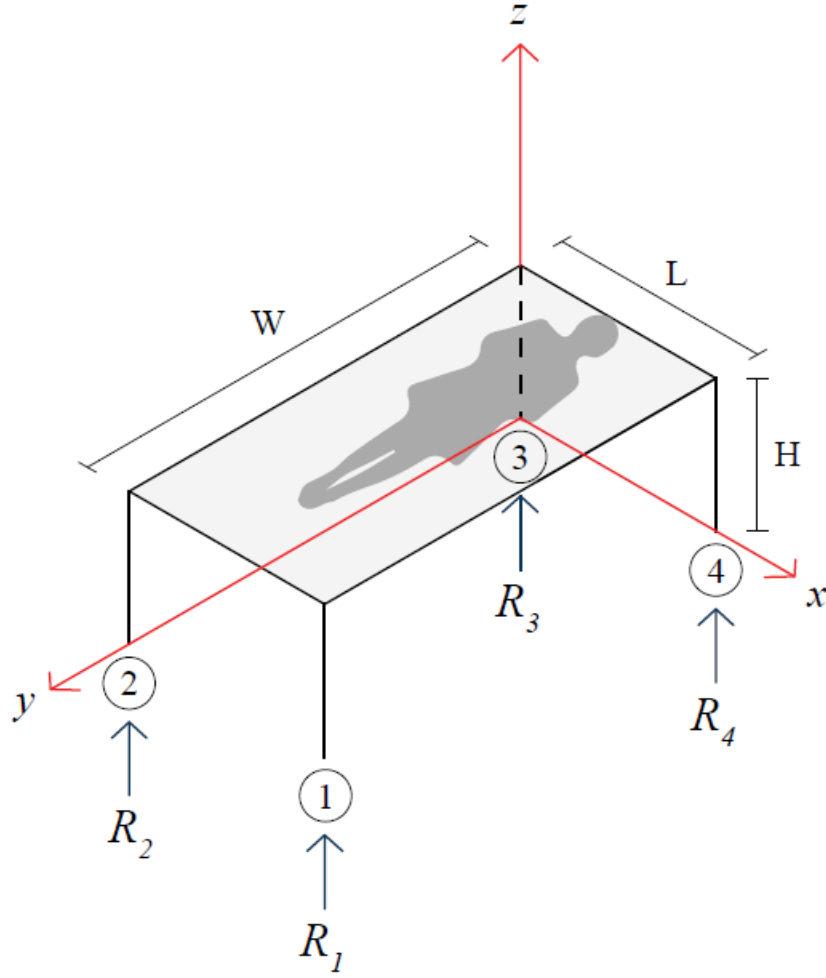


Figure 2.7: Reference systems to describe the CoM motion for the load cell: $\mathbf{X} = \{X, Y, Z\}$ is a cartesian reference system that is fixed with the environment, whereas R_i with $i = 1, \dots, 4$ are the signal recorded via the load cell signal.

load cells are in the z direction, which are truly complementary to those available via the suspended bed in the $x - y$ plane.

Then, $a_y(t)$ and $a_x(t)$ can be recovered utilizing the balance of the angular momentum with respect to the x -axis and y -axis respectively:

$$M H a_y(t) + g(M_f + M)d_y(t) = (R_1(t) + R_2(t))g L \quad (2.37)$$

$$M H a_x(t) + g(M_f + M)d_x(t) = (R_1(t) + R_4(t))g W \quad (2.38)$$

where M is the total body mass, M_f is the mass of the person lying on the bed, $d_x(t)$ and $d_y(t)$ are the displacement of CoM in the x and y direction, $a_x(t)$ and $a_y(t)$ are the displacement of CoM in the x and y direction, H is the height of the bed posts and L the length of the bed. In particular, the term $M_s H a_y(t)$ represents the **the thrust**, which is the

force, equal in magnitude and opposite in sign, resulting from the ejection of an accelerated mass in the systemic circulation, whereas $g(M_f + M)d_y(t)$ is the angular momentum given by **the weight**, which is the force, directed towards the ground, given by the product of the mass of the subject and the bed frame and the acceleration of gravity. Is it worth noting that the time-varying contribution given by the weight force is not due to a change in the mass of the subject, rather is produced by the change in the moment arm $d_y(t)$ of the weight force, which is not constant and depends on the CoM position.

Eq.2.36 - 2.38 represent a system of 2nd order, linear, non-homogeneous ordinary differential equations (ODEs) relating the measured load cell reactions (R_i with $i = 1, \dots, 4$) and the component of the pBCG tensor and can be rewritten as

$$a_y + \alpha^2 d_y = f_y \quad (2.39a)$$

$$a_x + \alpha^2 d_x = f_x \quad (2.39b)$$

$$a_z = f_z \quad (2.39c)$$

where

$$\alpha = \sqrt{\frac{(M_f + M)g}{MH}}, \quad f_y(t) = \frac{gL}{MH} (R_1(t) + R_2(t)) \quad (2.40)$$

$$f_x = \frac{gL}{MH} (R_1(t) + R_4(t)) \quad f_z = \frac{g}{M} \left(\sum_{i=1}^4 R_i(t) - M_f - M \right) \quad (2.41)$$

Overall, by solving 2.39 we can obtain the acceleration of the pBCG, which can be subsequently numerically integrated to calculate velocity and displacement. In this case $\underline{\mathcal{F}}_{lc}$ is invertible and, in addition, allows for direct reconstruction of the pBCG features in all the three directions.

2.4.4 Load cells under the bed posts ($j = lc$), numerical solution

We firstly obtain the analytical solution of 2.39b and 2.39c, which are both 2nd order, non-homogeneous, linear ODEs with just a different forcing terms. The solutions of the two ODEs is the CoM displacement in both x and y directions and can be formally defined as follow:

$$d_i = d^{\mathcal{H}} + d_i^{\mathcal{P}} \quad \text{with } i = \{x, y\} \quad (2.42)$$

where $d^{\mathcal{H}}$ is the solution of the associated homogeneous problem, whereas $d_i^{\mathcal{P}}$ with $i = \{x, y\}$ is the particular solution of the non-homogeneous ODE in the x and y direction. Since the roots of the associated homogeneous equation are two complex conjugate numbers $\pm i\sqrt{\alpha}$,

$d^{\mathcal{H}}$ can be obtained as

$$d^{\mathcal{H}} = c_1 \xi_1 + c_2 \xi_2 = c_1 \sin(\alpha t) + c_2 \cos(\alpha t) \quad (2.43)$$

Then, the particular solution $d_i^{\mathcal{P}}$ can be found utilizing the method of the variation of parameters. In particular, we seek a solution of the form

$$d_i^{\mathcal{P}} = \xi_1(t) v_1(t) + \xi_2(t) v_2(t) \quad \text{with } i = \{x, y\} \quad (2.44)$$

where v_1 and v_2 with $i = 1, 2$ are two unknown new function. Following the procedure outlined in [52], using the product rule to differentiate $d_i^{\mathcal{P}}$ twice, and then grouping the terms together, we get the following system of two equations in two unknowns

$$\dot{v}_1 \xi_1 + \dot{v}_2 \xi_2 = 0 \quad (2.45a)$$

$$\dot{v}_1 \dot{\xi}_1 + \dot{v}_2 \dot{\xi}_2 = f_i \quad (2.45b)$$

with $i = \{x, y\}$. Substituting 2.43 into Eq. 2.45, we get

$$\dot{v}_1 \sin(\alpha t) + \dot{v}_2 \cos(\alpha t) = 0 \quad (2.46a)$$

$$\dot{v}_1 \cos(\alpha t) \alpha - \dot{v}_2 \sin(\alpha t) \alpha = f_y \quad (2.46b)$$

Multiplying Eq. 2.46(a) by $\alpha \sin(\alpha t)$ and Eq. 2.46(b) by $\cos(\alpha t)$ and subtracting the two expressions we get

$$\dot{v}_1 = \frac{f_i \cos(\alpha t)}{\alpha} \quad (2.47)$$

Substituting Eq. 2.47 into Eq. 2.45(a) leads to

$$\dot{v}_2 = -\frac{f_i \sin(\alpha t)}{\alpha} \quad (2.48)$$

Knowing the analytical expression of \dot{v}_1 and \dot{v}_2 , we can compute v_1 and v_2 as

$$v_1 = \frac{1}{\alpha} \int_0^T f_i \cos(\alpha t) dt \quad (2.49a)$$

$$v_2 = -\frac{1}{\alpha} \int_0^T f_i \sin(\alpha t) dt \quad (2.49b)$$

Overall, the solution can be written as

$$\begin{aligned}
d_i(t) = & c_1 \cos(\alpha t) + c_2 \sin(\alpha t) + \sin(\alpha t) \cdot \frac{1}{\alpha} \int_0^T f_y(t) \cos(\alpha t) dt \\
& - \cos(\alpha t) \cdot \frac{1}{\alpha} \int_0^T f_i(t) \sin(\alpha t) dt \quad \text{with } i = \{x, y\}
\end{aligned} \tag{2.50a}$$

In addition, one can compute the analytical expression of $v_i(t)$ as follow

$$\begin{aligned}
v_i(t) = & c_1 \alpha \cos(\alpha t) - c_2 \alpha \sin(\alpha t) + \frac{\sin(\alpha t) \cos(\alpha t)}{\alpha} \cdot f_i + \\
& + \alpha \cos(\alpha t) \cdot \frac{1}{\alpha} \int_0^T f_i \cos(\alpha t) dt + \frac{\cos(\alpha t) \sin(\alpha t)}{\alpha} \cdot f_i + \\
& + \alpha \sin(\alpha t) \cdot \frac{1}{\alpha} \int_0^T f_i \sin(\alpha t) dt \quad \text{with } i = \{x, y\}
\end{aligned} \tag{2.51a}$$

Regarding the third equation in the z -direction, we can directly obtain a_z from the recordings on the load cell system utilizing 2.36. Then, both v_z and d_z can be obtained via a procedure of numerical integration, namely:

$$v_z(t) = \int_0^T a_z(t) dt \tag{2.52}$$

$$d_z(t) = \int_0^T v_z(t) dt \tag{2.53}$$

Chapter 3

CoM motion reconstruction for the suspended bed and load cell system

3.1 Introduction

The previous chapter defined the concept of **pBCG**, **mBCG** and their relationship in the case of the suspended bed and the load cells system under the bed post. In particular, we emphasized how, even though the signal source is the same **pBCG**, the **mBCG** has a different representation according to the sensing device. In this chapter we will utilize the physical relationship defined in the previous chapter to reconstruct the CoM motion and **pBCG** components on both the suspended bed and load cell system. For this purpose, we will combine *signal processing* and *numerical methods* to extract the signal of interest from the from the experimentally recorded signal on the sensing device. In particular, the former is needed to reduce the noise associated with the BCG measurements, remove the motion artifacts and respiration effects, whereas the latter is involved when reconstructing the velocity and displacement of the CoM in the case of the suspended bed, as well as in the solution of the ODEs for the load cell system reported in Eq. 2.40.

In addition, we will explore a template procedure, which refers to the procedure of averaging repeated measurements over several cardiac cycles. The template curve aims at: *(i)* smoothing the white noise and remove the motion artifacts, thus enhancing the signal-to-noise ratio, *(ii)* removing the respiration effects and *(iii)* providing a subject-specific representative signal over time that can unveil the patient-to-patient variability. In addition, the template procedure can be utilized to compare the signal recorded utilizing two different sensing devices for the same subject. Thus, this chapter has the following aims:

- **Signal processing**: to define the procedure needed to process the signal recorded on the suspended bed and the load cell system (Sec. 3.2)

ID	Gender	Age	Height [cm]	Weight [kg]	Systolic BP [mmHg]	Diastolic BP [mmHg]
1	Male	23	180	53.9	106.5	61.5
2	Female	26	162.5	48	99.7	66.7
3	Male	22	192.5	82.3	117.5	68.8

Table 3.1: Details of subjects involved in the CoM reconstruction project.

- **Template procedure:** to compute a representative template curve of the mBCG for the suspended bed and the load cell system(Section 3.2.2) ;
- **CoM reconstruction**to reconstruct the CoM motion in the case of the suspended bed and the load cells system (Section 3.3);

3.2 Methods

In this section, we firstly illustrate the method for acquiring ECG, SCG and BCG signals from the suspended bed and the load cell system (Section 3.2.1). Then, in Section 3.2.2 we outline the signal processing procedure applied to the signal recorded on the suspended bed, as well as the steps involved in the template curve generation. Similarly, Section 3.2.3 presents the procedure adopted to extract the pBCG components from the experimentally recorded signal on the load cell system, together with the template generation procedure.

3.2.1 Data acquisition and signal processing for ECG, SCG and BCG signals on a healthy subject

Three healthy volunteers were recruited for a data collection in a controlled laboratory settings. Firstly, each person was asked to lay still on a suspended bed system previously described in [15], while the ECG, SCG and BCG signals were recorded simultaneously. ECG signals were acquired via a 3-lead configuration, SCG signals were measured using a Kionix KXR94-2283 accelerometer, with 1000 mV/g sensitivity [21] placed on the subject’s sternum, and BCG signals were acquired with a three-axis accelerometer from Kionix with 1000 mV/g sensitivity placed on the bed frame of the suspended bed. All signals were collected simultaneously using an AD Instrument PowerLab 16/35 data acquisition system [22]. In addition to these signal, blood pressure measurements were taken for each subject at the beginning and at the end of the data acquisition. The pressure recordings were acquired with a commercial arm cuff blood pressure.

Then, the participant was asked to lay on their back on the bed where the load cell system had been previously installed. To reduce the distortion to the subject’s pBCG, the

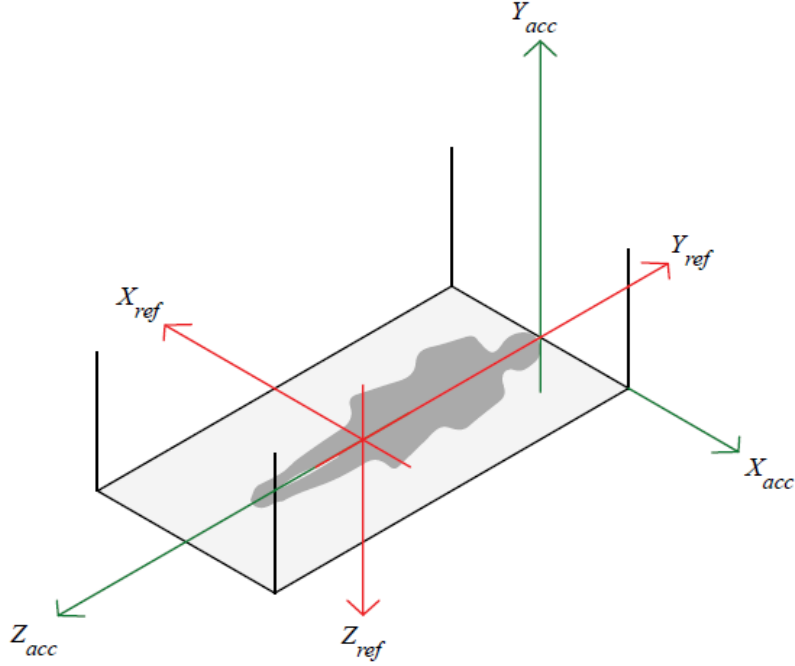


Figure 3.1: Reference system for the recordings on the suspended bed. Red: reference system utilized in the present work, in agreement with the conventions for presentation or reproduction of vector ballistocardiographic records (red arrows) [40]. Green: Accelerometer reference system.

recordings were performed with no mattress. After measuring participant’s blood pressure, the ECG, SCG and BCG signals were recorded simultaneously for 5 minutes. The ECG and SCG signal were measured using the same device as before, whereas the details regarding the load cell system are reported in Section 2.3.2. All signals were collected simultaneously using an AD Instrument PowerLab 16/35 data acquisition system [22]. The age, sex and value of the blood pressure (BP) for each subject involved in the study are reported in Table 3.1. The cuff BP measurement is considered as the ground truth (GT).

3.2.2 Signal processing and template generation for the suspended bed

Considering a continuous recording in the interval $[0, T]$, with the three axis accelerometer on the suspended bed we recover

$$a_x^V(t), a_y^V(t) \quad \text{with } t \in [0, T], \quad (3.1)$$

where $a_x^V(t)$ represents the signal recorded in the right-to-left shoulder direction, whereas $a_y^V(t)$ represents the signal recorded in the head-to-toe direction. The superscript V empha-

sizes that the acceleration is recorded in voltage. The acquired signals are then processed to extract the pBCG signal with the the following procedure:

1. **Reference system alignment:** Fig. 3.1 reports the reference system of the bed accelerometer (green arrows), and the conventions for presentation or reproduction of vector ballistocardiographic records (red arrows) [40]. For the remainder of the discussion, we adopt the conventional system. Thus, the signal recorded on the suspended bed is multiplied by a -1 factor in both the x and y direction;
2. **Unit of measurement conversion and filtering:** once both $a_x^V(t), a_y^V(t)$ are aligned to the conventional reference system, they are converted into an acceleration via the following linear relationship [21]

$$a_k = \frac{(a_k^V(t) - \text{offset})}{S} \quad \text{with } k \in \mathcal{K} = \{x, y\} \quad (3.2)$$

where $\text{offset} = 2.5$ [mV] and $S = 1$ [mV/g] [21]. Then, a fixed cut-off band-pass filters is applied to $a_k(t)$ with $k \in \mathcal{K}$ to remove baseline variations associated with respiration and high frequency noise associated with the measurement.

3. **Segmentation :** $a_x(t)$ and $a_y(t)$ are then segmented utilizing the R-peaks of the ECG signal as reference events. The R-peaks were detected using the standard Pan-Tompkins algorithm [21]. The resulting single beat waveform, denoted as a_k^i with $k \in \mathcal{K}$, are grouped into the vector valued function $\mathcal{T}_{a,k}$, namely

$$\mathcal{T}_{a,k} = \{a_k^i(t) : i \in [0, N]\} \quad \text{with } k \in \mathcal{K}, \quad (3.3)$$

where a_k^i with $k \in \mathcal{K}$ are the individual curves resulting from the repetitive motion of the CoM, whereas N is the number of heart beats in the time T of the continuous recording.

4. **Integration procedure to recover pBCG velocity and displacement:** once $\mathcal{T}_{a,k}$ has been obtained, the velocity and displacement of the CoM can be recovered via an integration procedure.

$$v_k^i(t) = \int_0^T a_k^i(t) dt \quad \text{with } i = 1, \dots, N \quad k \in \mathcal{K} \quad (3.4)$$

$$d_k^i(t) = \int_0^T v_k^i(t) dt \quad \text{with } i = 1, \dots, N \quad k \in \mathcal{K} \quad (3.5)$$

Then, the individually segmented pBCG velocity and displacement are grouped into the vector-valued vector $\mathcal{T}_{v,k}$ and $\mathcal{T}_{d,k}$, respectively.

Once the processed pBCG curves are extracted utilizing the described procedure, a representative BCG waveform, or template, of the recorded a_y and a_x is produced. The adopted procedure leverages on four main steps that are described next:

1. **Padding** : the pad is utilized to cut all the segments at certain distances after the reference event. In the present work, we utilized the median heart beat duration for each subject, denoted by T_{median} , to make all the $a_k^i \in \mathcal{T}_{a,k}$ of equal length starting from the R-peak of ECG. This approach helps saving the timing information of the main waveform peaks, even though the final part of each waveform is lost during the segmentation strategy.
2. **Signal Alignment**: The signal alignment is a two-fold procedure involving (i) the centroid calculation and (ii) the alignment to the centroid. Firstly, the mean waveform, which does not necessarily belongs to $\mathcal{T}_{a,k}$, is computed as

$$\bar{a}_k = \frac{1}{N} \cdot \sum_{i=1}^N a_k^i(t) \quad \text{with } t \in [0, T_{median}] \quad (3.6)$$

$$i = 1, \dots, N, k \in \mathcal{K} \quad (3.7)$$

Then, the centroid is computed as

$$a_k^C(t) = \arg \min_{i \in \mathcal{T}_{a,k}} a_k^i = \{a_k^i \mid d(a_k^i, \bar{a}_k(t))\} \quad \text{with } i = 1, \dots, N \quad k \in \mathcal{K} \quad (3.8)$$

To align the signals, the waveform $a_k^i \in \mathcal{T}_{a,k}$ are shifted based on their correlation value to the centroid a_k^C . Finally, a new ensemble $\mathcal{T}_{a,k}^A$ is produced discarding the waveform $f_{a,k}^i \in \mathcal{T}_{a,k}$ with a correlation below 0.4 and lag-time above 0.4 s.

3. **Definition of the BCG acceleration representative**: once the collection of aligned signal $\mathcal{T}_{a,k}^A$ with $k \in \mathcal{K}$ is produced, several strategies may be adopted to compute the actual representative curve, or template. In this case, we utilized the procedure described at step 3 for the centroid computation. More precisely, we firstly computed the mean waveform, denoted as $\overline{a_k(t)} \in \mathcal{T}_{a_k}^A$ and then the template curve is computed as

$$a_k^T(t) = \arg \min_{i \in \mathcal{T}_{a,k}^A} a_k^i = \{a_k^i \mid d(a_k^i, \overline{a_k(t)})\} \quad \text{with } i = 1, \dots, N \quad k \in \mathcal{K} \quad (3.9)$$

4. **Definition of the BCG velocity and displacement representative**: once $a_k^T(t)$ has been obtained, the template curve for the velocity of the CoM can be recovered via an integration procedure, namely

$$v_k^T(t) = \int_0^T a_k^T(t) dt \quad \text{with } k \in \mathcal{K} \quad (3.10)$$

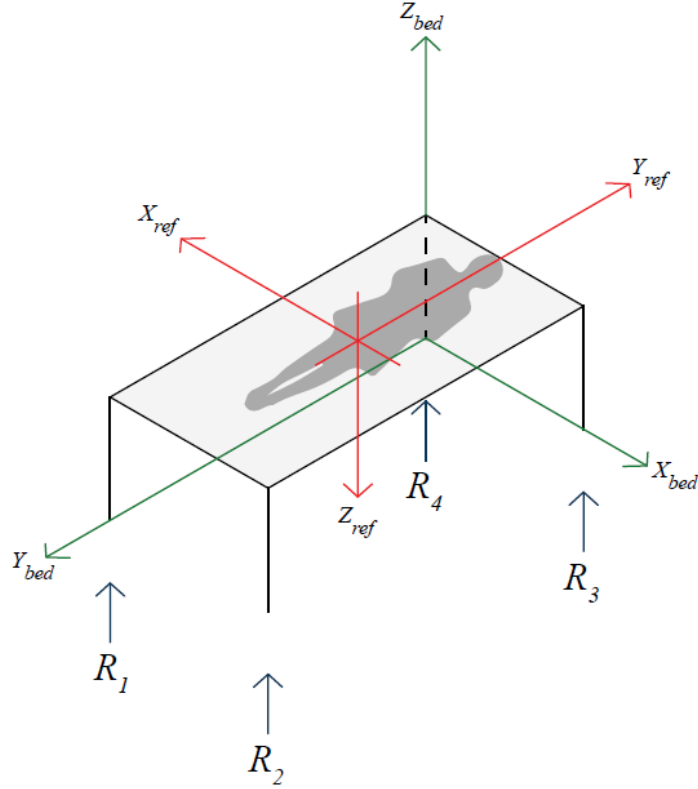


Figure 3.2: Reference system for the recordings on the load cell system. Red: reference system utilized in the present work, in agreement with the conventions for presentation or reproduction of vector ballistocardiographic records (red arrows) [40]. Green: Reference system adopted to recover the pBCG signal from the signal recorded on the load cell system.

Similarly, the template curve for the displacement of the CoM can be recovered integrating $f_v^T(t)$, namely

$$d_k^T(t) = \int_0^T v_k^T(t) dt \quad \text{with } k \in \mathcal{K} \quad (3.11)$$

It is worth noting that, before any integration procedure, we removed the best straight-fit line from the data utilizing the `detrend` function in Matlab. By so doing, we were able to account remove any trend present in the curve.

3.2.3 Signal processing and template generation for the load cell system

Considering a continuous recording in the interval $[0, T]$, with the load cell system we recover R_j^V with $j = 1 \dots 4$, where the superscript V emphasize that the acceleration are recorded in voltage. The acquired signal are then processed to extract the pBCG signal with the the following procedure:

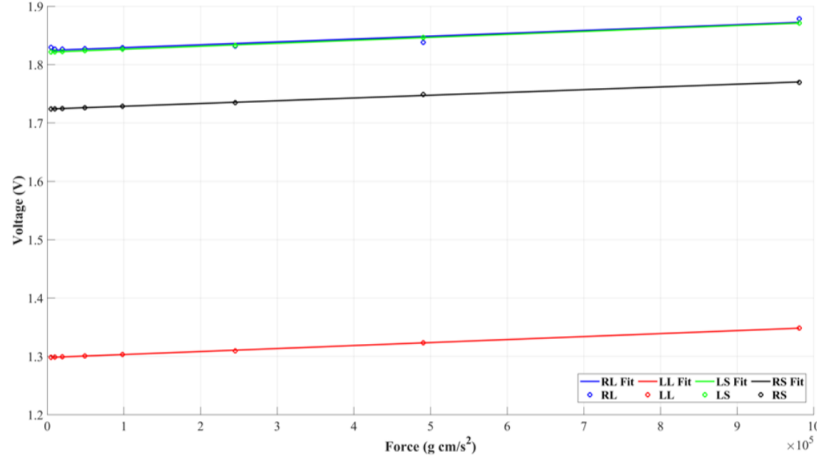


Figure 3.3: Average value of the recorded R_j^V plotted against the known masses.

1. **Load cells constitutive equation:** to convert R_j^V from a voltage into a mass, we initially need to define a constitutive equations relating the measured voltage to the corresponding mass measured at the load cells j , with $j = 1, \dots, 4$. For this purpose, we utilized an experimental linear regression method [2, 1]. In a condition of empty bed, 8 masses of known mass (5, 10, 20, 50, 100, 250, 500 and 1000-gram) were placed upon each bed posts and two session of 10 minute recording were performed. The average value of the recorded R_j for each bed post, denoted as \overline{R}_j , was then plotted against the known masses, and the results are reported in Figure 3.3. A linear relationship is observed between the recorded voltage \overline{R}_j and the known masses, which can be formally described as:

$$R_j^V = \frac{m_j \cdot M_m + b_j}{g} \quad (3.12)$$

where R_j^V is the measured voltage due to the force detected by each load cell (units: Volt) for the bed post j with $j = 1 \dots 4$, M_m is the m-mass utilized to obtain the load cell constitutive equation, whereas m_j and b_j are the regression results for the slope and vertical axis intercept of the fitted curves on the measurement data. Notably, Eq 3.12 represents the constitutive equation relating the recorded voltage and the measured mass for each load cell.

2. **Unit of measurement conversion and filtering:** utilizing Eq. 3.12, $R_j^V(t)$ are converted into a mass as follow

$$R_j = \frac{R_j^V(t) \cdot g - b_j}{m_j} \quad j = 1, \dots, 4 \quad (3.13)$$

where R_j (Unit: kg) is the recorded signal for the load cell j , whereas m_j and b_j are the slope and the intercepts previously obtained for the load cell j . Then, a fixed

cut-off band-pass filters is applied to R_j to remove baseline variations associated with respiration and high frequency noise associated with the measurement.

3. **Segmentation** : R_j is then segmented utilizing the R-peaks of the ECG signal as reference events. The R-peaks were detected using the standard Pan-Tompkins algorithm [21] and the resulting single beat waveforms are grouped into the vector valued function $\mathcal{T}_{R,j}$, namely

$$\mathcal{T}_{R,j} = \{R_j^i(t) : i \in [0, N]\} \quad \text{with } j = 1, \dots, 4, \quad (3.14)$$

where $R_j^i(t)$ are the individual curve resulting from the repetitive motion of the CoM, whereas N is the number of heart beats in the time T of the continuous recording.

4. **Computation of the pBCG kinematic components**: having computed the four vector valued $\mathcal{T}_{R,j}$ function, the displacement, velocity and acceleration of the pBCG can be computed utilizing the numerical solution of the system 2.40. More precisely, by solving Eq.2.36 we obtain a vector valued function $\mathcal{T}_{a,z}^{LC}$ representing the collection of segmented acceleration in the z-direction, that can be integrated to obtain $\mathcal{T}_{v,z}^{LC}$ and $\mathcal{T}_{d,z}^{LC}$. Interestingly, by solving Eq.2.50, we recover $\mathcal{T}_{d,y}^{LC}$ and $\mathcal{T}_{d,x}^{LC}$, which represent the collection of segmented accelerations in the y and x direction, respectively. Then, solving Eq. 2.51, we can obtain $\mathcal{T}_{v,y}^{LC}$ and $\mathcal{T}_{v,x}^{LC}$, as well as $\mathcal{T}_{a,y}^{LC}$ and $\mathcal{T}_{a,x}^{LC}$.
5. **Reference system alignment**: Fig.3.2 reports the reference system utilized to write the balances of forces and angular momentum (green arrows), and the conventions for presentation or reproduction of vector ballistocardiographic records (green) [40]. For the remainder of the discussion, we adopt the conventional system.

Once the processed pBCG curves are extracted utilizing the described procedure, the same steps outlined in Section 3.2.2 at point 3, 4 and 5 are utilized to obtain the template representative curve for the acceleration, velocity and displacement.

3.3 Results

This section is organized as follow. Firstly, we reconstruct the pBCG kinematic components from the mBCG signal recorded on the suspended bed (Sec. 3.3.1) and the load cell system (Sec. 3.3.2). Then, in Sec.3.3.3 we compare the BCG waveforms obtained with the suspended bed and the load cell system in the head-to-toe direction and right-to-left shoulder direction for each subject in the study.

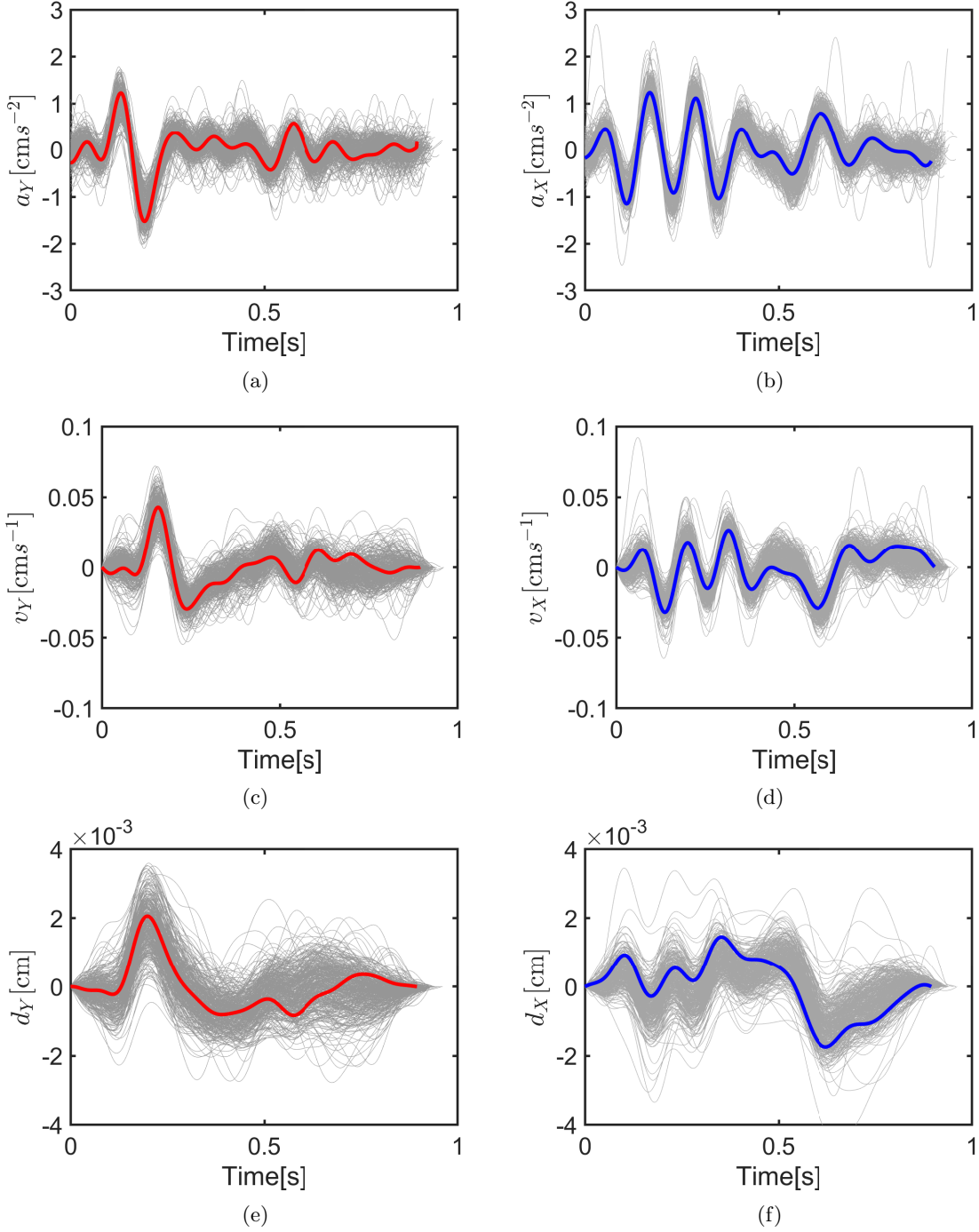


Figure 3.4: Recording on one subject of the y component of the pBCG tensor (Left) and the x component of the pBCG tensor (Right): (a): experimentally recorded a_y (grey curve) and computed template a_y^T (red curve), (c)- (e) numerically computed v_y and d_y (grey curve) via an integration process and computed template v_y^T and d_y^T . (b), experimentally recorded a_x (grey curve) and computed template a_x^T (blue curve), (d)-(f): numerically computed v_x and d_x (grey curve) via an integration process and computed template v_x^T and d_x^T (blue curve)

3.3.1 Reconstructed pBCG signal from the suspended bed

Fig. 3.4 reports the collection of the segmented waveforms recorded on the suspended in both the y direction (left) and in the x direction (right). The directly available features available with the suspended bed, i.e. the accelerations of the CoM, are reported in the top panel, whereas velocity and displacement are shown in the middle and bottom panel, respectively. Firstly, we can notice that (i) a_y exhibits the I, J, K complex characterizing the a_y waveform reported in the literature, (ii) both a_y and a_x curves shows larger amplitude in the initial part of the heart beat, whereas several oscillations in both directions can be detected in the diastolic part of the heart beat. Interestingly, although both v_y and d_y still maintain a larger prominent peak in the initial part of the heart beat, v_x and d_x present a flatter signal without a detectable prominent peak. In addition, as the integration in time proceeds, the bundle of curves grows in amplitude. The reason behind the observed behavior may be either numerical, i.e. an amplification in the amplitude of each single curve due to the process of numerical integration, or may reside in a physiological nature in the signal, i.e. the displacement is the smallest signal in magnitude and is significantly affected by small cardiovascular variations among each heart beat. The observed amplification of the pBCG can be in part mitigated by considering the template procedure described in Section 3.2.2. Indeed, superimposed to the measured and reconstructed signals in the x and y direction, Fig. 3.4 reports the computed template for each kinematic component of the pBCG. Each template curve remains within a certain approximation in the center of the ensemble, thus providing an average representative curve over the recording window of the pBCG components. The obtained curve may be useful, among the other, when reconstructing the CoM motion in the longitudinal-lateral plane. Fig. 3.8a-3.8b reports the template curve for the displacement in the x and y direction (black curve) and one d_x and d_y waveforms extract from the recording (blue curve). d_y^T and d_y present a similar waveform for almost the entire heartbeat, whereas larger differences can be observed among d_x and d_x^T in the diastolic part. This difference appears when reconstructing the CoM motion in the $x - y$ plane in Fig. 3.8c. Most notably, a "8-shape" can be detected, where the upper loop occurs during the systolic part of the representative heart beat, as indicated by the purple reference point, while the second loop occurs at the beginning of the diastolic wave (green point).

3.3.2 Reconstruction of the 3D pBCG signal from the load cell system

Fig. 3.6 reports the vector valued function $\mathcal{T}_{R,j}$ with $j = 1, \dots, 4$ representing the segmented signal collected on the load cell system for subject 1. The largest magnitude of the signal is observed with $\mathcal{T}_{R,3}$, which corresponds to the load cell located close to the left shoulder of the subject. Interestingly, $\mathcal{T}_{R,3}$ shows a prominent positive peak in the initial part of the waveform, whereas in $\mathcal{T}_{R,1}$ and $\mathcal{T}_{R,2}$ a negative peak is observed. In addition, these

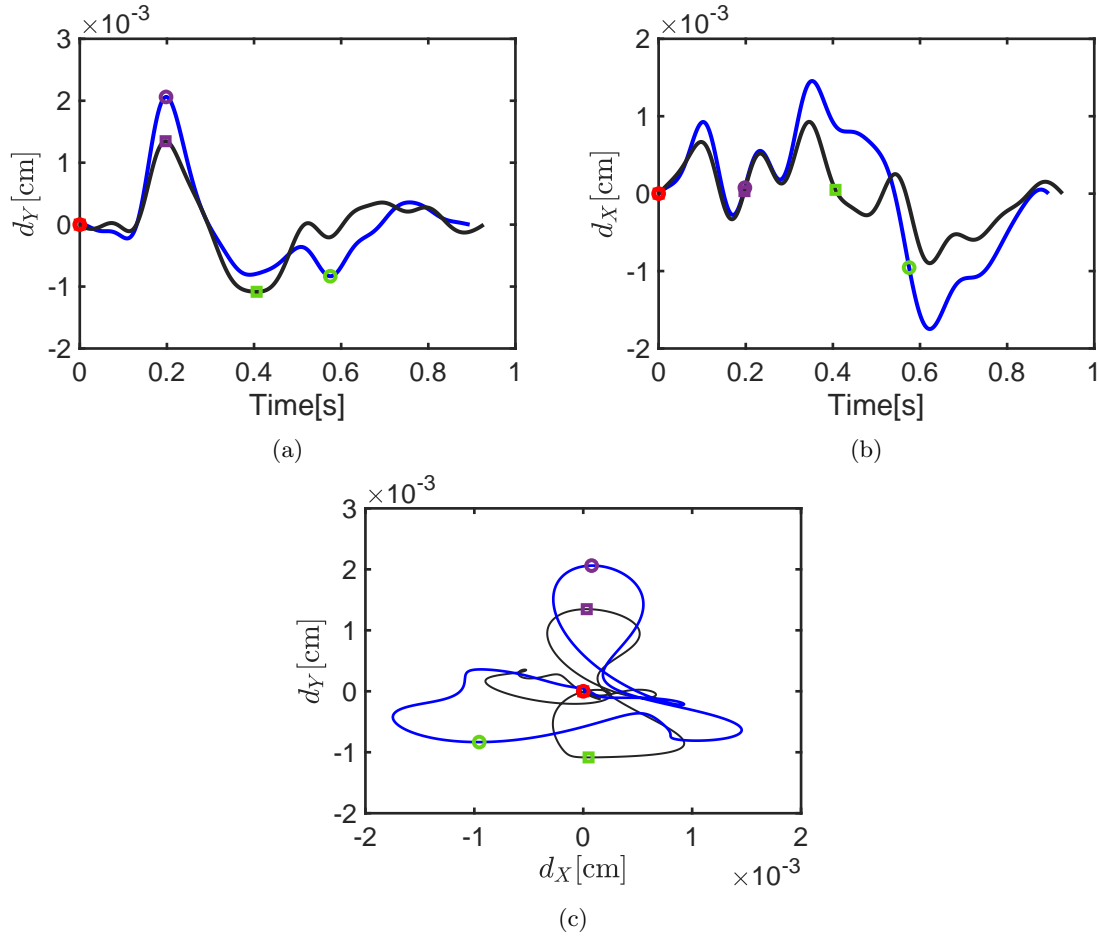


Figure 3.5: (a): d_y in one heart beat (black curve) and template curve d_y^T (blue curve). The colored circles indicates some reference points for d_y , whereas the colored squares indicates some reference points for d_y^T . (b): d_x in one heart beat (black curve) and template curve d_x^T (blue curve). (c) CoM motion in the lateral-longitudinal plane.

two signals are very similar both in term of shape and magnitude. Fig.3.7 reports the reconstructed 9 kinematic components of the pBCG reconstructed from the load cell signal: each column represents a different direction of the space (y , x and z from left to right), whereas in the rows the acceleration, velocity and displacement are reported from top to bottom, respectively. Firstly, we can notice that the z component is the smallest in terms of amplitude, with the displacement d_z presenting only small variation in the order of 10^{-4} . As for the suspended bed, the y -direction demonstrates a prominent peak in the systolic wave for all the three kinematic components, whereas the waveforms in the x -direction present a flatter signal without a detectable prominent peak. Fig. 3.8 reports the template curve for the displacement in the x and y direction (black curve) and one d_x and d_y waveforms extract from the recordings. d_y^T and d_y present a similar waveform for almost the entire heartbeat, whereas larger differences can be observed among d_x and d_x^T in the diastolic part. This

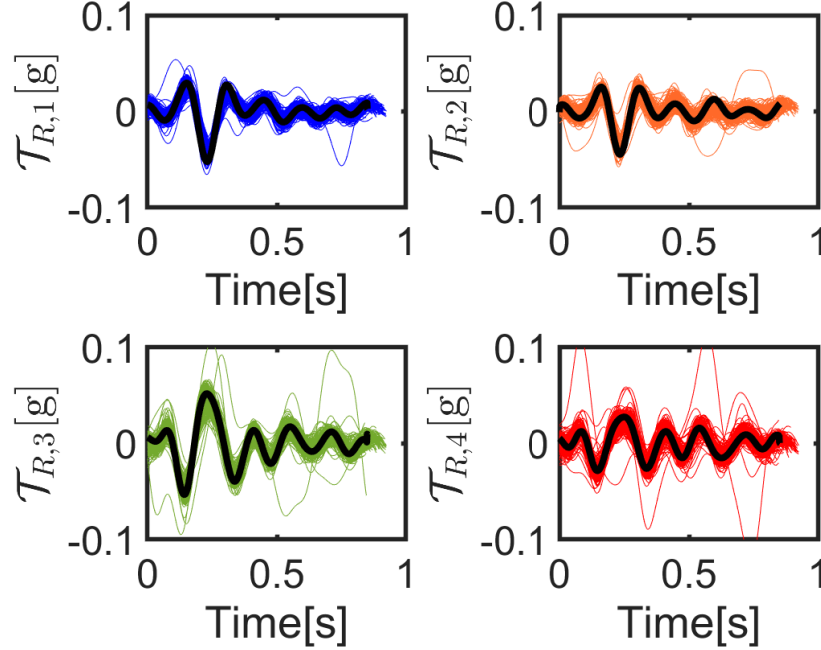


Figure 3.6: Vector valued function $\mathcal{T}_{R,j}$ with $j = 1, \dots, 4$.

difference appears when reconstructing the CoM motion in the $x - y$ plane in Fig. 3.8c. Most notably, a "8-shape" can be detected also for the signal on the load cell system. In addition, with the load cell we can reconstruct the 3D CoM motion, which has been reported in Fig.3.9. Interestingly, the 8-shape observed in the $x-y$ plane is still visible and, even though the displacement in the z direction is the smallest in terms of magnitude, we can observe that actually the CoM initially moves upward (green point corresponding to first valley in d_y), before moving significantly downward (purple square) and then slowly returning toward zero in the final part of the heart beat. It is worth noting that, utilizing the suspended bed we can reconstruct a two-dimensional CoM motion, whereas the complete three-dimensional CoM motion can be obtained utilizing the load cell system.

3.3.3 Towards an individual-specific pBCG

Table 3.2 reports the component of the pBCG tensor in the y direction for three subjects and is organized as follow: (i) each column represents a different subject involved in the study, identified as i , with $i = 1, \dots, 3$, (ii) the top row reports the reconstructed individual pBCG acceleration $a_{y,i}$, (iii) the middle row reports the reconstructed individual pBCG velocity $v_{y,i}$ and (iv) the bottom row reports the reconstructed individual pBCG displacement $d_{y,i}$. In addition, in each panel the red curve represents the collection of single beat waveform signal reconstructed from the suspended bed, i.e. $\mathcal{T}_{a,y}$, $\mathcal{T}_{v,y}$ and $\mathcal{T}_{d,y}$, whereas the collection of single

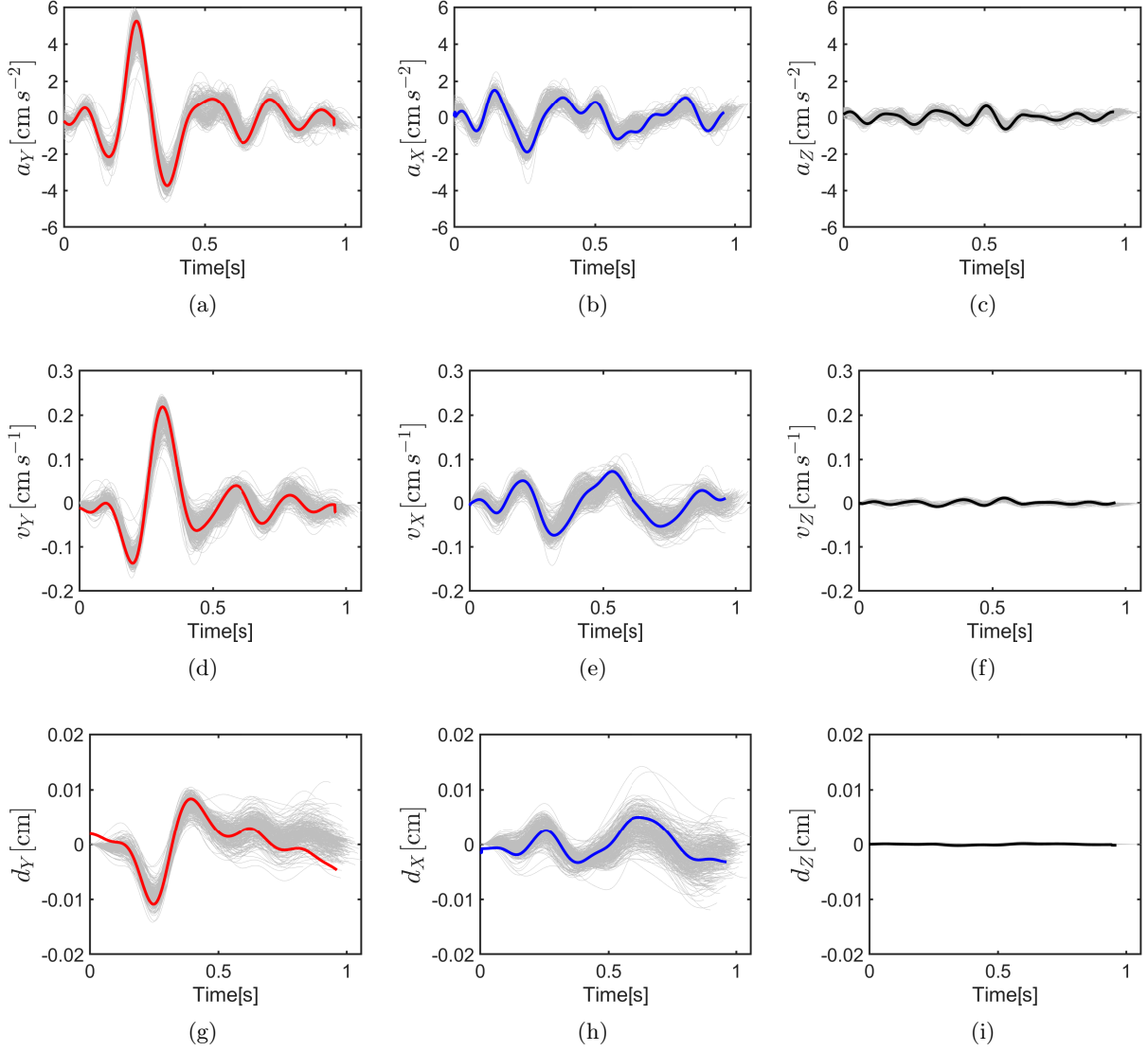


Figure 3.7: Recording on one subject of the y component of the pBCG tensor (Left) and the x component of the pBCG tensor (Right): (a): experimentally recorded a_y (grey curve) and computed template a_y^T (red curve), (c)- (e) numerically computed v_y and d_y (grey curve) via an integration process and computed template v_y^T and d_y^T . (b), experimentally recorded a_x (grey curve) and computed template a_x^T (blue curve), (d)-(f): numerically computed v_x and d_x (grey curve) via an integration process and computed template v_x^T and d_x^T (blue curve)

beat waveform signal obtained from the load cell, i.e. $\mathcal{T}_{a,y}^{LC}$, $\mathcal{T}_{v,y}^{LC}$ and $\mathcal{T}_{d,y}^{LC}$ is reported in black. For all the three subjects involved in the study, we can notice that the reconstructed kinematic components are within the same order of magnitude and they both present a similar shape. However, we can notice a delay in the reconstructed acceleration from the load cell signal, as well as an amplification in the magnitude if compared with the pBCG reconstructed from the suspended bed. This observation persists in all the three subjects.

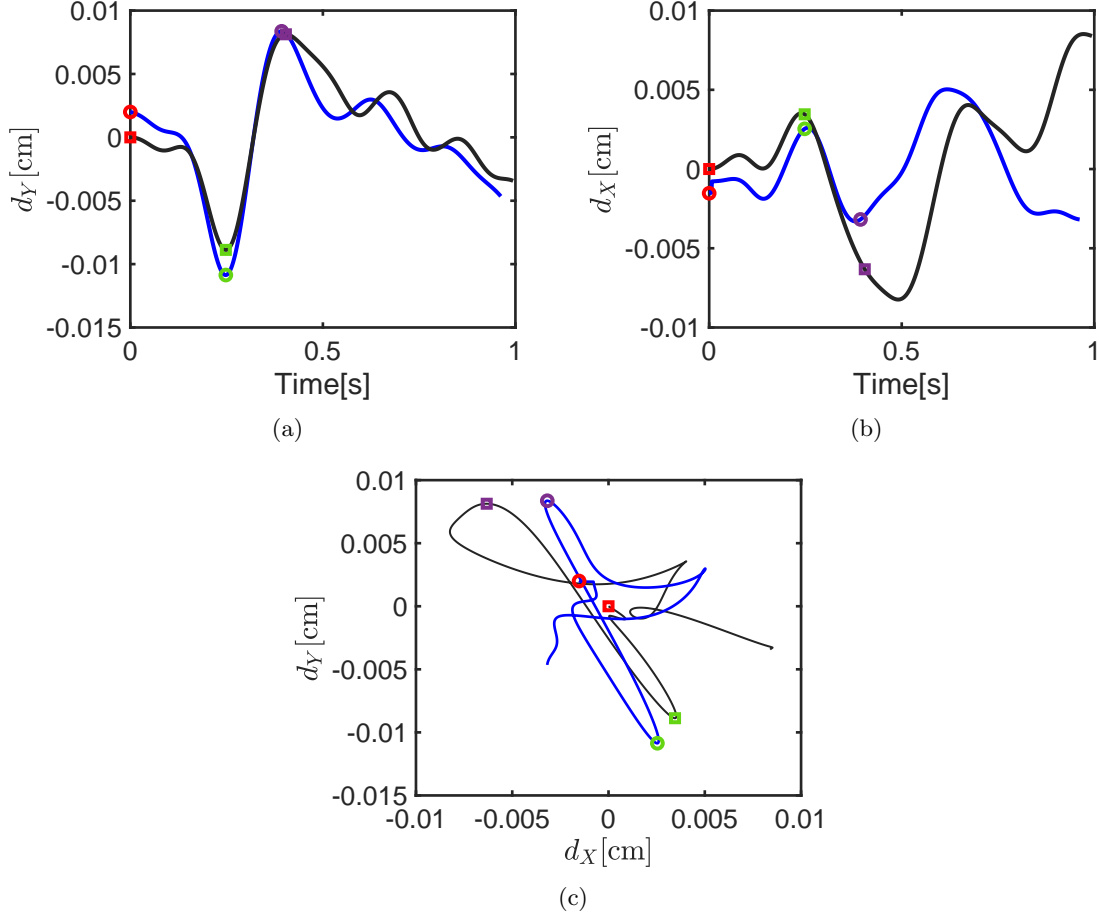


Figure 3.8: (a): d_y in one heart beat (black curve) and template curve d_y^T (blue curve). The colored circles indicates some reference points for d_y , whereas the colored squares indicates some reference points for d_y^T . (b): d_x in one heart beat (black curve) and template curve d_x^T (blue curve). (c) CoM motion in the lateral-longitudinal plane.

A similar behavior can be noticed for the velocity and displacement. In addition, $\mathcal{T}_{d,y}^{LC}$ presents a deeper first valley if compared to $\mathcal{T}_{d,y}$. Table 3.3 reports the same comparison in the x direction, where we notice a good agreement in the acceleration and velocity for subject 2 and 3. When considering the displacement, in general a more noisy signal can be observed with a noticeable difference in the shape. Indeed, the displacement BCG has the smallest amplitude and, for this reason, is largely affected by the noise associated with the measurements. To address this issue, we could consider the template and a smaller subset comprising the waveform with a high correlation and low lag time with the template (as it will be done in the next chapter). By so doing, we can have representative ensemble of pBCG waveforms for each subject where the noise associated with recording is minimized.

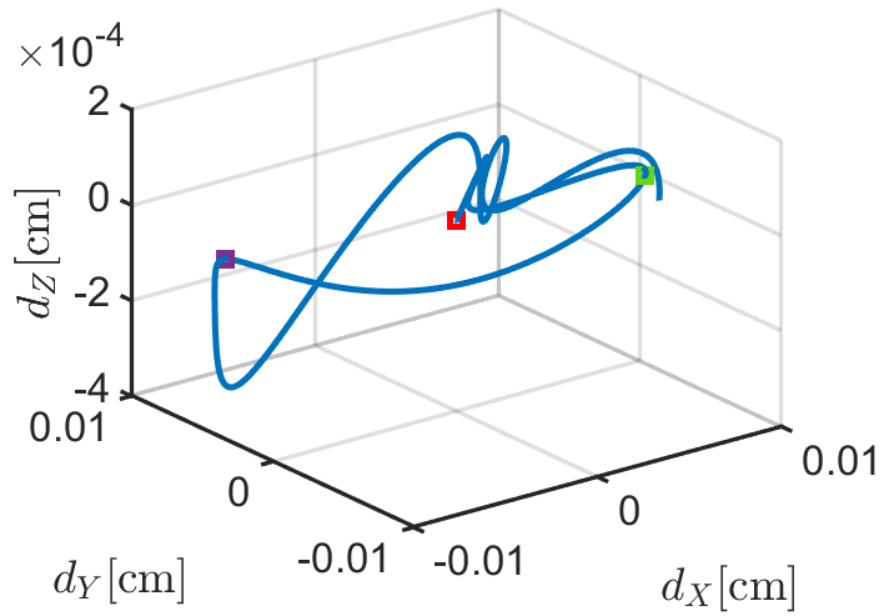


Figure 3.9: 3D motion as reconstructed from the signal recorded on the load cell system.

3.4 Conclusion

In this section, leveraging the BCG theoretical foundation defined in Chapter 2, we reconstructed the CoM motion utilizing the suspended bed and the load cell system. Combining the physics of the instrument and the physiology with signal processing and numerical methods techniques we were able to recover the component of the pBCG tensor in physical units and obtain a significant agreement in terms of order of magnitude from two different sensing devices. The velocity and acceleration reconstructed in the x direction for two subjects demonstrated a good alignment, whereas an amplification and shift appear when comparing the timing and magnitude of the reconstructed pBCG signal in the y direction. Although further works still to be done and the results are not conclusive, this work paves the way towards the concept that the pBCG does not depend on the sensing device, but it is actually specific to the physiology of the individual. Thus, there is hope for a standardization of the BCG signal, which could be actually crucial to make this technology utilized in a clinical settings.

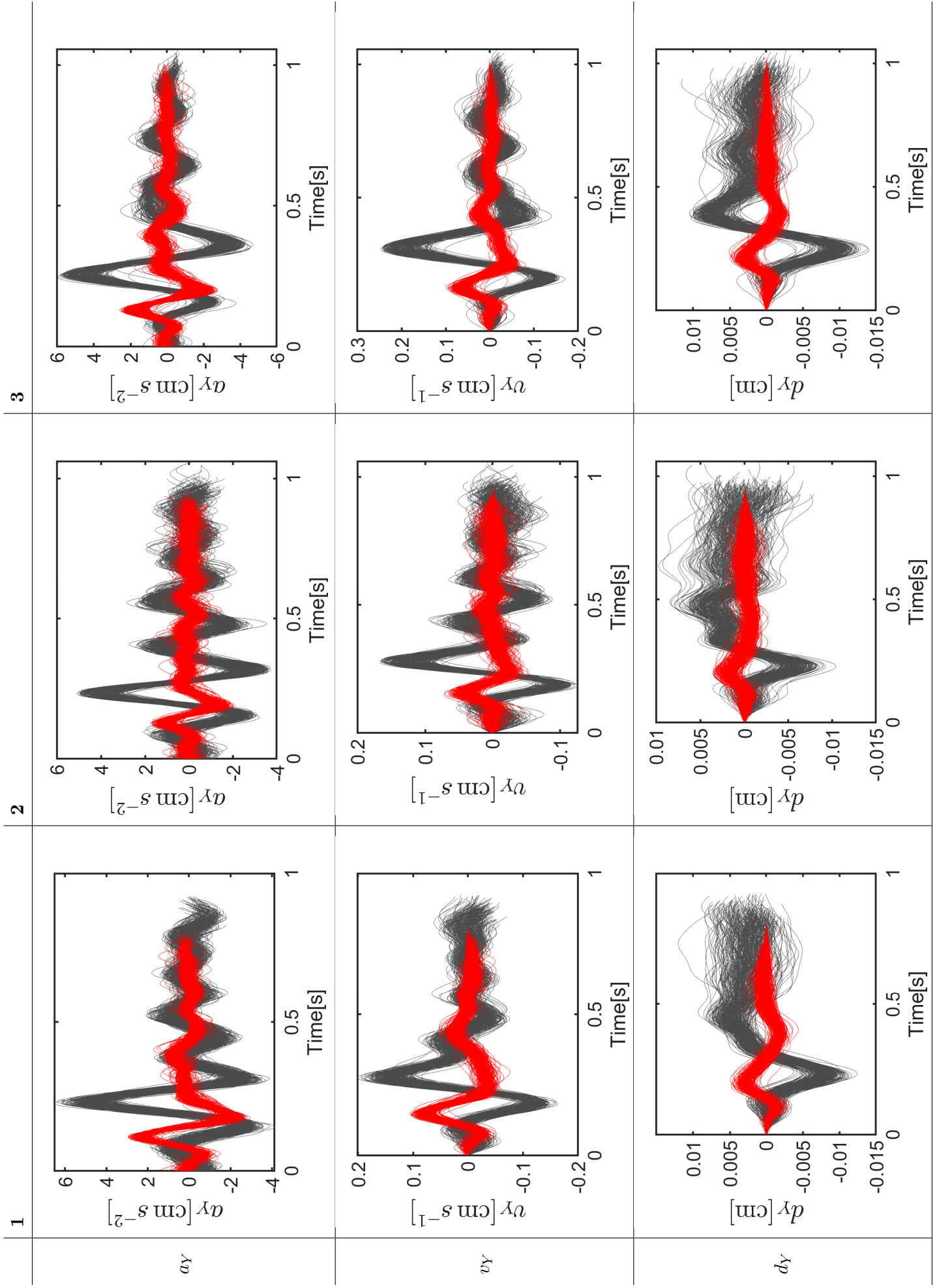


Table 3.2: Comparison between the reconstructed longitudinal acceleration a_Y , velocity v_Y and displacement d_Y for three subjects.

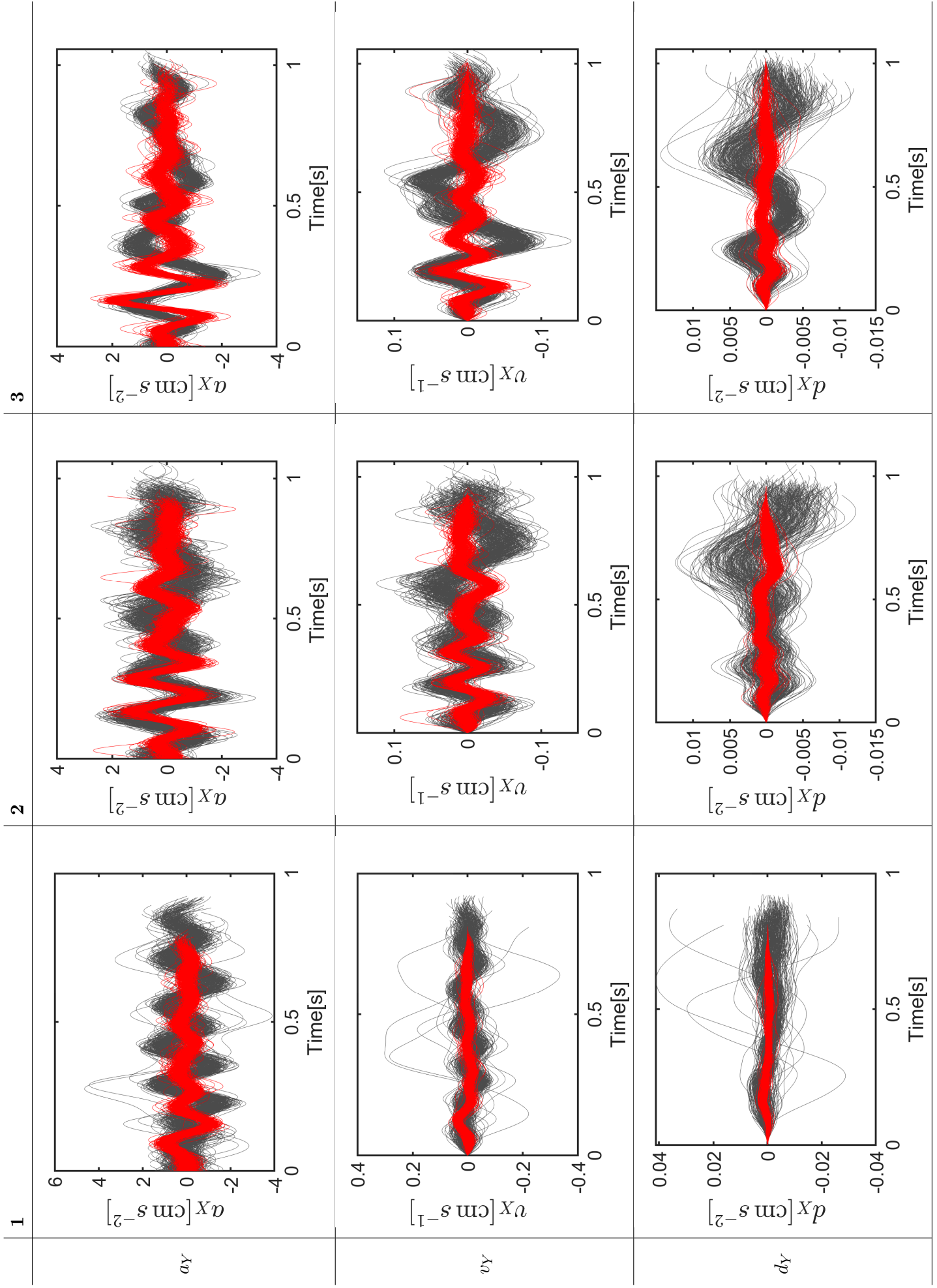


Table 3.3: Comparison between the reconstructed lateral acceleration a_X , velocity v_X and displacement d_X for three subjects.

Chapter 4

Non invasive estimate of the pulse pressure with the suspended bed and load cell signals

In the previous chapter, we reconstructed the CoM motion from the mBCG on both the suspended bed and the load cell system combining the physics of the instruments with modeling tools. In this chapter, we illustrate how the knowledge of the coupling among the physiology behind the BCG signal and the physics of the sensing devices may lead to novel clinical applications. In particular, we propose a cuff-less method for absolute pulse pressure assessment via the synergistic integration of two components, namely *(i)* theoretical simulations of cardiovascular physiology by means of our mathematical closed-loop model of the cardiovascular system, and *(ii)* synchronous ECG and BCG data acquired in our laboratory. To this end we leverage the basic BCG theory we revisited in the previous chapter and we use the suspended bed as sensing device, because it is a ultra-low frequency device that provides a waveform that is the closest to the physiological one. Thus, the main goal of this chapter is to develop and test a procedure that leverages physiology via a closed-loop model of the cardiovascular system to non-invasively estimate the absolute pulse wave pressure.

4.1 Background

High blood pressure was the leading risk factor for global disease burden in 2010 [28]. The potential negative outcomes resulting from an abnormal high blood pressure (BP) includes, just to name a few, the development of coronary artery disease [26], ischaemic stroke [28], aortic aneurism, left ventricular failure and myocardial infarction [34]. In addition, the association between elevated blood pressure and cardiovascular complications has been proved in several longitudinal and population-based study [35, 48]. For instance, Lee et al conducted a

ID	Gender	Age	Height [cm]	Weight [kg]	Systolic BP [mmHg]	Diastolic BP [mmHg]
1	Male	23	180	53.9	106.5	61.5
2	Male	22	192.5	82.3	117.5	68.8
3	Male	25	185	74.2	116.5	59
4	Male	32	180	72.3	109.7	52.3
5	Male	22	176	66.3	110.9	70
6	Male	69	180	79.4	112.1	65.2
7	Female	26	162.5	48	99.7	66.7
8	Female	28	165	49.9	106.7	70
9	Female	22	173	150	118.7	73.9
10	Female	66	152.4	71.1	116.5	59

Table 4.1: Details of subjects involved in the blood pressure study.

longitudinal study between 1962 and 1993 where 2280 patients were periodically monitored until death. The authors found that in younger adults the systolic blood pressure (SBP) was an independent predictor of fatal cardiovascular diseases, whereas the pulse pressure (PP), defined as the difference between the systolic and diastolic pressures, was a more accurate predictor of cardiovascular death in the elder population. In another study conducted with 110 normotensive patients with known coronary artery disease, the authors monitored the pulse pressure for 24 hours to evaluate the association between pulse pressure and other known cardiovascular markers to the severity of coronary artery disease. The study concluded that SBP, together with carotid artery intima–media thickness, were the marker which best associated with the severity of the coronary artery disease [51]. Benetos et al conducted a population-based study (Paris population, 834 subjects) to investigate the extent to which the carotid/brachial (C/B) ratio is an independent predictor of cardiovascular (CV) risk [5]. Brachial and carotid PP were measured from a cuff and pulse wave analysis respectively and multi-adjusted hazard ratios (HRs), which describes the relative risk of the complication based on comparison of event rates [43], were computed utilizing a regression method. The authors concluded that brachial and carotid PP, when used separately to evaluate adjusted CV risk, have a consistent impact.

Thus, given the role of the PP as an independent predictor of CV risk, an effective solution for monitoring blood pressure can play a crucial role in mitigating negative cardiovascular outcomes. In addition to traditional methods, such as arterial line blood pressure and blood pressure cuff, a range of solutions has been proposed to monitor BP. For instance, Shin et al developed a methodology which provides continuous BP estimates from the morphology of photoplethysmography (PPG) [41]. Another method is the pulse transit time (PTT), which computes the time delay between the observations of ECG and PPG valley or two PPG

devices from separate parts of the body to determine the relative blood pressure [46]. Ballistocardiography offers a promising venue to monitor BP due to its non-invasive and contactless nature. In a recent work, Su et al utilized a data-driven approach to establish features in the BCG waveform that could correlate with changes in blood pressure [46]. Notably, the authors were able to predict measurement of systolic blood pressure by utilizing the strength of the BCG waveform and the difference between IJ and JK amplitude at each heartbeat. The advantage of this study was the utilization of a hydraulic bed sensor system, that is a low-cost technology which does not require body contact. However, a calibration via a blood pressure cuff was needed, thereby limiting the possible utilization of this approach. Yet another approach to monitor the blood pressure utilizing the BCG was proposed by Shin et al by means of weight scale sensors [42]. Compared to the previous studies, which both utilized a data-driven approach, here we propose and test a procedure based on first principles that leverages physiology via a closed-loop model of the cardiovascular system to estimate PP. Indeed, the proposed mechanism-based approach offers the advantage of incorporating physiological knowledge into the model and enabling the investigation of mechanistic relationship between blood pressure and the pBCG waveforms.

4.2 Methods

The method section is organized as follow. In Sec. 4.2.1 we describe the data acquisition and signal processing procedure utilized in this study. Then, in Sec. 4.3.2 we provide the details regarding the proposed procedure to non-invasively estimate the absolute brachial pulse pressure from the BCG signal.

4.2.1 BCG Sensing Device, Data Acquisition and Signal Processing procedure

In this study we utilize the BCG signal acquired with the accelerometer on the suspended bed, which gives the BCG signal that is closest to the pBCG. For the present study, we consider the longitudinal (head-to-toe) direction since *(i)* it represents the direction where the predominant movement occurs and *(ii)* it can be supplied with physiological meaning thanks to the validated cardiovascular model.

For the data acquisition, ten healthy volunteers were recruited for a data collection in a controlled laboratory settings. Each person was asked to lay still on a suspended bed system previously described in [15], while the ECG, SCG and BCG signals were recorded simultaneously. ECG signals were acquired via a 3-lead configuration, SCG signals were measured using a Kionix KXR94-2283 accelerometer, with 1000 mV/g sensitivity [21] placed on the subject’s sternum, and BCG signals were acquired with a three-axis accelerometer from Kionix with 1000 mV/g sensitivity placed on the bed frame of the suspended bed.

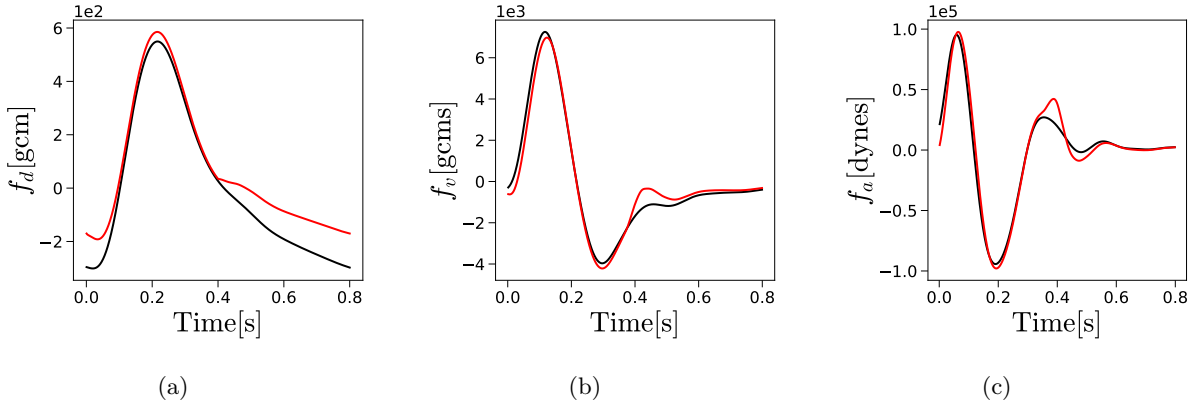


Figure 4.1: Simulated f_d , f_v and f_a via the closed-loop model: (a) black curve: f_d curves resulting considering all cardiovascular compartment, f_d curves resulting considering only the thoracic and abdominal compartment. (b) f_v curves resulting considering all cardiovascular compartment, f_v curves resulting considering only the thoracic and abdominal compartment. (c) f_a curves resulting considering all cardiovascular compartment, f_a curves resulting considering only the thoracic and abdominal compartment. representation..

All signals were collected simultaneously using an AD Instrument PowerLab 16/35 data acquisition system [22]. In addition to these signals, six blood pressure measurements were taken with the blood pressure cuff before starting the data collection and at the end of the same procedure to obtain the ground truth (GT) of the blood pressure. The age, sex and GT value for the BP are reported in Table 4.1.

To process the signal, we utilize the signal processing steps described in Section 3.2.2. As a result, we obtain three vector valued functions, denoted by $\mathcal{T}_{a,y}$, $\mathcal{T}_{v,y}$ and $\mathcal{T}_{d,y}$, which represent the ensemble of the segmented acceleration velocity and displacement. Then, each segmented curve $d_y(t) \in \mathcal{T}_{d,y}$ is converted into [dynes cm s⁻²] via the following relationship

$$f_d(t) = d_y(t) \cdot m_j \cdot g \quad \text{with } j = 1, \dots, 11 \quad (4.1)$$

where $d_y(t)$ is the BCG displacement measured in cm, g is the gravitational constant, equal to 981 cm s⁻², and m_j represent the mass of subject j measured in grams.

4.2.2 Non invasive estimate of the absolute pulse pressure

The closed loop model is utilized to obtain a physiologically-based relationship between the blood pressure and f_d . Firstly, we explore the relative contribution of each cardiovascular compartment in determining f_d . Indeed, although the volume waveforms $V_i(t)$ with $i = 1, \dots, N$ results from the complex interplay of each element in the closed loop model, a reasonable approximation of the pBCG waveforms can be obtained by considering a subset of all the cardiovascular compartments. Figure 4.1 compares the f_d , f_v and f_a waveforms

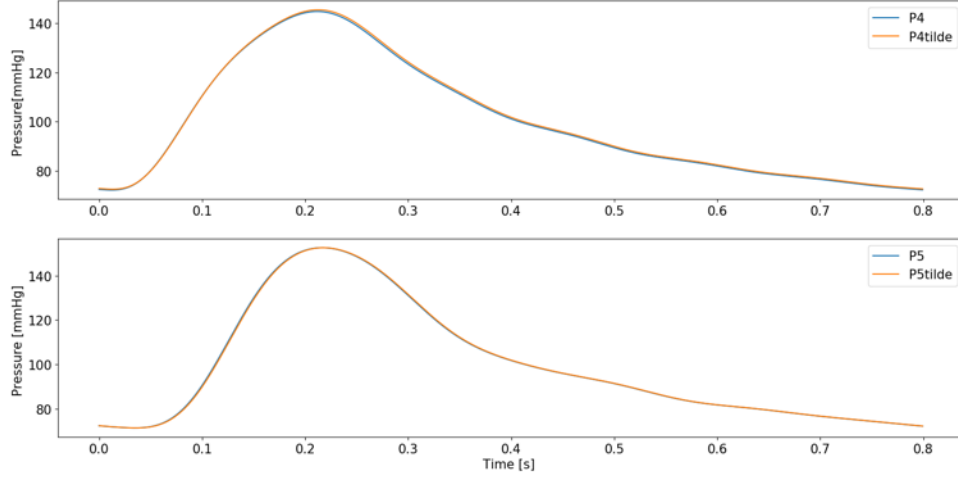


Figure 4.2: Comparison of the pressure waveform in the thoracic (top) and abdominal artery (bottom). Blue curve: $P_i = \frac{V_i}{C_i} + \gamma \frac{dV_i}{dt}$. Orange curve: $\tilde{P}_i = \frac{V_i}{C_i}$.

PARAMETER	VALUE	UNIT	REF
ρ_b	1.05	[g cm ⁻³ mmHg ⁻¹]	[15]
C_4	0.2196	[cm ³ mmHg ⁻¹]	[15]
C_5	0.1735	[cm ³ mmHg ⁻¹]	[15]
y_4	20	[cm]	[15]
y_5	35	[cm]	[15]

Table 4.2: Parameter of the proposed physiological-based formula.

as computed in [15], i.e. by considering $N=9$ cardiovascular compartments (black curves), and the corresponding waveforms obtained by only considering the volume waveforms in the thoracic and abdominal artery, i.e. $i = 4, 5$ in Eq 2.31 (red curve). Interestingly, a small difference, mainly in the diastolic part, can be observed between the two curves. Leveraging this result, we can approximate f_D with the following expression

$$f_D \approx \rho_b(V_4 + V_5) \quad (4.2)$$

To obtain the brachial pulse pressure from Eq. 4.2, we firstly utilize the relationship between the blood volume $V_i(t)$ and the blood pressure $P_i(t)$ in the thoracic and abdominal cardiovascular compartment [15], which can be written as

$$P_i = \frac{V_i}{C} + \gamma \frac{dV_i}{dt} \quad \text{with } i = 4, 5 \quad (4.3)$$

where P_i and V_i represent the pressure and the volume in the i compartment with $i = 4, 5$, whereas C and γ are positive constants representing the elastic and viscoelastic properties of the arterial wall. Although pressures and volumes waveform are coupled via Eq.4.3, i.e.

with a linear differential equation, we can reasonably assume that the viscoelastic component, which is given by $\gamma \frac{dV_i}{dt}$, induces a small change in the magnitude of the pressure waveforms. Indeed, Fig. 4.2 reports a comparison between the pressure waveforms in the thoracic and abdominal artery obtained when (i) $P_i = \frac{V_i}{C_i} + \gamma \frac{dV_i}{dt}$ (blue curve) and (ii) $\tilde{P}_i = \frac{V_i}{C_i}$ (orange curve). Model results confirm that the viscoelastic term does not significantly affect the magnitude of the pressure waveforms in the thoracic and abdominal compartments. Thus, leveraging these results, we can write an explicit relationship between f_D and the pressure in the abdominal and arterial compartments, namely

$$\frac{f_D}{\rho_b} = C_4 y_4 P_4(t) + C_5 y_5 P_5(t) \quad (4.4)$$

And by defining the average pressure in the abdominal compartment as $\overline{P_{abd}} = \frac{P_4(t) + P_5(t)}{2}$, the functional relationship between f_D and $\overline{P_{abd}}$ can be expressed as follow

$$\overline{P_{abd}} = \frac{f_D}{(C_4 y_4 + C_5 y_5 P_5(t)) \rho_b} \quad (4.5)$$

where $\overline{P_{abd}}$ represents an average value of the pressure in the abdominal aorta, C_4 and C_5 are the capacitances of the thoracic and abdominal artery and y_4 and y_5 are the locations at which the midpoint of the abdominal and thoracic arteries are assumed to be located with respect to the heart valves. The values for these parameter are reported in Table 4.2. To compute the brachial pressure, we then utilize the following formula

$$P_{bra} = \overline{P_{abd}} \cdot \beta \quad (4.6)$$

where β is defined as the ratio between the systolic pressure in the abdominal and brachial artery and it has been considered equal to 0.9 [49]. Finally, we can obtain an estimate of the pulse pressure as follow:

$$PP_{bra} = \max(P_{bra}) - \min(P_{bra}) = \max \left(\frac{f_D}{(C_4 y_4 + C_5 y_5 P_5(t)) \rho_b} \right) - \min \left(\frac{f_D}{(C_4 y_4 + C_5 y_5 P_5(t)) \rho_b} \right) \quad (4.7)$$

Overall, the following five steps are applied to recast an absolute cuffless measurement of pulse pressure from the BCG recordings on the suspended bed:

- measurement of the BCG signal on the suspended bed;
- perform the signal processing procedure outlined in Section 3.2.2;
- apply the physiological-based formula obtained via the closed-loop model to $f_d(t)$ to estimate the absolute brachial pulse pressure;
- compare the predicted absolute brachial pulse pressure with the measured brachial pressure.

DESCRIPTION	SYMBOLS	UNIT
<i>Longitudinal Acceleration</i>		
Magnitude of the J peak in a_y	A_J^a	[cm s ⁻²]
Magnitude of the K valley in a_y	A_K^a	[cm s ⁻²]
Timing of the J peak in a_y	T_J^a	[s]
Timing of the K valley in a_y	T_K^a	[s]
<i>Longitudinal Velocity</i>		
Magnitude of the first and most prominent peak in v_y	A_1^v	[cm s ⁻¹]
Timing of the first and most prominent peak in v_y	T_1^v	[s]
<i>Longitudinal Displacement</i>		
Magnitude of the first and most prominent peak in d_y	A_1^d	[cm]
Timing of the first and most prominent peak in d_y	T_1^d	[s]

Table 4.3: Summary of the analyzed BCG features for the subject involved in the study. The table distinguishes among features pertaining to the acceleration, velocity and displacement BCG.

4.3 Results

SUBJECT	A_J^a	A_K^a	A_1^v	A_1^d
<i>Male subject</i>				
1	1.86 ± 0.28	-2.16 ± 0.31	0.076 ± 0.02	3.7 · 10 ⁻³ ± 1 · 10 ⁻³
2	1.45 ± 0.36	-1.73 ± 0.46	0.062 ± 0.01	3 · 10 ⁻³ ± 1 · 10 ⁻³
3	1.43 ± 0.21	-1.40 ± 0.21	0.059 ± 0.01	2.9 · 10 ⁻³ ± 1 · 10 ⁻³
4	1.90 ± 0.30	-2.20 ± 0.43	0.073 ± 0.01	2.9 · 10 ⁻³ ± 1 · 10 ⁻³
5	1.03 ± 0.16	-1.05 ± 0.25	0.039 ± 0.01	1.8 · 10 ⁻³ ± 1 · 10 ⁻³
Mean Value Young Subject	1.53 ± 0.25	-1.70 ± 0.3	0.061 ± 0.01	2.86 · 10⁻³ ± 1 · 10⁻³
6	1.03 ± 0.17	-0.79 ± 0.25	0.024 ± 0.01	1 · 10 ⁻³ ± 1 · 10 ⁻³
<i>Female subject</i>				
8	0.79±0.25	-1.30±0.34	-0.032±0.02	2.8 · 10 ⁻³ ± 1 · 10 ⁻³
9	0.50±0.18	-0.72±0.30	0.039±0.02	1.1 · 10 ⁻³ ± 1 · 10 ⁻³
10	0.98±0.19	-1.14±0.22	0.04±0.01	1.7 · 10 ⁻³ ± 1 · 10 ⁻³
Mean Value Young Subject	0.75 ± 0.21	-1.05 ± 0.28	0.03 ± 0.01	1.9 · 10⁻³ ± 1 · 10⁻³
11	0.49±0.26	-0.82±0.31	0.02±0.01	1.5 · 10 ⁻³ ± 1 · 10 ⁻³

Table 4.4: mBCG relevant features among the subjects involved in the study

The result section is organized as follows. Firstly, in Sec. 4.3.1 we compare some of the pBCG features obtained for the subjects involved in the study, in particular focusing on the differences among the male and female subjects. For ease of reference, the list of the analyzed BCG features is reported in Table 4.4. Then, in Sec. 4.3.2 we apply the physiological-based formula obtained via the closed-loop model to estimate the absolute brachial pressure and

SUBJECT	T_J^a	T_K^a	T_1^v	T_1^d
<i>Male subject</i>				
1	0.11 ± 0.003	0.19 ± 0.008	0.15 ± 0.003	0.2 ± 0.02
2	0.13 ± 0.01	0.21 ± 0.01	0.17 ± 0.004	0.21 ± 0.02
3	0.13 ± 0.003	0.22 ± 0.004	0.17 ± 0.003	0.22 ± 0.04
4	0.12 ± 0.002	0.19 ± 0.002	0.16 ± 0.002	0.20 ± 0.06
5	0.12 ± 0.003	0.19 ± 0.009	0.15 ± 0.003	0.18 ± 0.06
Mean Value Young Subject	0.12 ± 0.005	0.20 ± 0.007	0.17 ± 0.03	0.20 ± 0.03
6	0.14 ± 0.08	0.20 ± 0.01	0.15 ± 0.002	0.18 ± 0.02
<i>Female subject</i>				
8	0.13±0.04	0.19±0.03	0.14±0.03	0.18 ± 0.06
9	0.19±0.01	0.15±0.08	0.13±0.07	0.21 ± 0.11
10	0.12±0.02	0.19±0.01	0.15±0.01	0.16 ± 0.10
Mean Value Young Subject	0.13 ± 0.02	0.17 ± 0.04	0.14 ± 0.035	0.17 ± 0.07
11	0.16±0.1	0.20±0.07	0.14±0.04	0.22 ± 0.12

Table 4.5: mBCG relevant features among the subjects involved in the study

test the performance on the whole population.

4.3.1 Intraclass variability of the relevant BCG features recorded on the suspended bed

Fig. 4.3 summarizes the mean value and the standard deviation of the measured features of a_y , whereas the quantitative values are reported in Table 4.4 and Table 4.5. Interestingly, we can notice that the male subjects exhibit a larger magnitude of the J peak (mean value of 1.53 [cm s⁻²]) which is almost twice larger than the one measured in the young female subject (0.75 [cm s⁻²]). In addition, subject 6 and 10, which are elder adults, are characterized by the smallest J-peak magnitude in both the male and female subgroups, respectively. A similar behaviour can be noticed for the K-valley amplitude, with an average larger amplitude recorded in the male subjects (-1.75 [cm s⁻²]) compared to females (-1.05 [cm s⁻²]). The same trend can be observed when considering the first more prominent peak of the velocity, with the mean value measured in young males which is twice than the one in the women, 0.061 [cm s⁻¹] and 0.03 [cm s⁻¹] respectively. The difference decreases when considering the displacement, where we can notice a small intra-sex difference and a significantly larger variability for both males and females. Interestingly, comparing the timing of the J peak (Fig. 4.3c) and the K valley (Fig. 4.3d) a less pronounced difference can be noticed among male and female subjects. Indeed, the mean value of T_J^a is around 0.13 s for all the young subjects, and also the mean value of T_K^a varies between a mean value of 0.20 s for young males and 0.18 s for young females. Interestingly, a significant higher variability in the timing

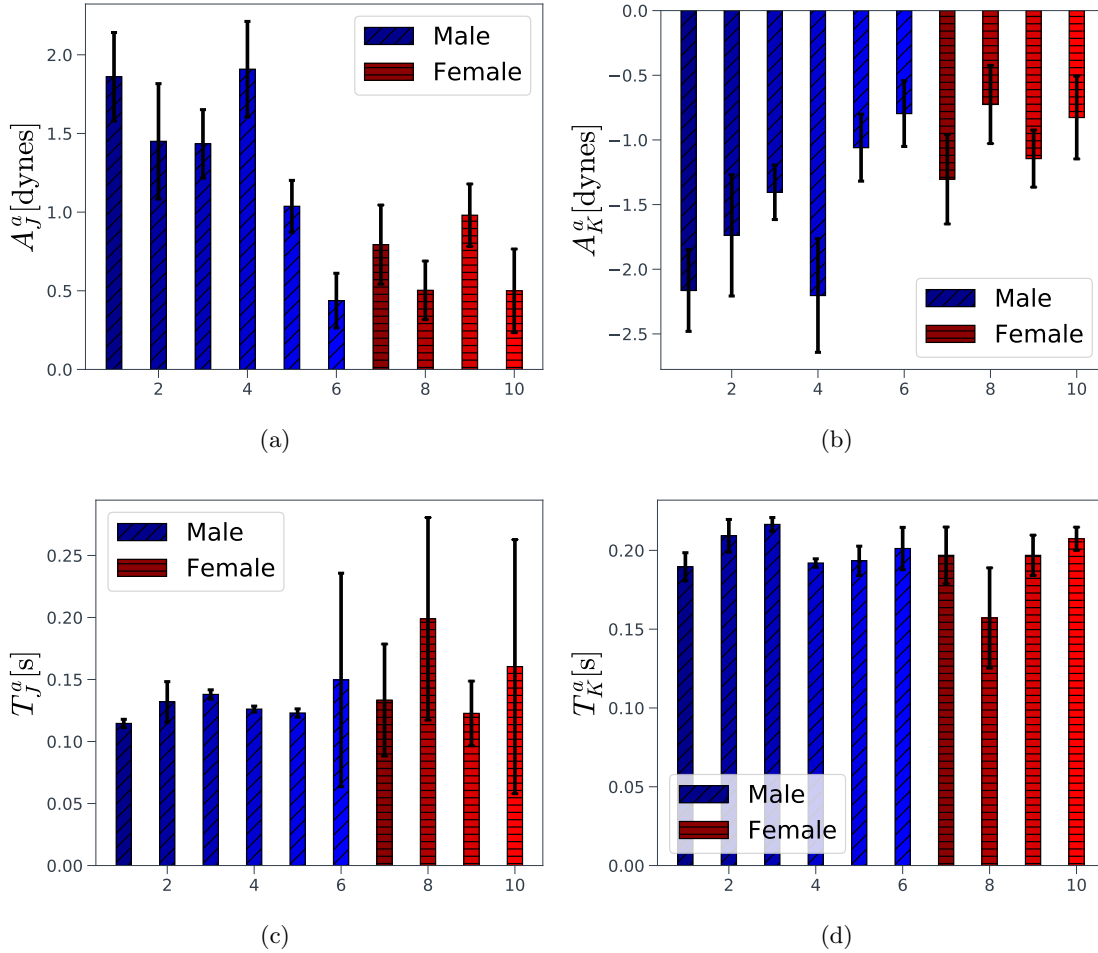


Figure 4.3: Bar chart summarizing the mean value and standard deviation of the recorded BCG features for the male subjects (blue bars) and the female subjects (red bars). (a) T_j^a , (b) T_K^a , (c) T_1^v , (d) T_1^d .

is observed for the two elder adults involved in the study, i.e. for subjects 6 and 10. Small differences are observed also when considering the timing of the most prominent peak of both velocity and displacement, with a smaller value of T_1^v and T_1^d in the female subjects. Overall, the timing of the peaks seems to be a more consistent feature among the two groups, whereas the amplitude presents a larger variability among male and females.

4.3.2 Absolute Pulse Pressure estimate procedure

As a first step, we have tested the proposed methodology on a young male (subject 4) and a young female (subject 7). Fig 4.4 (left) reports the ensemble of the measured d_y signal recorded for subject 4 (grey line), alongside with the computed template (red curve). To compute the absolute brachial pulse pressure, we selected a smaller ensemble comprising the d_y waveforms with a correlation below 0.4 and lag-time above 0.4 seconds, which is reported

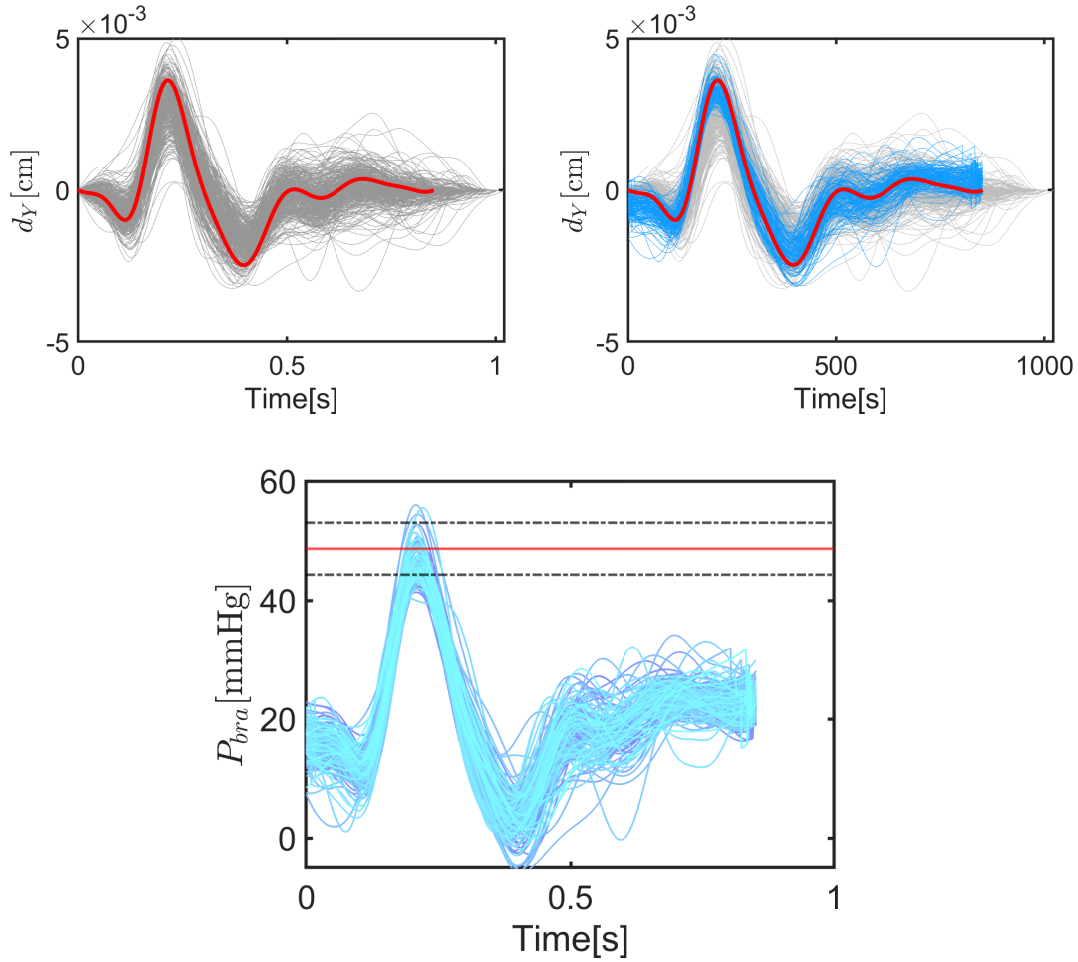


Figure 4.4: (a): recorded d_y (grey curves) and template curve (red curve) for subject 4.(b) d_y waveforms with a correlation below 0.4 and lag-time above 0.4 (blue shaded curve).(c): comparison between the predicted brachial pulse pressure amplitude via the proposed methodology (blue shaded curve) and the measured GT pressure (red line) for subject 4.

in Fig. 4.4 (right) in shaded blue. Fig. 4.4 (bottom) reports the predicted brachial pressure waveform for subject 4, which has been computed utilizing Eq. 4.6, alongside with the mean and standard deviation of the GT pressure measured in the lab (red and black lines, respectively). It should be noted that the P_{bra} waveform has been shifted, for graphical purposes only, so that its minimum is equal to 0. By so doing, we can observe a good agreement between the predicted absolute brachial pressure and the pressure measured via the cuff. Indeed, the model-based estimates of the pulse amplitude fall within the intervals of pressure measured in the lab. The same procedure has been applied in Fig. 4.5 for the female subject 7, and the results are reported in Fig. 4.5., where we can notice that the predicted brachial pressure is slightly smaller than the measured one.

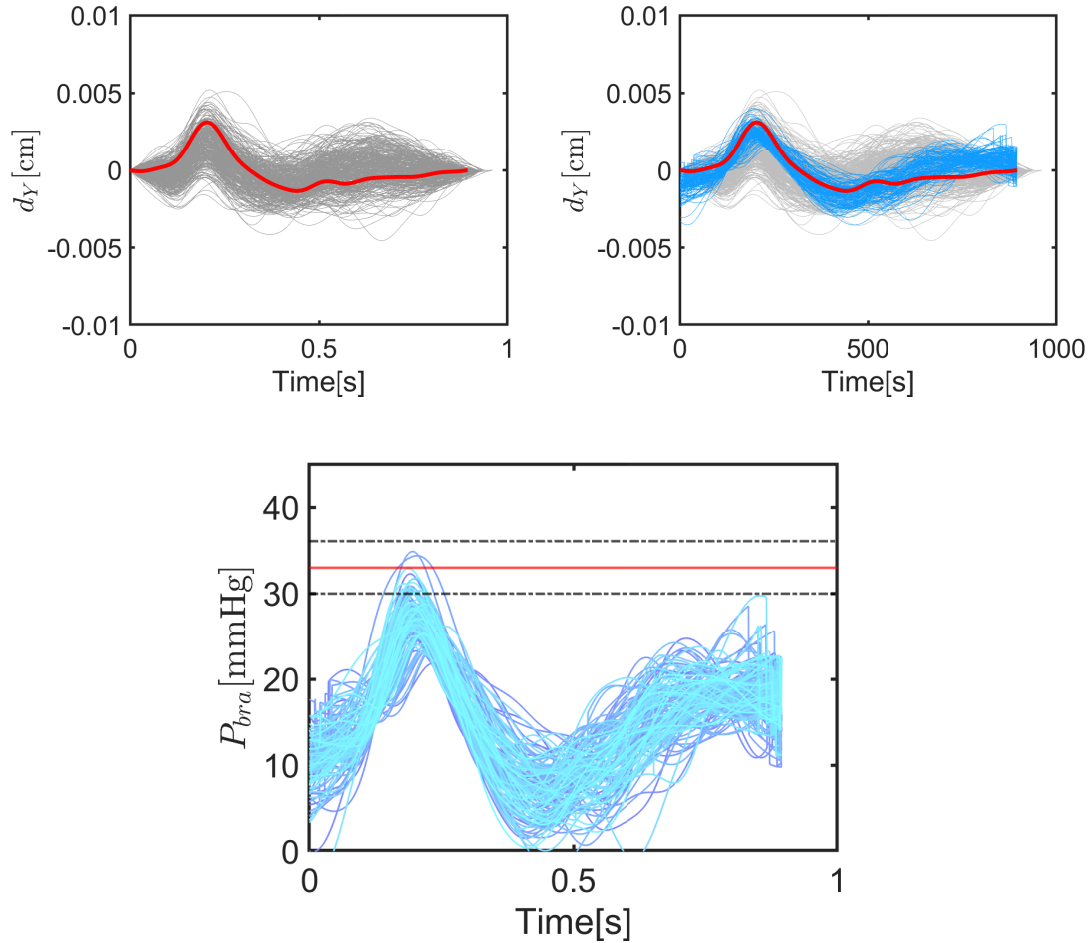


Figure 4.5: (a): recorded d_y (grey curves) and template curve (red curve) for subject 7.(b) d_y waveforms with a correlation below 0.4 and lag-time above 0.4 (blue shaded curve).(c): comparison between the predicted brachial pulse pressure amplitude via the proposed methodology (blue shaded curve) and the measured GT pressure (red line) for subject 7.

4.3.3 Absolute Pulse Pressure results for the entire population

The procedure described in Sec. 4.3.2 for subject 4 and 7 is then performed on each subject in the study. Fig. 4.6 compares the mean value of the brachial pulse pressure predicted via the closed-loop model for each male subjects (blue bar) and the measured GT pressure (black bar). In particular, the mean and standard deviation values have been computed utilizing the smaller ensemble of d_y waveforms with a correlation below 0.4 and lag-time above 0.4. Interestingly, a good agreement is sustained throughout all the male subjects involved in the study, thereby providing a quantitative demonstration of the predictive capability of the proposed method to estimate the absolute brachial pressure. In particular, an average error of 8.2 % is observed between the predicted and ground truth values, as reported in

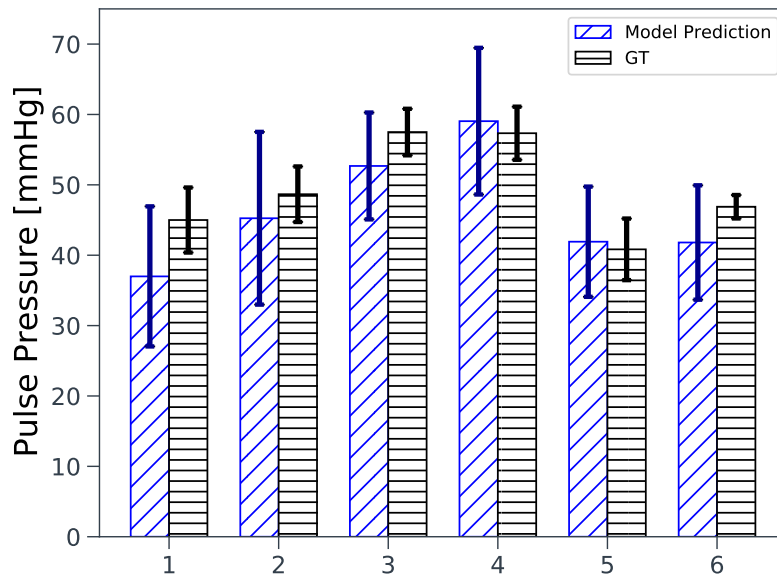
Table 4.6. When considering the mean value of the brachial pulse pressure predicted via the closed-loop model for the female subjects (red bar), our formula predicts a smaller pulse pressure amplitude compared to the ground truth. Indeed, for this subgroup, a larger 18% error is observed in Table 4.6.

4.4 Conclusions: advantages and limitation for the proposed method for the Pulse Pressure estimate

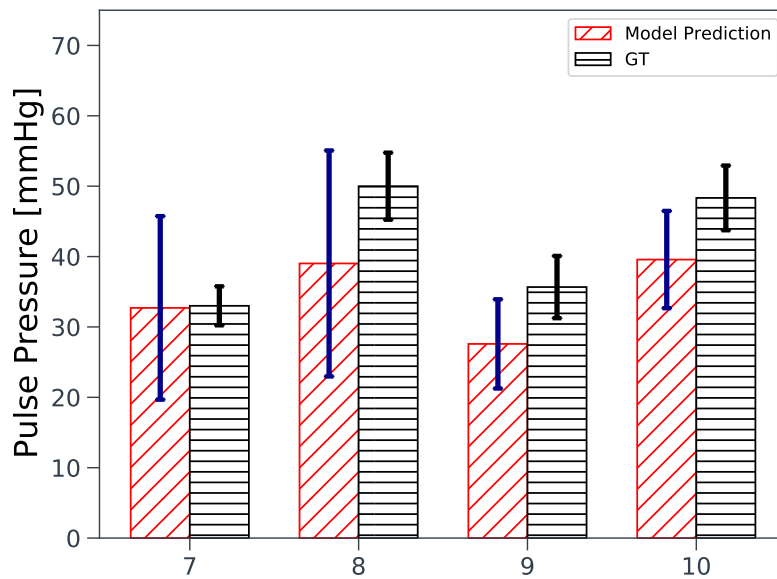
In this section, leveraging the BCG theoretical foundation defined in Chapter 2 and our closed-loop model of the cardiovascular system, we developed a novel non-invasive strategy to assess the absolute brachial pulse pressure from the measured BCG signal. The results show a remarkable agreement when considering male subjects, with a computed average error between the predicted and measured brachial PP equal to 8%. Overall, a larger error is observed when considering female subjects (18%). However, it should be noted that the parameters involved in Eq. 4.7 refers to an ideal average subject and that they could be individualized to account for the subject physiological differences. In this perspective, the next chapter presents an evolutionary algorithm aimed at individualizing the closed-loop model of the cardiovascular system.

ID	Mean GT PP	Mean Predicted PP	Percentage Error
1	45.0	37.1	17.2%
2	48.7	45.3	7.1%
3	57.5	52.7	8.3%
4	57.4	59.0	2.8%
5	40.8	41.9	2.7%
6	46.9	41.8	10.8%
7	33.0	32.7	0.6%
8	50	39.0	22%
9	35.6	27.6	22%
10	48.3	39.6	18%

Table 4.6: Comparison between the brachial pressure computed via the proposed cuff-less methodology and the GT brachial pressure measured in the lab.



(a)



(b)

Figure 4.6: (a) blue bar: mean value and standard deviation of predicted brachial pulse pressure for the male subject involved in the study, black bar: mean value and standard deviation of GT pressure measured via the cuff device in the lab. (b) red bar: mean value and standard deviation of predicted brachial pulse pressure for the female subject involved in the study, black bar: mean value and standard deviation of GT pressure measured via the cuff device in the lab.

Chapter 5

Development of an evolutionary algorithm to individualize the model parameters of the cardiovascular model

In Chapter 4, we proposed and tested a methodology to estimate the absolute PP leveraging physiology knowledge via a closed-loop model. In this chapter, we explore an additional strategy to estimate the individual PP. Specifically, we will individualize the parameters of the cardiovascular closed-loop model and, as a result, obtain an estimate of the central aortic pulse pressure (cPP). It is worth noting that central aortic blood pressure is often considered to be a superior predictor of cardiovascular risk compared to brachial blood pressure [32]. Several approaches estimate the cBP applying a signal processing technique or validated algorithm to the recorded radial or brachial pressure. For instance, the SphygmoCor device applies a generalized transfer function (GTF) to the measured brachial pulse pressure. Similarly, the Mobil-O-Graph device records the brachial pressure with a cuff, and then estimates the cBP via a GTF. Both the HEM 9000AIA and Novacor devices utilize a linear regression algorithm to the measured brachial blood pressure to recast the cBP. However, these approaches suffer from significant interdevice variability [32], and require a prior measurement of the blood pressure with a medical device, such as a pressure cuff. Conversely, the methodology we propose in this chapter relies on the combination of *(i)* a non-invasive, contact-less BCG measurement which are then combined with a ECG recording, *(ii)* a closed-loop mathematical model of the cardiovascular circulation and *(iii)* an evolutionary algorithm to individualize the model input parameters. Thus, this chapter has the following aims:

- to develop an evolutionary algorithm for the individualization of the cardiovascular

model;

- to evaluate the estimate of the central PP obtained via the EA algorithm;

The chapter is organized as follows. In Section 5.1, we present an overview of the evolutionary algorithms theory. Then, in Section 5.2 we outline the EA problem under investigation and provide the details regarding the implementation of the EA. Finally, in Sec. 5.3 we present the experimental results before providing the conclusive remarks in Sec. 5.4.

5.1 Evolutionary algorithms

Evolutionary algorithms (EA) represent a computational technique that use the mechanisms of evolution to search for optimal solutions to a problem. The EA search mechanism is inspired by Darwin's Theory of Evolution: similar to individuals evolving inside a species according to their fitness in the environment, solutions in a EA evolve in the search space in order to optimize an objective function[36].

Evolutionary computational models share a common conceptual base of simulating the evolution of an individual based on processes of selection and recombinations. More precisely, evolutionary algorithms begin with a population of individuals which receives a measure of its fitness in the environment. Then, selection process focuses on high fitness individuals, whereas recombination processes use random changes together with the fitness function to evaluate the goodness of each solution, thus resulting in a random exploration of the solution space and avoidance of local minima.

The outlined process can be formalized mathematically, following the procedure described in [3, 20]. Let us denote with \mathcal{G} the genotypic state space, which represents the underlying genetic coding of an individual (*genotype*) and by \mathcal{P} the phenotypical space, which represents the manner of response contained in the behavior, physiology, and morphology of the organism. Then, the evolution of a species can be described by mean of four mapping functions, namely

$$f_1 : \mathcal{I} \times \mathcal{G} \rightarrow \mathcal{P} \tag{5.1a}$$

$$f_2 : \mathcal{P} \rightarrow \mathcal{P} \tag{5.1b}$$

$$f_3 : \mathcal{P} \rightarrow \mathcal{G} \tag{5.1c}$$

$$f_4 : \mathcal{G} \rightarrow \mathcal{G}. \tag{5.1d}$$

where:

- the function f_1 is called epigenesis and maps an element $g_i \in \mathcal{G}$ in an indexed set $(i_1, \dots, i_i \dots i_k) \in \mathcal{I}$ into \mathcal{P} as a collection of phenotypes p_i ;

- the function f_2 is called selection and maps phenotypes p_1 into p_2 ;
- the function f_3 is called survival selection and maps the selected phenotypes p_2 into \mathcal{P} , thus describing the effects of the selection process in \mathcal{G} ;
- the function f_4 is called mutation and represents the genetic variation occurred to g_2 .

Algorithm 1 Evolutionary Algorithm

Input: $f_{a,n}^M$ with $n = 1 \dots N_c$

Output: ϕ_n with $n = 1, \dots, N_c$

```

1: for  $n \leftarrow 1$  to  $N_C$  do
2:   Set  $j = 1$ 
3:   Set Conv = False  $\Rightarrow j$  is the counter for the evolution of the n-th curve
4:   if  $n$  is 1 then
5:      $\mathbf{P}_{1,j} \leftarrow \text{Initialize population}(M)$ 
6:   else
7:      $\mathbf{P}_{n,j} \leftarrow \text{Initialize Constrained population}(\phi_1^{Ref})$ 
8:   end if
9:    $\mathbf{P}_{n,j}^{sort} \leftarrow \text{Evaluate fitness}(\mathbf{P}_{n,j})$ 
10:  while Conv is False do
11:     $\lambda_{n,j} \leftarrow \text{Selection}(\mathbf{P}_{n,j}^{sort}, \lambda)$   $\Rightarrow \text{card}(\lambda_{n,j}) = \lambda$ 
12:     $\mu_{n,j} \leftarrow \text{Mutation}(\lambda_{n,j})$   $\Rightarrow \text{card}(\mu_{n,j}) = \mu$ 
13:     $j + 1 \leftarrow j$ 
14:     $\mathbf{P}_{n,j}^{sort} \leftarrow \text{Evaluate Fitness}(\mathbf{P}_{n,j-1}^{sort} \cup \mu_{n,j-1})$ 
15:     $\mathbf{P}_{n,j}^{sort} \leftarrow \text{Selection}(\mathbf{P}_{n,j}^{sort}, M)$ 
16:    Conv  $\leftarrow \text{Check for Convergence}(\mathbf{P}_{n,j}^{sort})$ 
17:  end while
18:   $\phi_n^{Ref} \leftarrow \text{Select reference solution}(\mathbf{P}_{n,j})$ 
19: end for

```

5.2 Problem statement

Since the BCG signal originates from the motion of the blood in the human body, individual-specific features (e.g. height, weight, age and biomechanical cardiovascular features) yields individual-specific healthy pBCG signals. To reconstruct the combination of individual-specific cardiovascular features that lead to the individual pBCG, we will utilize the closed loop model to perform an evolutionary search, from which we aim at identifying the features that are most relevant for BCG personalization.

More precisely, let us denote by \mathcal{P} the set of all the model input parameter of the closed loop cardiovascular model. In the case of the EA, we consider a subset $\mathcal{P}^r \in \mathcal{P}$, for which

we aim at finding the individual-specific value resulting in the individual pBCG. Specifically, the set \mathcal{P}^r can be divided into 6 subsets, namely \mathcal{P}^{lv} , \mathcal{P}^{rv} , \mathcal{P}^a , \mathcal{P}^{ra} , \mathcal{P}^{la} , \mathcal{P}^{ya} in such a way that:

$$\begin{aligned}\mathcal{P}^r &= \mathcal{P}^{lv} \cup \mathcal{P}^{rv} \cup \mathcal{P}^a \cup \mathcal{P}^{ra} \cup \mathcal{P}^{la} \cup \mathcal{P}^{ya} = \\ &= \bigcup_{k \in \mathcal{K}} \mathcal{P}^k \text{ with } \mathcal{K} = \{lv, rv, a, ra, la, ya\}\end{aligned}\quad (5.2)$$

The set \mathcal{P}^{lv} contains the cardiovascular parameter representing the biomechanical properties of the left ventricle, the set \mathcal{P}^{rv} contains the cardiovascular parameter representing the biomechanical properties of the right ventricle, \mathcal{P}^a contains the cardiovascular parameter representing the biomechanical properties of the arterial system, \mathcal{P}^{ra} contains the radii of each arterial compartment modeled in the cardiovascular closed-loop, \mathcal{P}^{la} contains the lengths of each arterial compartment modeled in the cardiovascular closed-loop, whereas \mathcal{P}^{ya} contains the locations at which each arterial compartment is assumed to be located with respect to the heart valves plane. In the present work we have

$$\mathcal{P}^{lv} = \{\text{ELS, ULO, ELD, } q_L, \text{Ts}\}. \quad (5.3a)$$

$$\mathcal{P}^{rv} = \{\text{ERS, URO, ERD, } q_R, \text{Ts}\}. \quad (5.3b)$$

$$\mathcal{P}^a = \{\text{E, } R_7\}. \quad (5.3c)$$

$$\mathcal{P}^{ra} = \{r_i \text{ with } i = 2, 3, 4, 5, 6, 14\}. \quad (5.3d)$$

$$\mathcal{P}^{la} = \{l_i \text{ with } i = 2, 3, 4, 5, 6, 14\}. \quad (5.3e)$$

$$\mathcal{P}^{ya} = \{y_i \text{ with } i = 2, 3, 4, 5, 6, 14\}. \quad (5.3f)$$

$$(5.3g)$$

We set $N_{lv} = \text{card}(\mathcal{P}^{lv})$, $N_{rv} = \text{card}(\mathcal{P}^{rv})$, $N_a = \text{card}(\mathcal{P}^a)$, $N_{ra} = \text{card}(\mathcal{P}^{ra})$, $N_{la} = \text{card}(\mathcal{P}^{la})$, and $N_{ya} = \text{card}(\mathcal{P}^{ya})$. Thus, referring to Eq. 5.1, we can introduce the following notation which that will be utilized thorough this chapter:

- the genetic coding of an individual, i.e. the **genotype**, is represented by the model parameters $p_i^k \in \mathcal{P}^k$ for $k \in \mathcal{K}$ and $i = 1, \dots, N_k$.
- The complete **genotypical expression of an individual**, abbreviated as **individual**, will be then denoted as $\mathcal{P}^r = \bigcup_{k \in \mathcal{K}} \mathcal{P}^k$;
- the collection of **individuals** produced in a generation j in the evolutionary search will be denoted as \mathbf{P}_j
- the epigenesis function f_1 is the closed-loop model of the cardiovascular system presented in Chapter 2, namely

$$\begin{aligned}f_1 : \mathcal{I} \times \mathcal{G} &\rightarrow \mathcal{P} \\ \mathbf{P}_j &\rightarrow \mathbf{f}_a^{\mathcal{P}}\end{aligned}\quad (5.4)$$

where \mathbf{P}_j represents the *individuals* in a generation j and $\mathbf{f}_a^{\mathcal{P}}$ represent the closed-loop model predicted f_a waveform utilizing \mathbf{P}_j as an input.

The objective of the present work is to find the numerical value of each parameter $p_i^k \in \mathcal{P}^k$ for $k \in \mathcal{K}$ and $i = 1, \dots, N_k$ such that:

$$\arg \min_{p_i^k \in \mathcal{P}^k} f_a^{\mathcal{P}} = \{p_i^k \mid d(f_a^{\mathcal{P}}, f_a^{\mathcal{M}})\} \quad (5.5)$$

where $f_a^{\mathcal{M}}$ is the f_a curve experimentally measured on the suspended bed for each individual, whereas $f_a^{\mathcal{P}}$ is the f_a curve predicted via the closed-loop model.

5.2.1 Data Collection

BCG signals were acquired on a healthy subject (male of 25 years of age) recruited for a data collection in a controlled laboratory settings. The subject was asked to lay still on a suspended bed system previously described in [15], while the ECG, SCG and BCG signals were recorded simultaneously. ECG signals were acquired via a 3-lead configuration, SCG signals were measured using a Kionix KXR94-2283 accelerometer, with 1000 mV/g sensitivity [21] placed on the subject's sternum, and BCG signals were acquired with a three-axis accelerometer from Kionix with 1000 mV/g sensitivity placed on the bed frame of the suspended bed. All signals were collected simultaneously using an AD Instrument PowerLab 16/35 data acquisition system [22]. In addition to these signal, six blood pressure measurements were taken with the blood pressure cuff before starting the data collection and at the end of the same procedure to obtain the ground truth (GT) of the blood pressure.

5.2.2 Evolutionary algorithm formulation

The strategy adopted in the EA implementation is summarized in Algorithm 1. For each subject in the study, N_c consecutive $f_a^{\mathcal{M}}$ curves are selected and utilized as objective curves for the evolutionary search. For the first objective curve, i.e. $n = 1$, an initial population $\mathbf{P}_{1,j}$ of M random individuals \mathcal{P}^r is computed via Algorithm 2. At each iteration of the loop (line 1), the `InitialMutation` function computes the underlying genotype p_i^k , for $k \in \mathcal{K}$ and $i = 1, \dots, N_k$ of each individual $\mathcal{P}^r \in \mathbf{P}_{1,i}^j$ according to the following scheme:

Algorithm 2 Initialize Population

Input: M $\triangleright M$ is the size of the initial population**Output:** $\mathbf{P}_{1,i}^j = \{\mathcal{P}_1^r, \dots, \mathcal{P}_M^r\}$

```
1: for  $m \leftarrow 1$  to  $M$  do
2:    $Check \leftarrow \text{False}$ 
3:   while  $Check$  is  $\text{False}$  do
4:      $\mathcal{P}_m^r \leftarrow \text{InitialMutation}$ 
5:      $\text{PhysiologicalCheck}(\mathcal{P}_m^r)$ 
6:     if  $\text{PhysiologicalCheck}(\mathcal{P}_m^r)$  is  $\text{Pass}$  then
7:        $Check \leftarrow \text{True}$ 
8:     end if
9:   end while
10: end for
```

Algorithm 3 Evaluate Fitness

Input: $\mathbf{P}_{1,i}^j = \{\mathcal{P}_1^r, \dots, \mathcal{P}_M^r\}$ **Output:** $\mathbf{P}_{n,i}^{j,sort}$

```
1: for  $m \leftarrow 1$  to  $M$  do
2:   Compute  $f_{a,m}^{\mathcal{P}}$  from  $\mathcal{P}_M^r$ 
3:   Compute  $d_m = \sqrt{(f_{a,m}^{\mathcal{P}} - f_{a,m}^{\mathcal{M}})^2}$ 
4: end for
5:  $\mathbf{P}_{n,i}^{j,sort} \leftarrow \text{sort } \mathbf{P}_{1,i}^j$  based on  $\mathbf{d} = \{d_1, \dots, d_M\}$ 
```

$$p_i^{lv} = \bar{p}_i^{lv} + \mathcal{N}(0, \sigma_i^{lv}) \quad i = 1, \dots, N_{lv} \quad (5.6a)$$

$$p_i^{rv} = \bar{p}_i^{rv} + \mathcal{N}(0, \sigma_i^{rv}) \quad i = 1, \dots, N_{rv} \quad (5.6b)$$

$$p_i^a = \bar{p}_i^a + \mathcal{N}(0, \sigma_i^a) \quad i = 1, \dots, N_a \quad (5.6c)$$

$$p_i^{ra} = \mathcal{U}(p_{i,inf}^{ra}, \min(p_{i,sup}^{ra}, p_{i-1}^{ra})) \quad i = 1, \dots, N_{ra} \quad (5.6d)$$

$$p_i^{la} = \mathcal{U}(p_{i,inf}^{la}, p_{i,sup}^{la}) \quad i = 1, \dots, N_{la} \quad (5.6e)$$

$$p_i^{ya} = \bar{p}^{ya} \cdot \alpha^{ya} \quad i = 1, \dots, N_{ya} \quad (5.6f)$$

where \bar{p}_i^k and σ_i^k for $k \in \{lv, rv, a\}$ and $i = 1, \dots, N_k$ are the baseline values and standard deviation for each bio-mechanical parameter in the subset $\mathcal{P}^{lv} \cup \mathcal{P}^{rv} \cup \mathcal{P}^a$ (see Table 5.2), $p_{i,inf}^{ra}$ and $p_{i,sup}^{ra}$ represent the physiological lower and upper bound for the radius of each cardiovascular compartment (Table 5.3), $p_{i,inf}^{la}$ and $p_{i,sup}^{la}$ represent the physiological lower and upper bound for the length of each cardiovascular compartment (Table 5.3) whereas α^{ya} is a multiplicative factor established a priori based on the subjects' height. It is worth noting that, when computing the radii and lengths of each arterial segments, three constraints

have been imposed: (i) the radius should decrease when moving down into the arterial tree (Eq.5.6d), (ii) the radius of each arterial compartment should be within the range from $p_{i,inf}^{ra}$ and $p_{i,sup}^{ra}$ (Eq.5.6d) and (iii) the length of each arterial compartment should be within the range from $p_{i,inf}^{la}$ and $p_{i,sup}^{la}$ (Eq.5.10).

Then, the `PhysiologicalCheck` function verifies whether the individual \mathcal{P}_m^r results in a normal clinical range for some of the quantitative parameters describing cardiovascular physiology (line 5), including end-diastolic volume (EDV), end-systolic volume (ESV), stroke volume (SV), cardiac output (CO) and ejection fraction (EF) associated with the left and right ventricles. EDV and ESV are computed as the maximum and minimum values of the ventricular volumes during the cardiac cycle, respectively, and their difference gives SV, namely $SV = EDV - ESV$. The relative difference between EDV and ESV gives EF, namely $EF = 100 \times (EDV - ESV) / EDV$. Then, denoting by Tc the length of the heartbeat measured in seconds, the heart rate HR and the cardiac output CO are computed as $HR = 60 / Tc$ and $CO = HR \times SV / 1000$. Table 5.1 provides the values of these parameters for the left and right ventricles as reported in the clinical literature.

Once the initial population $\mathbf{P}_{1,j}$ is produced (line 8, Algorithm 1), each random individual $\mathcal{P}^r \in \mathbf{P}_{1,i}$ is ordered according to its similarity to the objective curve $f_{a,n}^{\mathcal{M}}$ utilizing Algorithm 3. Firstly, the algorithm computes $f_{a,m}^{\mathcal{M}}$, which represent the f_a curve predicted by the model having \mathcal{P}_m^r as an input (line 2). Then, the fitness of each combination \mathcal{P}_m^r is evaluated computing the Euclidean distance between $f_{a,m}^{\mathcal{P}}$ and $f_a^{\mathcal{M}}$ (line 3) and utilized as the criteria to sort $\mathbf{P}_{1,i}$.

At this point, the actual evolutionary search starts for the n -th curve (line 10-14, Algorithm 1). Firstly, the λ fittest individuals of the generation j are selected and collected into the vector $\boldsymbol{\lambda}_{n,j}$. Then, for each individual $\mathcal{P}^r \in \boldsymbol{\lambda}_{n,j}$, μ physiological offsprings are produced utilizing the algorithm reported in Algorithm 6. Denoting with $p_{i,\ell}^k$ the genotype of the parent \mathcal{P}_ℓ^r for $k \in \mathcal{K}$ and $i = 1 \dots N_k$, the genotype $p_{i,c}^k$ of the offspring $\mathcal{P}_{\ell,c}^r$ is computed via the `Mutation` function according to the following rule (line 5):

$$p_{i,c}^{lv} = p_{i,l}^{lv} + \mathcal{N}(0, \sigma_i^{lv}) \quad i = 1, \dots, N_{b,lv} \quad (5.7a)$$

$$p_{i,c}^{rv} = p_{i,l}^{rv} + \mathcal{N}(0, \sigma_i^{rv}) \quad i = 1, \dots, N_{rv} \quad (5.7b)$$

$$p_{i,c}^a = p_{i,l}^a + \mathcal{N}(0, \sigma_i^a) \quad i = 1, \dots, N_{b,ra} \quad (5.7c)$$

$$p_{i,c}^{ra} = p_{i,l}^{ra} + \mathcal{U}(p_{i,inf}^{ra} - p_{i,c}^{ra}, \min(p_{i,inf}^{ra}, p_{i-1}^{ra}) - p_{i,c}^{ra}) \quad i = 1, \dots, N_{ra} \quad (5.7d)$$

$$p_{i,c}^{la} = p_{i,l}^{la} + \mathcal{U}(p_{i,inf}^{la} - p_{i,c}^{la}, p_{i,sup}^{la} - p_{i,c}^{la}) \quad i = 1, \dots, N_{ra} \quad (5.7e)$$

$$p_{i,c}^{ya} = \bar{p}^{ya} \cdot \alpha^{ya} \quad i = 1, \dots, N_{ya} \quad (5.7f)$$

where $p_{i,l}^k$ for $k \in \mathcal{K}$ and $i = 1, \dots, N_k$ are the model parameters resulting in the parent genotype $\mathcal{P}_{\ell,c}^r$, whereas σ_i^{lv} , σ_i^{rv} and σ_i^a represent the standard deviation for each bio-

Algorithm 4 Mutation

Input: $\lambda_{n,j} = \{\mathcal{P}_1^r, \dots, \mathcal{P}_\ell^{r,k}, \dots, \mathcal{P}_\lambda^r\}$ $\triangleright \lambda = \text{card}(\lambda_{n,j})$
Output: $\mu_{n,j} = \{\{\mathcal{P}_{1,1}^r \dots \mathcal{P}_{1,\mu}^r\} \dots \cup \{\mathcal{P}_{\ell,1}^r \dots \mathcal{P}_{\ell,\mu}^r\} \dots \cup \{\mathcal{P}_{\lambda,1}^r \dots \mathcal{P}_{\lambda,\mu}^r\}\}$ $\triangleright \text{card}(\mu_{n,j}) = \lambda \cdot \mu$

- 1: **for** $\ell \leftarrow 1$ to λ **do**
- 2: **for** $c \leftarrow 1$ to μ **do**
- 3: $Check \leftarrow \text{False}$
- 4: **while** $Check$ is **False** **do**
- 5: $\mathcal{P}_{\ell,c}^r \leftarrow \mathcal{P}_\ell^r + \text{Mutation}(\mathcal{P}_\ell^r)$
- 6: $\text{PhysiologicalCheck}(\mathcal{P}_{\ell,c}^r)$
- 7: **if** $\text{PhysiologicalCheck}(\mathcal{P}_{\ell,c}^r)$ pass **then**
- 8: $Check \leftarrow \text{True}$
- 9: **end if**
- 10: **if** counter \leq maxiter **then**
- 11: $\mathcal{P}_{\ell,c}^r \leftarrow \text{InitializePopulation}$
- 12: $Check \leftarrow \text{True}$
- 13: **end if**
- 14: **end while**
- 15: **end for**
- 16: **end for**

Algorithm 5 Check for Convergence

Input: $\mathbf{P}_{n,j}^{\text{sort}}, N_{\text{Curve}}$
Output: **True** or **False**

- 1: Compute $A_J^{\mathcal{M}}, A_K^{\mathcal{M}}, T_J^{\mathcal{M}}, \Delta T_{jk}^{\mathcal{M}}$
- 2: **for** $n_c \leftarrow 1$ to N_{Curve} **do**
- 3: **if** $A_J^{\mathcal{M}} - A_{nc,J}^{\mathcal{P}} \leq 5\%$ **and** $A_K^{\mathcal{M}} - A_{nc,K}^{\mathcal{P}} \leq 5\%$ **and** $T_J^{\mathcal{M}} - T_{nc,J}^{\mathcal{P}} \leq 5\%$ **and** $\Delta T_{jk}^{\mathcal{M}} - \Delta T_{jk,nc}^{\mathcal{P}} \leq 5\%$ **then**
- 4: $True \leftarrow \text{Converged}$
- 5: **break**
- 6: **end if**
- 7: **end for**

mechanical parameter in \mathcal{P}^{lv} , \mathcal{P}^{rv} and \mathcal{P}^a . Also in this case, the radii and lengths of each arterial segments must be within the physiological bound reported in the literature (see Table 5.3). Regarding y_i^k , α^{ya} is a multiplicative factor which is drawn from $\mathcal{U}(1, 1 + \mu)$, with μ being a factor established a priori based on the subjects' height.

The procedure continues until μ child are found for each parent $\mathcal{P}^r \in \lambda_{n,i}^j$ and the output is grouped into a vector $\mu_{n,i}^j$. Then, all the individuals of generation j are ordered according to its similarity to the objective curve $f_a^{\mathcal{M}}$ utilizing Algorithm 3 and the fittest M

individuals are kept and form the generation advancing in the evolution, denoted as $\mathbf{P}_{n,j}^{sort}$. Each generation $\mathbf{P}_{n,j}^{sort}$ is then checked to verify whether the convergence criteria reported in Alg.5 is satisfied. Firstly, the algorithm computes the magnitude and timing of the J peak of the objective curve, the magnitude of the K valley and the time difference between the timing of the J peak and K valley, denoted as A_K^M , A_J^M and T_J^M and T_K^M respectively. Then, the EA verifies whether there exist an individual satisfying the following two constraints (line 2-3): (i) the individual must be within the first N_{curves} individual of $\mathbf{P}_{n,j}^{sort}$ and (ii) the predicted J-K complex features must be within a 5% range when compared to the objective curve. If such an individual exists, convergence is reached. The rationale behind the considered convergence criteria is the following:

- the J peak and K valley are the most prominent peak in the a_y waveforms and they are closely related to the systolic and diastolic central pressure. Thus we aim at finding a curve that has the same magnitude and timing for these two parameters;
- by imposing the further constraint that the curve must be within the first n_c curved ranked by the EA algorithm, we aim at finding a solution that is close in an average sense to the measured curve and, simultaneously, maximizes the similarity to the J-K complex features;

Once the first solution $p_i^k \in \mathcal{P}^k$ is found, we constraint some of the parameters for the subsequent runs of the EA. Indeed, the cardiovascular structural parameters, namely $\mathcal{P}^{s,ra}$, $\mathcal{P}^{s,la}$ and $\mathcal{P}^{s,ya}$ are not expected to change from heart beat to heart beat. By denoting with the subscript *ref* the parameter values $\mathcal{P}^{s,i}$, with $i = ra, ya, la$ obtained in the first iteration, their value in the subsequent iteration will belong to the following intervals:

$$[p_{ref}^{s,ra} - 3\%, p_{ref}^{s,ra} + 3\%] \quad i = 1, \dots, N_{s,ra} \quad (5.8)$$

$$[p_{ref}^{s,ya} - 3\%, p_{ref}^{s,ya} + 3\%] \quad i = 1, \dots, N_{s,ya} \quad (5.9)$$

$$[p_{ref}^{s,la} - 3\%, p_{ref}^{s,la} + 3\%] \quad i = 1, \dots, N_{s,la} \quad (5.10)$$

$$(5.11)$$

Then the algorithm proceed as for the first run, i.e. according to Alg. 1.

5.3 Results

In this section, we test the proposed EA methodology on one subject.

5.3.1 EA algorithm results

Fig. 5.1 reports the collection of segmented $f_{a,j}^M$ curve alongside with the objective curve, which have been randomly selected as a sample of 5 consecutive curves out of the whole

PARAMETER	UNIT	NORMAL CLINICAL RANGE	
		<i>Left</i> <i>Ventricle</i>	<i>Right</i> <i>Ventricle</i>
End-Diastolic Volume (EDV)	[ml]	142 (102,183) [30]	144 (98,190) [29] 100 - 160 [27]
End-Systolic Volume (ESV)	[ml]	47 (27,68) [30]	50 (22,78) [29] 50-100 [27]
Stroke Volume (SV)	[ml/beat]	95 (67, 123) [30]	94 (64, 124) [29] 60-100 [27]
Cardiac Output (CO)	[l/min]	4-8 [27]	4-8 [27]
Ejection Fraction (EF)	[%]	67 (58, 76) [30]	66 (54, 78) [29] 40 - 60 [27]

Table 5.1: Cardiovascular Physiology: Condition establishing if a combination $\mathcal{P}_{r,i}$ is physiological.

PARAMETER	UNIT	BASELINE VALUE	REF	STANDARD DEVIATION	REF
ELS	[mmHg cm ⁻³ s ⁻¹]	1.375	[15]	0.6875	This work
ELD	[mmHg cm ⁻³ s ⁻¹]	0.04	[15]	0.02	This work
ULO	[mmHg]	50	[15]	25	This work
ERS	[mmHg cm ⁻³ s ⁻¹]	0.23	[15]	0.115	This work
ERD	[mmHg cm ⁻³ s ⁻¹]	0.01	[15]	0.005	This work
URO	[mmHg]	26	[15]	13	This work
E	[mmHg]	3000	[15]	1500	This work

Table 5.2: Summary of the baseline and the standard deviation values utilized in the EA simulation for each of the bio-mechanical parameter for the left and right ventricle and the arterial segments.

ensemble. To run the EA, we considered an initial population consisting of 300 individuals, and we set $\mu = 80$ and $\lambda = 30$. For each $f_{a,j}^M$ curve, the EA runs until the convergence criteria is satisfied and then the three best ranked curve are furtherly analyzed. Specifically, by denoting with $\mathbf{P}_n^{j,sort}$ the population produced at the j generation where the convergence criteria is satisfied for the n objective curve, the three best curves are denoted as $\mathbf{P}_n^{j,best} = \{\mathcal{P}_1^r, \mathcal{P}_2^r, \mathcal{P}_3^r\} \in \mathbf{P}_n^{j,sort} = \{\mathcal{P}_1^r, \dots, \mathcal{P}_M^r\}$.

The output of the EA algorithm is the *personalized* range of variability of each physiological parameters in \mathcal{P}^r , which for subject 4 have been reported in Fig. 5.2. The bars

ARTERIAL SEG.	UNIT	$p_{i,inf}^{ra}$	$p_{i,sup}^{ra}$	REF	$p_{i,sup}^{la}$	$p_{i,sup}^{la}$	REF
Ascending ($i = 2$)	[cm]	1.49	1.91	[50]	4	5	[13], [15]
Aortic arc ($i = 3$)	[cm]	1.14	1.42	[50]	3.85	5.9	[7], [15]
Thoracic ($i = 4$)	[cm]	0.92	1.28	[18]	12.9	15.7	[15],[37]
Abdominal ($i = 5$)	[cm]	0.80	1.10	[18]	13	16	[15], [13], [11]
Iliac ($i = 6$)	[cm]	0.492	0.725	[18]	3.7	7.5	[6]
Carotid ($i = 14$)	[cm]	0.26	0.36	[24]	20	24.4	[10]

Table 5.3: Summary of the reported range of the length and radii of the arterial compartment.

Algorithm 6 Mutation

Input: $\lambda_{n,i}^j = \{\mathcal{P}_1^r, \dots, \mathcal{P}_\ell^{r,k}, \dots, \mathcal{P}_\lambda^r\}$ $\triangleright \mu = \text{card}(\lambda_{n,i}^j)$
Output: $\mu_{n,i}^j = \{\{\mathcal{P}_{1,1}^r \dots \mathcal{P}_{1,C}^r\} \dots \cup \{\mathcal{P}_{\ell,1}^r \dots \mathcal{P}_{\ell,C}^r\} \dots \cup \{\mathcal{P}_{\lambda,1}^r \dots \mathcal{P}_{\lambda,C}^r\}\}$ $\triangleright C = \frac{\lambda}{\mu}$

- 1: **for** $\ell \leftarrow 1$ to λ **do**
- 2: **for** $c \leftarrow 1$ to C **do**
- 3: $Check \leftarrow \text{False}$
- 4: **while** $Check$ is **False** **do**
- 5: $\mathcal{P}_{\ell,c}^r \leftarrow \mathcal{P}_\ell^r + \text{Mutation}(\mathcal{P}_\ell^r)$
- 6: $\text{PhysiologicalCheck}(\mathcal{P}_{\ell,c}^r)$
- 7: **if** $\text{PhysiologicalCheck}((\mathcal{P}_{\ell,c}^r))$ pass **then**
- 8: $Check \leftarrow \text{True}$
- 9: **end if**
- 10: **if** counter \leq maxiter **then**
- 11: $\mathcal{P}_{\ell,c}^r \leftarrow \text{InitializePopulation}$
- 12: $Check \leftarrow \text{True}$
- 13: **end if**
- 14: **end while**
- 15: **end for**
- 16: **end for**

represent the mean value of each physiological parameter in $\mathbf{P}_n^{j,best}$ with $n = 1, \dots, 5$ and the associated standard deviation. The results indicate that the variation among the five successive curves is within a 20 % variation, except for two of the parameters of the right ventricle, i.e. A_{qr} and ERD, and the effective peripheral resistance R_7 . In addition, as a result of the imposed constraint on the radii, length and y during the EA algorithm construction, the values predicted by the EA in the subsequent runs are within an even smaller 6 % range.

Fig. 5.3 reports the comparison between the experimentally measured $f_{a,n}^{\mathcal{M}}$ curve (black curve), with $i = 1, \dots, N_c$ and the best three ranked curve $f_{a,n}^{\mathcal{P}}$ (shaded colored-curve) predicted by the closed-loop model utilizing $\mathbf{P}_n^{j,best}$ as a personalized input. Notably, the f_a

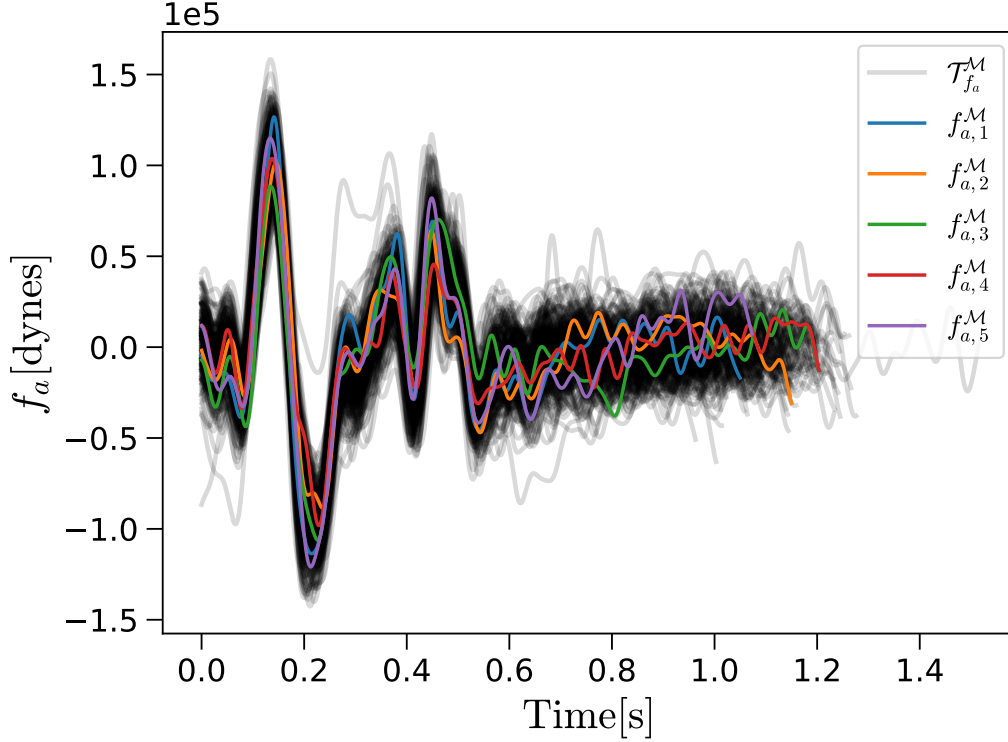


Figure 5.1: $\mathcal{T}_{f_a}^M$: collection of the individually segmented $f_{a,j}^M(t)$ curves for subject 4 (black curves). $f_{a,j}^M$: selected objective curves for subject 4.

curves predicted by the EA model shows a good agreement with the experimentally measured f_a^M in the initial part of the heart beat, with a detectable accordance in term of J-K features. Considering the following M-N complex, the f_a curve produced by the EA qualitative follows the shape of the subsequent peaks and valleys, whereas in the diastolic part of the heart beat the EA predicts a flatter profile if compared to the experimentally measured shape. The quantitative comparison is reported in Table 5.4, which summarize the percentage error between the mean J-K feature predicted by the EA and the J-K features measured experimentally. Specifically, the former are computed as

$$\bar{A}_J^{\mathcal{P}} = \frac{1}{3} \sum_{s=1}^3 A_J^{\mathcal{P},s} \quad \bar{A}_K^{\mathcal{P}} = \frac{1}{3} \sum_{s=1}^3 A_K^{\mathcal{P},s} \quad (5.12)$$

$$\bar{T}_J^{\mathcal{P}} = \frac{1}{3} \sum_{s=1}^3 T_J^{\mathcal{P},s} \quad \bar{T}_K^{\mathcal{P}} = \frac{1}{3} \sum_{s=1}^3 T_K^{\mathcal{P},s}. \quad (5.13)$$

where $\bar{A}_J^{\mathcal{P}}$ and $\bar{A}_K^{\mathcal{P}}$ represent the mean amplitude of the J-peak and K-valley of the three best ranked curve, whereas $\bar{T}_J^{\mathcal{P}}$ and $\bar{T}_K^{\mathcal{P}}$ are the mean timing of the J-peak and K-valley of the three best ranked curve, respectively. Overall, we can notice that the mean percentage errors in the timing is very low, with an average error less than 2% for both timing of the

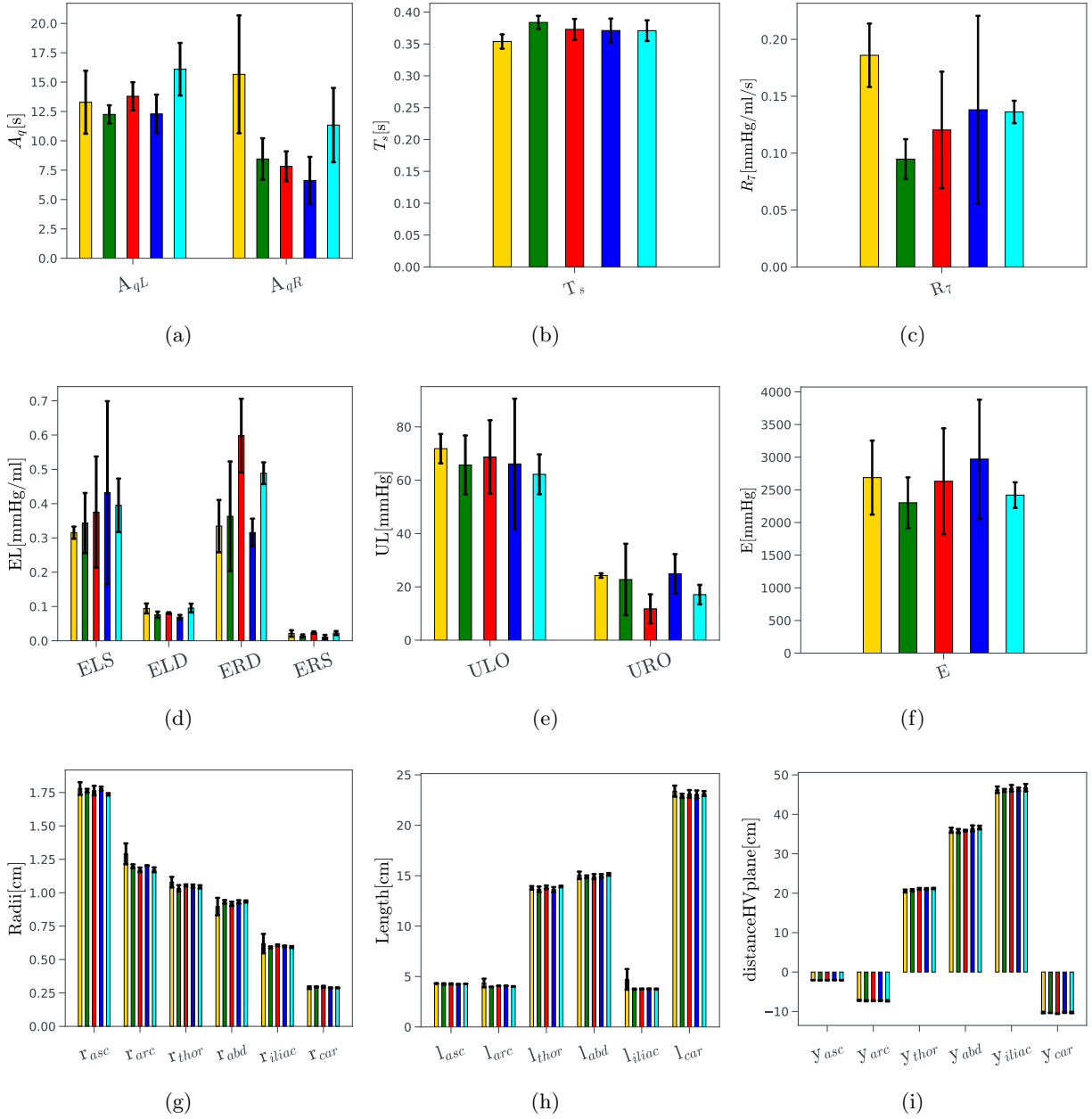


Figure 5.2: Resulting value of the parameter \mathcal{P}^r predicted by the EA.

J peak and K valley. The EA model produces the largest average error when predicting the amplitude of the J-peak, with an average error of 17.3%, whereas a smaller error, quantified in 12.9%, is observed for the J peak. To further verify the capability of the EA algorithm to reach a physiological solution, Fig. 5.4 compares the experimentally measured brachial pressure (black horizontal line) and the closed loop model prediction. Specifically, Fig. 5.4a reports the model pressure waveforms in the ascending aorta predicted by the closed-loop model utilizing the combination of individualized model parameters of the three best ranked

CURVE	$\Delta(\bar{A}_J^P, A_J^M)$	$\Delta(\bar{A}_K^P, A_K^M)$	$\Delta(\bar{T}_J^P, T_J^M)$	$\Delta(\bar{T}_K^P, T_K^M)$
ID	[%]	[%]	[%]	[%]
$n = 1$	20.1 %	18.2 %	1.85 %	2.74 %
$n = 2$	14.3 %	14.0 %	1.59 %	1 %
$n = 3$	2.9 %	16.9 %	1.52 %	0.8 %
$n = 4$	20.1 %	19.2 %	2.43 %	0.89 %
$n = 5$	6.9 %	17.3 %	0.93 %	1.89 %
Mean Value	12.9 %	17.3 %	1.66 %	1.46 %

Table 5.4: Quantitative comparison between the mean J-K feature predicted by the EA and the J-K features measured experimentally. \bar{A}_J^P and \bar{A}_K^P represent the mean amplitude of the J-peak and K-valley of the three best ranked curve predicted for each run by the EA, whereas \bar{T}_J^P and \bar{T}_K^P are the mean timing of the J-peak and K-valley of the three best ranked curve, respectively, predicted for each run by the EA. Conversely, \bar{A}_J^M and \bar{A}_K^M represent the amplitude of the J-peak and K-valley, whereas \bar{T}_J^M and \bar{T}_K^M

curve for $f_{a,1}^M$. Then, the central aortic pressure waveform is amplified by a corrective factor selected according to the age and gender from the work of ..., which have been reported as a vertical line from the peak systolic pressure of the. Fig. 5.4a summarize compares the mean systolic and diastolic brachial pressure predicted for the following n_c curves with the measured pressure. Overall, we can notice a good agreement in the term of predicted pulse pressure amplitude, thereby proving that the model input parameters predicted by the EA provide a reasonable physiological result.

5.4 Conclusion

In this chapter we developed an automated EA algorithm capable of individualizing the input parameter of the closed-loop model. In addition, utilizing the predicted parameter as an input for the cardiovascular model, we were able to obtain a reasonable approximation of the central aortic pressure of the subject, thereby indicating that a physiological solution was reached.

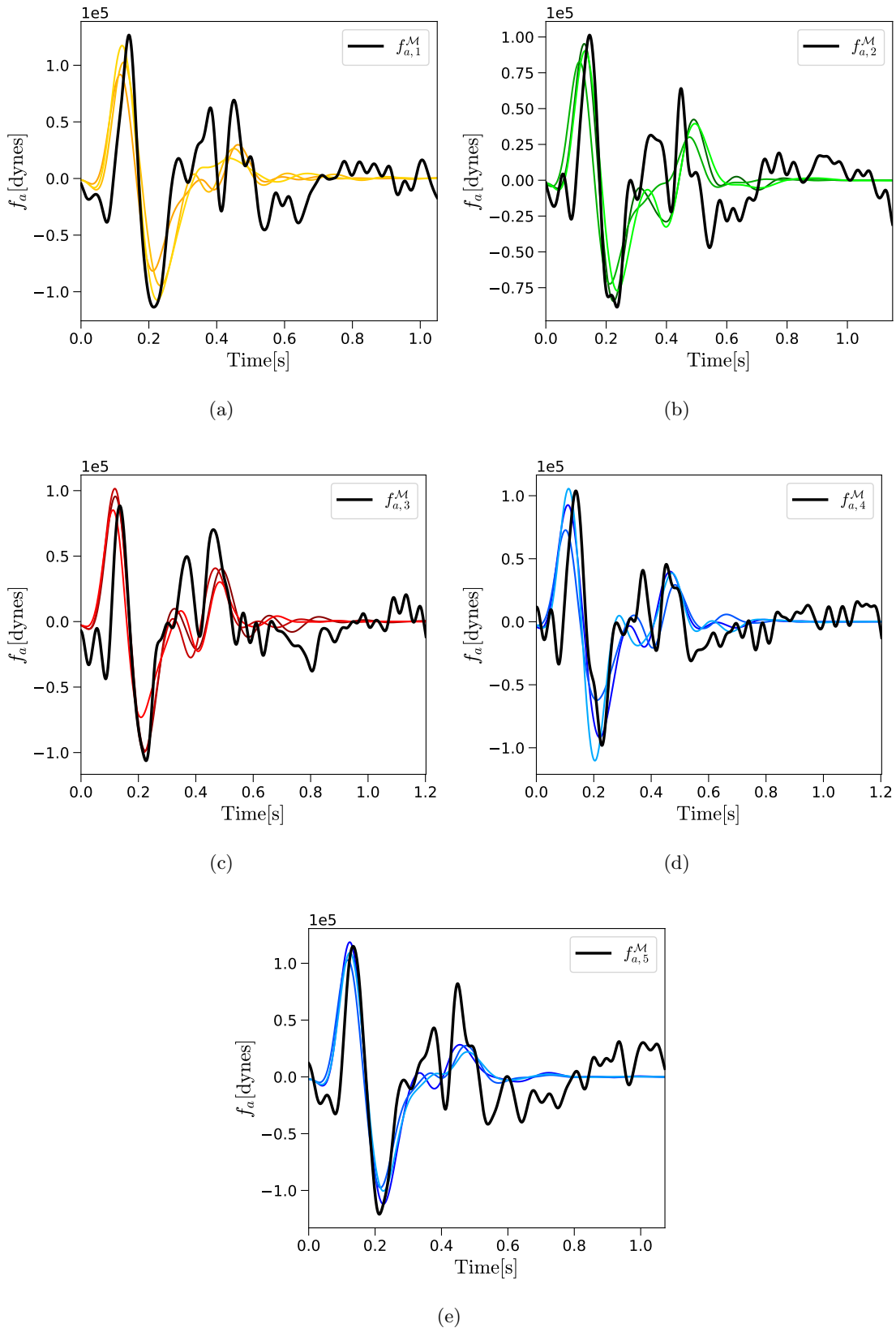


Figure 5.3: Comparison among the experimentally measured a_y curve and the three best-ranked a_y curve computed by the EA (colored-curve).

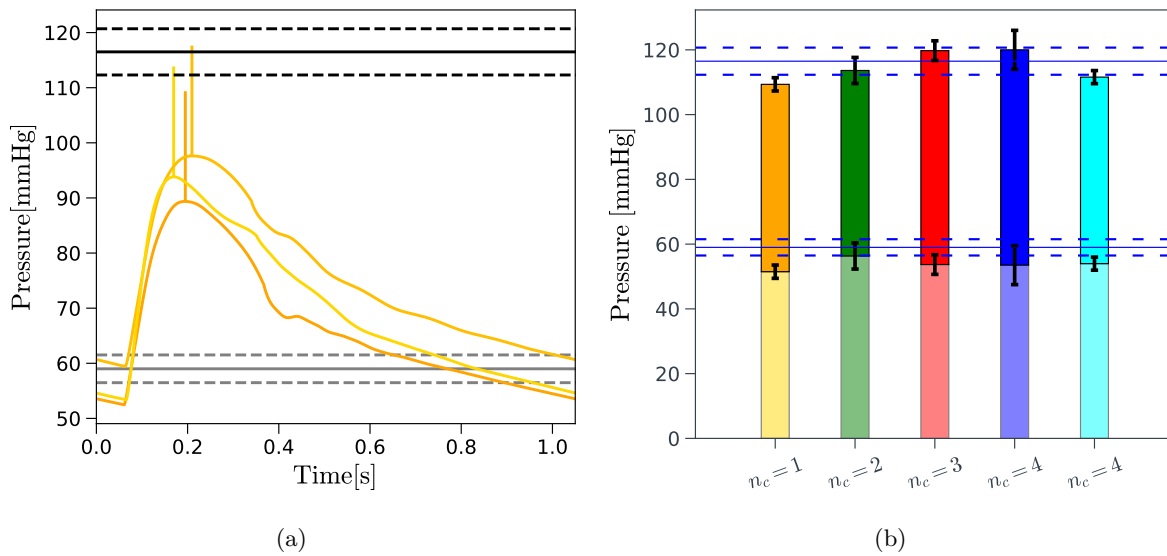


Figure 5.4: Left: Predicted central aortic pressure via the personalized input parameter obtained after the first run of the EA. Right: Comparison between the experimentally measured brachial pulse pressure (blue lines) and the the pressure predicted by the EA.

Chapter 6

Conclusion and Future Directions

In this thesis we presented a physically-based modeling framework for the analysis of the BCG signal, aimed at integrating the physiology with the technological solution utilized to record the BCG signal. In particular:

- in Chapter 2 we provided a mathematical formulation to the concept of **pBCG** and **mBCG**, emphasizing that the former is a physiological signal that is specific to each individual, whereas the latter is a device-dependent signal which varies according to the device which is used. Then, we illustrated how the **mBCG** and **pBCG** concepts can be coupled utilizing the physics of two sensing devices, namely the suspended bed and the load cell system;
- In Chapter 3 we compared the reconstructed **CoM** motion, in physical units, from accelerometer on the suspended bed and the load cell signals.
- in Chapter 4 we proposed a novel non-invasive methodology to estimate the absolute brachial pulse pressure integrating *(i)* synchronous recordings of the ECG and BCG and *(ii)* theoretical simulations of the cardiovascular system.
- in Chapter 5 we developed an evolutionary algorithm to individualize the parameters of the cardiovascular model utilizing the BCG signal obtained from the suspended bed;

Overall, the most critical outcome of the present thesis is that physical based modeling can enhance the comprehension of the BCG signal, as shown by the following results:

- the **CoM** motion reconstructed by two different sensing devices results in the same order of magnitude and in a similar shape for three subjects. In particular, a remarkable agreement in terms of shape and magnitude is obtained in the shoulder to shoulder direction. The main significance of the present results is towards the individualization and standardization of the BCG signal, which could facilitate the identification

of instances when changes in the BCG waveform are truly indicative of pathological conditions rather than changes in the device setting.

- the proposed cuff-less methodology was tested on 10 subjects and predicts the individual pulse pressure with an overall good approximation, namely with a 8% average error in the male subjects and with a larger 18 % of in the female subjects. Thus, our method offers a promising methodology for non-invasive measurement of absolute pulse pressure, which is a known markers for cardiovascular monitoring;
- We provided evidences of male/female difference in the BCG signal, in particular in terms of the magnitude of the most prominent peaks and valley in the CoM motion in the head-to-toe direction. This result indicate that the BCG signal could be a promising methodology to evaluate sex-differences in cardiovascular functions;
- the EA algorithm predicts, for one subject, a set of individual parameters P^r that results in a a_y waveform in a good agreement with the a_y measured in the lab. In addition, the brachial pressure predicted utilizing the personalized individual parameters P^r demonstrate a significant agreement with the pressure measured in the lab. Thus, our methodology offers a promising venue to (i) personalize the closed-loop model and (ii) access several personalized information about the subject that are of clinical interest but cannot be measured directly.

Finally, the following direction of research could be investigated to overcome the limitations associated with this work:

- to investigate the reason of the observed delay and amplification in the CoM motion reconstructed from the load cell system in the head-to-toe direction;
- to seek a functional relationship between the mBCG recorded utilizing the hydraulic bed sensor and the pBCG;
- to verify the sensitivity of the parameters of the proposed cuff-less methodology, in particular referring to the variability of the compliance among male and female subjects;
- to define a larger database comprising male and female subjects to test the statistical significance of the differences in the pBCG features between male and female subjects;
- to test the EA methodology on a larger population;
- to verify the sensitivity of the proposed EA formulation upon the curve initialization;

Bibliography

- [1] Alaleh Alivar, Charles Carlson, Ahmad Suliman, Steve Warren, Punit Prakash, Dave Thompson, and Balasubramaniam Natarajan. Motion detection in bed-based ballistocardiogram to quantify sleep quality. In *GLOBECOM 2017-2017 IEEE Global Communications Conference*, pages 1–6. IEEE, 2017.
- [2] Alaleh Alivar, Charles Carlson, Ahmad Suliman, Steve Warren, Punit Prakash, David E Thompson, and Balasubramaniam Natarajan. Motion artifact detection and reduction in bed-based ballistocardiogram. *IEEE Access*, 7:13693–13703, 2019.
- [3] Wirt Atmar. Notes on the simulation of evolution. *IEEE Transactions on Neural Networks*, 5(1):130–147, 1994.
- [4] Guido Avanzolini et al. Cadcs simulation of the closed-loop cardiovascular system. *International Journal of Biomedical Computing*, 22(1):39–49, 1988.
- [5] Athanase Benetos, Frédérique Thomas, Laure Joly, Jacques Blacher, Bruno Pannier, Carlos Labat, Paolo Salvi, Harold Smulyan, and Michel E Safar. Pulse pressure amplification: a mechanical biomarker of cardiovascular risk. *Journal of the American College of Cardiology*, 55(10):1032–1037, 2010.
- [6] Ronald A Bergman. Illustrated encyclopedia of human anatomic variation. <http://www.anatomyatlases.org/AnatomicVariants/MuscularSystem/Text/P/08Pectoralis.shtml>, 2007.
- [7] M Boufi, C Guivier-Curien, AD Loundou, Valerie Deplano, O Boiron, K Chaumoitre, V Gariboldi, and YS Alimi. Morphological analysis of healthy aortic arch. *European Journal of Vascular and Endovascular Surgery*, 53(5):663–670, 2017.
- [8] HC Burger, A Noordergraaf, and AMW Verhagen. Physical basis of the low-frequency ballistocardiograph. *American heart journal*, 46(1):71–83, 1953.
- [9] Sunčica Čanić, Josip Tambača, Giovanna Guidoboni, Andro Mikelić, Craig J Hartley, and Doreen Rosenstrauch. Modeling viscoelastic behavior of arterial walls and their

- interaction with pulsatile blood flow. *SIAM Journal on Applied Mathematics*, 67(1):164–193, 2006.
- [10] Farooq A Choudhry, John T Grantham, Ansaar T Rai, and Jeffery P Hogg. Vascular geometry of the extracranial carotid arteries: an analysis of length, diameter, and tortuosity. *Journal of neurointerventional surgery*, 8(5):536–540, 2016.
- [11] Richard Drake, A Wayne Vogl, and Adam WM Mitchell. *Gray’s Anatomy for Students E-Book*. Elsevier Health Sciences, 2009.
- [12] Laurent Giovangrandi, Omer T Inan, Richard M Wiard, Mozziyar Etemadi, and Gregory TA Kovacs. Ballistocardiography—a method worth revisiting. In *2011 annual international conference of the IEEE engineering in medicine and biology society*, pages 4279–4282. IEEE, 2011.
- [13] Lee Goldman and Andrew I Schafer. *Goldman’s Cecil medicine E-book*. Elsevier Health Sciences, 2011.
- [14] JW Gordon. Certain molar movements of the human body produced by the circulation of the blood. *Journal of anatomy and physiology*, 11(Pt 3):533, 1877.
- [15] Giovanna Guidoboni, Lorenzo Sala, Moein Enayati, Riccardo Sacco, Marcela Szopos, James M Keller, Mihail Popescu, Laurel Despina, Virginia H Huxley, and Marjorie Skubic. Cardiovascular function and ballistocardiogram: a relationship interpreted via mathematical modeling. *IEEE Transactions on Biomedical Engineering*, 66(10):2906–2917, 2019.
- [16] WF Hamilton, Philip Dow, and John W Remington. The relationship between the cardiac ejection curve and the ballistocardiographic forces. *American Journal of Physiology-Legacy Content*, 144(4):557–570, 1945.
- [17] Omer T Inan, Mozziyar Etemadi, Laurent B Giovangrandi, Gregory T Kovacs, and Richard M Wiard. Weighing scale and sensor systems and methods for monitoring heart function, June 16 2015. US Patent 9,055,871.
- [18] Jin Hyun Joh, Hyung-Joon Ahn, and Ho-Chul Park. Reference diameters of the abdominal aorta and iliac arteries in the Korean population. *Yonsei medical journal*, 54(1):48–54, 2013.
- [19] Sakari Junnila, Alireza Akhbardeh, Alpo Varri, and Teemu Koivistoinen. An emfi-film sensor based ballistocardiographic chair: Performance and cycle extraction method. In *IEEE Workshop on Signal Processing Systems Design and Implementation, 2005.*, pages 373–377. IEEE, 2005.

- [20] James M Keller, Derong Liu, and David B Fogel. *Fundamentals of computational intelligence: neural networks, fuzzy systems, and evolutionary computation*. John Wiley & Sons, 2016.
- [21] Inc Kionix. Kxr94-2283. 2014.
- [22] Inc Kionix. Adinstruments powerlab 16/35.
- [23] Antonius Adrianus Knoop. *Experimental Investigations on Ultra-low Frequency Displacement Ballistocardiography*. Number 269. National Aeronautics and Space Administration, 1965.
- [24] Jaroslaw Krejza, Michal Arkuszewski, Scott E Kasner, John Weigele, Andrzej Ustymowicz, Robert W Hurst, Brett L Cucchiara, and Steven R Messe. Carotid artery diameter in men and women and the relation to body and neck size. *Stroke*, 37(4):1103–1105, 2006.
- [25] William D Lakin, Scott A Stevens, Bruce I Tranmer, and Paul L Penar. A whole-body mathematical model for intracranial pressure dynamics. *Journal of mathematical biology*, 46(4):347–383, 2003.
- [26] Mei-Ling T Lee, Bernard A Rosner, and Scott T Weiss. Relationship of blood pressure to cardiovascular death: the effects of pulse pressure in the elderly. *Annals of epidemiology*, 9(2):101–107, 1999.
- [27] Edwards Lifesciences. Normal hemodynamic parameters and laboratory values. *Retrieved on April, 9, 2014*.
- [28] Stephen S Lim, Theo Vos, Abraham D Flaxman, Goodarz Danaei, Kenji Shibuya, Heather Adair-Rohani, Mohammad A AlMazroa, Markus Amann, H Ross Anderson, Kathryn G Andrews, et al. A comparative risk assessment of burden of disease and injury attributable to 67 risk factors and risk factor clusters in 21 regions, 1990–2010: a systematic analysis for the global burden of disease study 2010. *The lancet*, 380(9859):2224–2260, 2012.
- [29] Alicia M Maceira et al. Reference right ventricular systolic and diastolic function normalized to age, gender and body surface area from steady-state free precession cardiovascular magnetic resonance. *European Heart Journal*, 27(23):2879–2888, 2006.
- [30] Alicia M Maceira et al. Normalized left ventricular systolic and diastolic function by steady state free precession cardiovascular magnetic resonance. *Journal of Cardiovascular Magnetic Resonance*, 8(3):417–426, 2006.
- [31] Harold W March. Three-plane ballistocardiography: the effect of age on the longitudinal, lateral, and dorsoventral ballistocardiograms. *Circulation*, 12(5):869–882, 1955.

- [32] Om Narayan, Joshua Casan, Martin Szarski, Anthony M Dart, Ian T Meredith, and James D Cameron. Estimation of central aortic blood pressure: a systematic meta-analysis of available techniques. *Journal of hypertension*, 32(9):1727–1740, 2014.
- [33] JT Ottesen and M Danielson. Modeling ventricular contraction with heart rate changes. *Journal of theoretical biology*, 222(3):337–346, 2003.
- [34] H Mitchell Perry Jr, WM Smith, Robert H McDonald, Dennis Black, Jeffrey A Cutler, Curt D Furberg, Merwyn R Greenlick, Lewis H Kuller, HW Schnaper, and JA Schoenberger. Morbidity and mortality in the systolic hypertension in the elderly program (shep) pilot study. *Stroke*, 20(1):4–13, 1989.
- [35] SIMON W RABKIN, FRANCIS AL MATHEWSON, and ROBERT B TATE. Longitudinal blood pressure measurements during a 26-year observation period and the risk of ischemic heart disease. *American Journal of Epidemiology*, 109(6):650–662, 1979.
- [36] Shoba Ranganathan, Kenta Nakai, and Christian Schonbach. *Encyclopedia of Bioinformatics and Computational Biology: ABC of Bioinformatics*. Elsevier, 2018.
- [37] Alban Redheuil, Wen-Chung Yu, Elie Mousseaux, Ahmed A Harouni, Nadjia Kachenoura, Colin O Wu, David Bluemke, and Joao AC Lima. Age-related changes in aortic arch geometry: relationship with proximal aortic function and left ventricular mass and remodeling. *Journal of the American College of Cardiology*, 58(12):1262–1270, 2011.
- [38] Licet Rosales, Bo Yu Su, Marjorie Skubic, and KC Ho. Heart rate monitoring using hydraulic bed sensor ballistocardiogram 1. *Journal of Ambient Intelligence and Smart Environments*, 9(2):193–207, 2017.
- [39] Riccardo Sacco, Giovanna Guidoboni, and Aurelio Giancarlo Mauri. *A Comprehensive Physically Based Approach to Modeling in Bioengineering and Life Sciences*. Academic Press, 2019.
- [40] William R Scarborough, SAMUEL A TALBOT, JOHN R BRAUNSTEIN, MAURICE B RAPPAPORT, WILLIAM DOCK, WILLIAM R SCARBOROUGH, WF Hamilton, JOHN E SMITH, JOHN L NICKERSON, SAMUEL A TALBOT, et al. Proposals for ballistocardiographic nomenclature and conventions: Revised and extended: Report of committee on ballistocardiographic terminology. *Circulation*, 14(3):435–450, 1956.
- [41] Hangsik Shin and Se Dong Min. Feasibility study for the non-invasive blood pressure estimation based on ppg morphology: normotensive subject study. *Biomedical engineering online*, 16(1):10, 2017.

- [42] Jae Hyuk Shin and Kwang Suk Park. Hrv analysis and blood pressure monitoring on weighing scale using bcg. In *2012 Annual International Conference of the IEEE Engineering in Medicine and Biology Society*, pages 3789–3792. IEEE, 2012.
- [43] Spotswood L Spruance, Julia E Reid, Michael Grace, and Matthew Samore. Hazard ratio in clinical trials. *Antimicrobial agents and chemotherapy*, 48(8):2787–2792, 2004.
- [44] Isaac Starr and Abraham Noordergraaf. *Ballistocardiography in cardiovascular research: Physical aspects of the circulation in health and disease*. Lippincott, 1967.
- [45] Isaac Starr and AJ Rawson. The vertical ballistocardiograph; experiments on the changes in the circulation on arising; with a further study of ballistic theory. *American Journal of Physiology-Legacy Content*, 134(2):403–425, 1941.
- [46] Bo Yu Su, Moein Enayati, KC Ho, Marjorie Skubic, Laurel Despina, James Keller, Mihail Popescu, Giovanna Guidoboni, and Marilyn Rantz. Monitoring the relative blood pressure using a hydraulic bed sensor system. *IEEE Transactions on Biomedical Engineering*, 66(3):740–748, 2018.
- [47] Ahmad Suliman, Charles Carlson, Carl J Ade, Steve Warren, and David E Thompson. Performance comparison for ballistocardiogram peak detection methods. *IEEE Access*, 7:53945–53955, 2019.
- [48] Robert B Tate, Jure Manfreda, Andrew D Krahn, and T Edward Cuddy. Tracking of blood pressure over a 40-year period in the university of manitoba follow-up study, 1948–1988. *American Journal of Epidemiology*, 142(9):946–954, 1995.
- [49] Charalambos Vlachopoulos, Michael O’Rourke, and Wilmer W Nichols. *McDonald’s blood flow in arteries: theoretical, experimental and clinical principles*. CRC press, 2011.
- [50] Arik Wolak, Heidi Gransar, Louise EJ Thomson, John D Friedman, Rory Hachamovitch, Ariel Gutstein, Leslee J Shaw, Donna Polk, Nathan D Wong, Rola Saouaf, et al. Aortic size assessment by noncontrast cardiac computed tomography: normal limits by age, gender, and body surface area. *JACC: Cardiovascular Imaging*, 1(2):200–209, 2008.
- [51] Nikos A Zakopoulos, John P Lekakis, Christos M Papamichael, Savas T Toumanidis, John E Kanakakis, Dimitris Kostandonis, Theodosia J Vogiazoglou, Christos G Rombopoulos, Stamatios F Stamatelopoulos, and Spyridon D Mouloupoulos. Pulse pressure in normotensives: a marker of cardiovascular disease. *American journal of hypertension*, 14(3):195–199, 2001.
- [52] Dennis G Zill and Michael R Cullen. *Differential equations*. Brooks/Cole, Cengage Learning., 2009.